Fall 12-2022

IMAGING METAL OBJECTS THROUGH RADIO FREQUENCY CHANNEL SOUNDING

Jamison Ehlers

IMAGING METAL OBJECTS THROUGH RADIO FREQUENCY CHANNEL SOUNDING

by

Jamison Ehlers

A thesis submitted in partial fulfillment of the
requirements for the degree of

Masters of Science in Electrical Engineering

Montana Tech
2022

Abstract

Metal casting is used widely throughout the manufacturing industry, where detection of imperfections is an important aspect of the overall casting process. This work proposes a system based on wireless signal propagation at radio frequency could be used to develop a model for defect detection of a metal part. A proof of concept was constructed of the proposed system to detect the presence of metal inside the propagation channel. The dielectric properties of the sand-casting media were observed, as well as losses and time-delays due to the introduction of a metal object. The measurement setup was validated using set lengths of cables as the propagation channel rather than wireless transmission.

Keywords: RF propagation, dielectric properties, loss tangent, RF imaging

Dedication

This work is dedicated to my family, Jim, Kathy and Kellen Ehlers. Without your support, I could not have gotten to this point.

Acknowledgements

This research was sponsored by the Combat Capabilities Development Command Army Research Laboratory and was accomplished under Cooperative Agreement number W911NF-20-0163. The views and conclusions contained in this document are those of the authors and should not be interpreted as representing the official policies, either expressed or implied, of the Combat Capabilities Development Command Army Research Laboratory or the U.S. Government. The U.S. Government is authorized to reproduce and distribute reprints for Government purposes notwithstanding any copyright notation herein.

I would like to thank my advisor, Dr. Bryce Hill for getting me on this project, as well as the various opportunities as an undergrad working on research. Without him, I would not be where I am today. I would also like to thank Dr. Kevin Negus for his insight throughout the project, as well as convincing me to continue my academic studies, along with Dr. Hill, after my bachelors. I would also like to thank Dr. Richard LaDouceur for agreeing to on my committee, and providing much appreciated observations and critiques when defending this work.

Thanks goes to Benjamin Rathman for assistance in machining the custom waveguides, Kathryn Bozer and Reed Harder for helping me process the sandcasts, and Tyler Holliday for his assistance measuring the trigger on the signal generator.

Finally, I'd like to thank the Montana Tech Electrical Engineering Department. Everyone here was critical throughout my academic career either from supporting the various projects I've been a part of, or providing me the knowledge to further my career as an engineer.

Table of Contents

List of Tables

List of Figures

List of Equations

Glossary of Terms

Term	Definition
RF	Radio Frequency, refers to electromagnetic signals with an approximate frequency between 20 kHz and 300 GHz
VNA	Vector Network Analyzer, equipment used to analyze a systems amplitude and phase properties
RTI	Radio Tomographic Imaging
IEEE	Institute of Electrical and Electronic Engineers
802.11	IEEE standard outlining wireless networks
LAN	Local Access Network
WLAN	Wireless Local Access Network
FCC	Federal Communications Commission
MRI	Magnetic Resonance Imaging
MPI	Magnetic Particle Inspection
Radar	Radio detection and ranging
SNR	Signal-to-Noise Ratio
TEM	Transverse Electromagnetic
SA	Spectrum Analyzer
VSG	Vector Signal Generator
ISM	Industrial, Scientific and Medical

1. Introduction

1.1. Background

Since ancient times, casting has been used to create and produce metal products on a large scale. The first known castings occurred during the Copper Age, around 5000 B.C., in the Balkans [1] During the casting process, many defects can occur, such as porosity, inclusions, and metal penetration [2]. These imperfections introduced during the casting process can create lasting effects on the quality of the product and can be expensive to identify, and usually cannot be identified until after the casted part has been completed.

Many challenges arise with identifying such defects, such as their location in the cast. If the part in question is large, defects may form deep inside the part, and could be harder to find. Some defects can only be found during the machining process, when finding such defects can be already too late, while others are only discovered once the part has failed. Within the last century, advancement in technology has allowed for advanced imaging techniques to arise, leading to more accurate diagnostics when it comes to different applications, such as medical imaging or quality control with casting products.

There are already imaging methods available, such as x-ray and ultrasonic. However, most equipment that utilize these methods require trained professionals, or are quite expensive [3] [4]. Many alternatives for cast imaging are destructive, causing the part under test to be unusable after locating the defects in question, requiring more to be made. All these methods are only able to be performed after the part has been formed and cooled, requiring a sample to be taken off the production line and tested.

1.2. Problem Statement

This work proposes the framework for an alternate imaging method using radio frequency (RF) electromagnetic waves to create a model of the part as the cast fills, to be later used to generate an image.

The overall goal of this work was to provide a proof of concept for and determine the feasibility of the imaging system for use on non-ferric materials. To complete this work in a reasonable amount of time, the proof of concept was done for only one dimension of a metal plate, or the thickness. As a result, this methodology can be used to develop future models and systems for the remaining two dimensions.

1.3. Imaging Overview

Imaging is defined by the Oxford Dictionary as the process of making a visual representation of something by scanning it with a detector or electromagnetic beam and is usually associated with medical imaging. Most imaging methods are used to investigate something invisible to the naked eye. In the next few sections, similar imaging techniques and applications to this work are discussed, as well as other testing methods in the casting industry, focusing on those using electromagnetic propagation.

1.3.1. Magnetic Resonance Imaging

Magnetic resonance imaging (MRI) operates by magnetizing hydrogen atoms in the subject by way of a powerful electromagnet. Once the subject is inside of the machine and a magnetic field is established, RF pulses are introduced to disturb hydrogen atoms inside of the patient [5]. This is done at the same frequency as the magnetic field, to allow for resonance and energy transfer between the RF pulse and the magnetic field. The RF pulses can be anywhere from 1 MHz to 300 MHz, depending on the strength of the magnetic field, but a typical

frequency is 64 MHz [6] [7]. These pulses cause the hydrogen atoms' protons to move out of phase with the magnetic field. From there, the hydrogen protons will realign, and based on the realignment of the protons' phase with respect to time, the phases of the disturbed atoms can be recorded using a receiver coil and RF receiver. Depending on the tissues being observed, and the type of pulse used, different images can be generated, highlighting different tissues. The main risk associated with MRI scans include the presence of metal. Any metal can distort the image, as well as present a safety concern if the metal is magnetic [8]. An example of an MRI machine and MRI scan can be seen in Figure 1 and Figure 2 respectively.

Figure 1: A medical MRI machine, used to generate diagnostic images of patients [6]

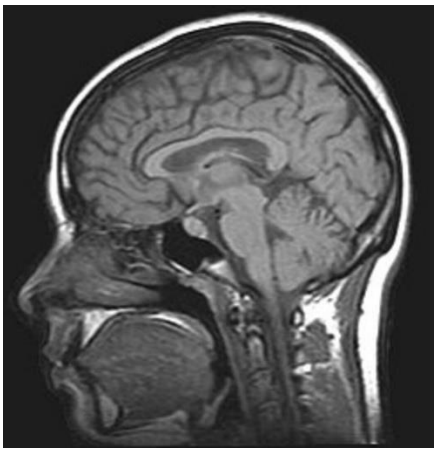

Figure 2: Brain scan image, generated via MRI [9]

1.3.2. Magnetic Particle Testing

A similar method to MRI in the casting industry, magnetic particle inspection (MPI), is used on casts to locate surface and near-surface discontinuities in ferromagnetic materials after cooling [10]. This is done through application of one or more magnetic fields on colored magnetic particles applied to the part. When the fields encounter a discontinuity transverse to the direction of the field, the magnetic flux lines produce a leakage field, attracting the magnetic particles into the discontinuity, creating a visible indication. The operational frequency of MPI

varies widely, from full and half-wave DC to 100 kHz AC. Direct-current (DC) is typically used to detect sub-surface defects, while alternating-current (AC) is used for surface defects, due to a physical phenomenon known as the skin effect, where current flow in AC runs along the surface of the part [11]. The frequency of the AC determines the amount of penetration into said part. This method is limited to ferromagnetic materials, such as iron, cobalt, nickel, and other alloys of these materials and can only detect either surface or near-surface defects.

1.3.3. Ultrasound

Ultrasound imaging has existed since the late 1940's and uses high-frequency sound waves to create an image [12] [13]. These sound waves are far above the human threshold for hearing and can be in the megahertz range. These sound waves are applied by a transducer probe directly on the skin and images are generated in real time. This probe utilizes piezoelectric materials to both generate and receive sound waves through an electric field. Soundwaves are then sent into the patient, reflected after creating contact with a tissue boundary of differing tissue types and sends an electrical signal back to the device. Utilizing the speed of sound, and time of signal return, the distance from the probe to the tissue boundary is calculated and an image is produced. An example of a medical ultrasound transducer and image can be seen in Figure 3 and Figure 4.

Figure 3: A computer rendering of a medical ultrasound transducer [13]

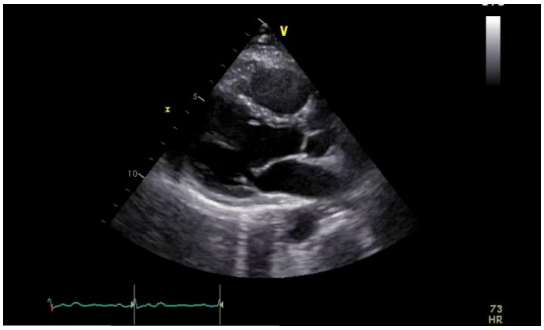

Figure 4: An echocardiogram of a heart, generated through ultrasound [14]

Ultrasound is already used in the casting industry to inspect finished products. It allows for high accuracy, and detection of extremely small flaws. This method is ultimately limited to thicker casts, as well as penetration into the part. The higher the frequency generated, the more precise the measurement, but lower penetration. While lower frequencies allow for deeper penetration but result in lower sensitivity [10].

1.3.4. Radiographic

A common imaging method in both the medical and casting fields, radiographic testing commonly uses x-rays (3×10^{17} Hz) to penetrate the material of the cast in question. For more dense casts, gamma rays (3×10^{23} Hz) are used [15]. To apply these waves, decaying radioactive materials, such as Iridium-192 and Cobalt-60 are used. The waves penetrate the part in question, recorded on a special film on the other side of the part in relation to the wave. When developing the film, darker images indicate sections where more radiation passed through the part, while lighter images indicate less penetration [10]. Limitations in radio graphic methods are the rarity of the radiation producing materials, as well as having the facilities to perform such a test, as the radiation itself can be highly dangerous to living beings over long periods of exposure.

1.3.5. Radar

Radar is a well-known imaging method, typically used for surveillance and tracking [16]. There are many different types of radars, varying with their method of radiation and control setup. This

Firstly, a radar system transmits an electromagnetic pulse [16]. The parameters of this pulse can vary, depending on the purpose of the radar operation. Modern radar will use complex wave forms with specific auto correlation properties, to improve accuracy [17]. The signal is

then modulated and up converted to transmission frequency and amplitude. This carrier modulated signal is then fed into the antenna, propagating this radar pulse, which will then traverse until the pulse is either reflected against an object, or continues until its energy dissipates. Traditional radars will then switch their transmitter with a receiver and wait for a return signal, or it will be received by a different antenna all together. Once the reflected waveform is captured by the receiver antenna, the receiver will then down-convert the signal to a usable frequency. This signal is then passed through a matched filter with the transmitter to remove any noise and is then used to predict where the target is. As for this work's purpose, the main limitation to radar for close range application is the range resolution, derived from Fell [16].

$$\sigma_R \propto \frac{1}{f}\frac{1}{\sqrt{SNR}} \tag{1}$$

In equation (1), σ_R is the standard deviation of the range measurements taken, f is the frequency or effective bandwidth of the system and SNR is the signal-noise ratio of the system. In any radar application, σ_R would be, ideally, small and constant, while frequency and SNR would remain large.

1.4. Previous Work

1.4.1. Material Characterization

The methods of electrically characterizing materials are wide and varied, as seen with Jesch [18], Cote [19] and Matzler [20]. Many studies on the dielectric constant of sand focused on expressing the constant as a function of water content at set frequencies [18] [21]. The dielectric constant for dry sand found by Jesch [18] and Matzler [20] being between 2.56 and 2.73. The loss tangent for sand found by Jesch was in the range of -0.00372 to 0.240. The

differences in the location of the samples taken in both studies likely contributed to the difference in measured dielectric properties.

In work done by Cote [19], the dielectric constants and loss tangents of different fluid types were explored, using a custom waveguide setup to collect data on the fluid in question. From this study, the characterization setup was adopted and applied to crushed sandcasts. Waveguides, the dielectric constant, and loss-tangent will be further discussed in section 1.5

1.4.2. Imaging Techniques Used in Cast Monitoring

Techniques used to monitor casting processes are wide and varied, from monitoring the state of the cast during the process using sensors and other monitoring devices [22] [23], to statistical models based on a set sample size of the product in question [24]. These systems suffer from the sensors not being able to survive the casting process [22], or the requirement of a sample set to apply the changes through statistic modeling [24]

1.4.3. Radio Tomographic Imaging

Much research has been done in using radio tomographic imaging (RTI) to localize people and objects in indoor environments without the use of additional devices. RTI implements detection of changes in a radio signal's propagation statistics due to obstruction. Said systems are usually compromised of numerous radio links, or antennas [25] or take advantage of special diversity between the transceivers [26]. Traditional systems usually operate in the lower Wi-Fi band of 2.4 GHz, being less sensitive to small movements in the environment, but having increased stability in connection strength and improved range. These systems also take advantage of existing devices to ease implementation.

1.5. Electrical Concepts

1.5.1. Waveguides

To characterize the sandcast, the experimental design and methodology was adopted from work by Cote [19] to measure the electrical characteristics of the sandcast to be used, provided by DevCom. The electrical characterization process is defined using a waveguide to aid in finding dielectric loses caused by the crushed sand cast. The characterization setup involves sending a test signal into a waveguide, of frequencies from 100 kHz to 8.5 GHz, via a vector network analyzer (VNA), and observing the received signal content.

Waveguides are structures used to guide either electromagnetic or mechanical waves in one direction, with minimal loss of energy. Some examples of electromagnetic waveguide applications are microwave ovens, coaxial and fiber optic cable, and antenna feeds for radar systems. Transmission lines are another example and are made of at least two conductors. Coaxial cables have an inner conductor, usually copper, and an outer conductor shield, with a dielectric insulator between them (Figure 5).

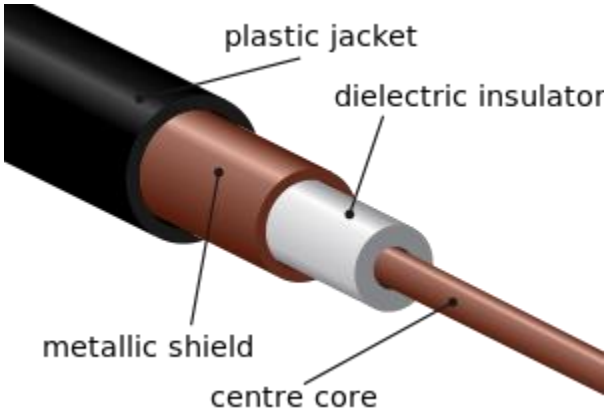

Figure 5: Diagram of a coaxial cable [27]

In two-conductor transmission lines, the dominant mode of electromagnetic wave propagation is transverse electromagnetic (TEM), where there is no electrical field component or magnetic field component in the direction of propagation, as seen in Figure 6. In this example, a

TEM wave traveling down the cable will have an electric field between the inner and outer conductor as well as a magnetic field around the inner conductor, but neither will be pointed transversely down the cable [28].

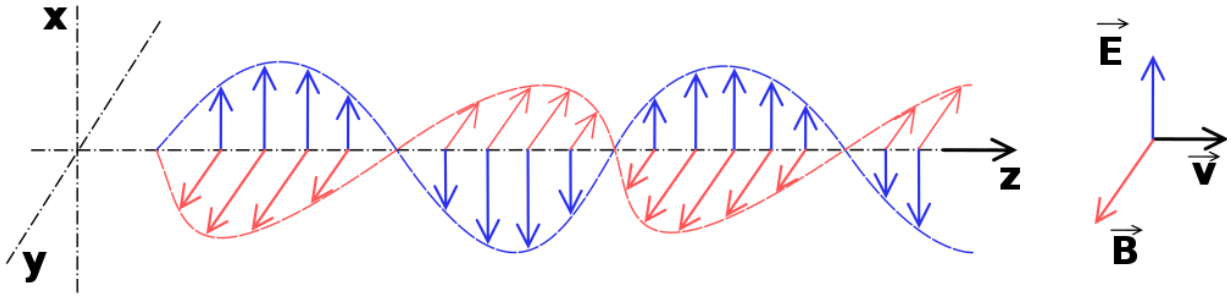

Figure 6: A pictorial representation of TEM Propagation [29]

As for traditional electrical waveguides, TEM wave propagation is not supported, resulting in transverse electric (TE) or transvers magnetic (TM) propagation. Plainly speaking, neither the electric or magnetic fields traverse along the length of the waveguide, rather at an angle. This behavior is due to the boundary conditions of the fields at the surfaces of the waveguide [19]. Due to the lack of TEM propagation, a minimum wavelength for waves propagating in the waveguide becomes apparent, leading to the waveguide to act as a high-pass filter. Using a vector network analyzer, or VNA, the systems response can be collected, and the cutoff frequency observed, via scattering parameters.

1.5.2. Scattering Parameters

Scattering parameters, also known as s-parameters, are a measure of the ratio of voltages sent and received from different ports of a system [28]. System characteristics such as impedance match, return loss, and insertion loss can be described using s-parameters. s-parameters are given in the form S_{mn} where m is the receiving port and n is the sending port.

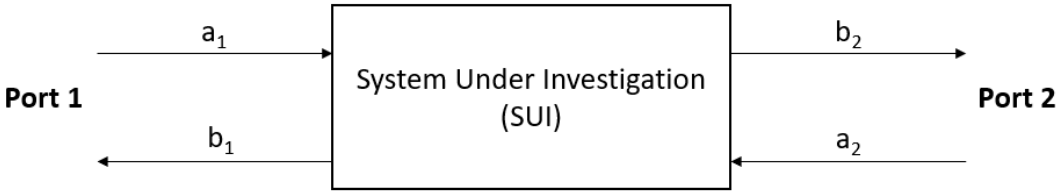

Figure 7: Example of scattering parameter components, adapted from Cote [19]

$$S_{mn} = \frac{b_m}{a_n} = \frac{V_m^-}{V_n^+} \quad (2)$$

V_n^+ is the voltage of the "input" signal at port one while V_m^- is the voltage of the "output" signal at port two. One S-parameter, S_{12}, would be the ratio of voltages received at port one with respect to the voltage sent from port two [28], whereas S_{11} would be the voltage received at port one after sending from the same port.

1.5.3. Fresnel Zone

One important property of wireless transmission is the Fresnel Zone. When electromagnetic waves are transmitted, the dominant signal will travel in a straight path from transmitter to receiver. The signal will diffract, however, and small copies of the signal will propagate through deviated paths from the main path. These "copies" will either be in-phase or out of phase with the transmitted signal. The area these deviated paths cover are called Fresnel zones. Between transmitter and receiver, there are an infinite number of Fresnel zones, numbered one through N. The copies of the signal are then summed at the receiver, either constructively or destructively, depending on the resultant phase of the copies, where the change in phase is proportional to the path-length difference between the two signals [15].

As the number of the Fresnel Zone increases, the effect the resultant signals copy has on the received signal is less significant, with the first Fresnel zone having the biggest effect. Due to

the presence of Fresnel zones, multi-path propagation becomes prevalent. See Figure 8 for an example of Fresnel Zones.

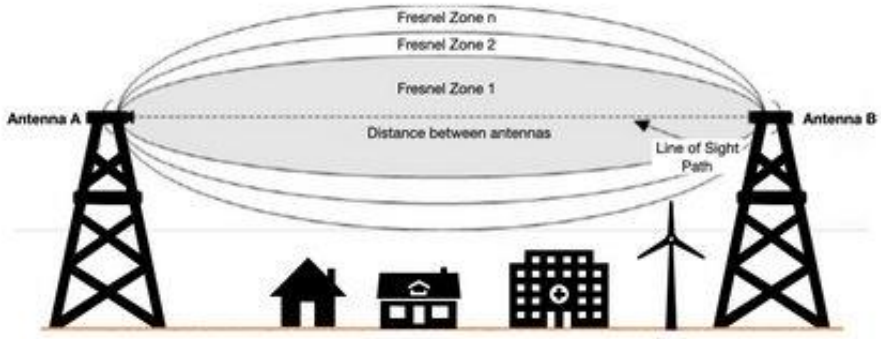

Figure 8: Illustration of Fresnel zones between two antennas [30]

1.5.4. Multi-path Propagation

When a non-periodic signal is transmitted over-air via an antenna, a phenomenon known as multi-path fading, a direct product of Fresnel Zones, occurs. Multi-path is caused by numerous factors, mainly caused by the signal being refracted and reflected by the propagation environment and delayed with respect to time. This affect can be modeled as a filtering operation on the transmitted signal, with the filter characteristics possibly varying with time and frequency [31].

Should the signals copies pass through two channels, i.e., two different paths, with a significant time-delay, destructive interference can occur, causing signal fading. This received signal can be modeled as the output of k transfer functions, with the channel it traveled through being the transfer function. This relationship is outlined by the following equations from Golio [31] where s_0 is the baseband signal, α is the gain of the channel, ϕ is the phase offset, δ is the

impulse response of the channel, $s(t)$ is the transmitted signal and τ is the time-delay of the channel.

$$s(t) = Re[s_0(t)e^{j2\pi f_c t}] \quad (3)$$

$$h(t) = \sum_{k=1}^{M} \alpha_k e^{j\phi_k} \delta(t - \tau_k) \quad (4)$$

$$H(f) = \alpha_k e^{j\phi_k - 2j\pi f \tau_k} \quad (5)$$

$$r_0 = \sum_{k} \alpha_k s_0(t - \tau_k) e^{(j\phi_k - j2\pi f_c \tau_k)} \quad (6)$$

1.5.5. Signal Generation

To ease development and observation of such a system, 5.55 GHz, was selected as the operating frequency, due to many factors. The first factor being the higher density and lower cost of components operating in this frequency. Another factor being that equipment that can operate in this band was readily available, and thus the only equipment needed to be ordered were new antennas. The final factor in selecting this band is the ability to operate. In accordance with standards set by the Federal Communications Commission (FCC), eight frequency bands from 5.150 to 7.125 GHz are unlicensed for specific use, allowing for amateur use in these bands. For this application, the U-NII-2C band was used [32]. This specific band was selected after observation of a lack of other activity, to avoid interference from local wireless networks.

To accurately record a time-delay, a signal with high autocorrelation parameters was needed, to get accurate timing. To generate this, a script in MATLAB was created to produce a pseudo-noise sequence. Pseudo-noise, or PN sequences are used in many applications, such as signal synchronization, radar ranging, multi-path resolution and signal identification [17]. The type of PN sequence used for this work is a binary maximum length sequence, or m sequence. A binary shift-register sequence satisfies a linear recurrence relation of the form

$$\sum_{i=0}^{r} f_i s(t+i) = 0 \quad for\ all\ t \geq 0 \tag{7}$$

where $r \geq 1$ is the degree of the recursion; coefficients f_i belong to the finite field GF (2) = {0,1}, with the leading coefficient $f_r = 1$, as described by Gibson [17]. Said *r*-bit binary shift register can assume a maximum of 2^r states, resulting in the sequence being periodic, with a period of $n \leq 2^r$. An m-sequence is such that the period is maximal. This results in the sequence of length *n* having the autocorrelation property value in equation (9), where the autocorrelation of a binary sequence is defined in equation (8).

$$\theta_s(\tau) = \sum_{t=0}^{n-1} (-1)^{s(t+\tau) - s(t)} \tag{8}$$

$$\theta_s(\tau) = \begin{cases} n & if\ \tau = 0 \\ -1 & if\ \tau \neq 0 \end{cases} \tag{9}$$

where $s(t)$ is the original sequence and $s(t+\tau)$is the time delayed version of the sequence.

The sequence used in this research had a length of 32 bits and was concatenated eight times. The sequence was then modulated using binary-phase shift key (BPSK) and band-limited using a raised-cosine filter with a β of 0.25 and a span of 100.

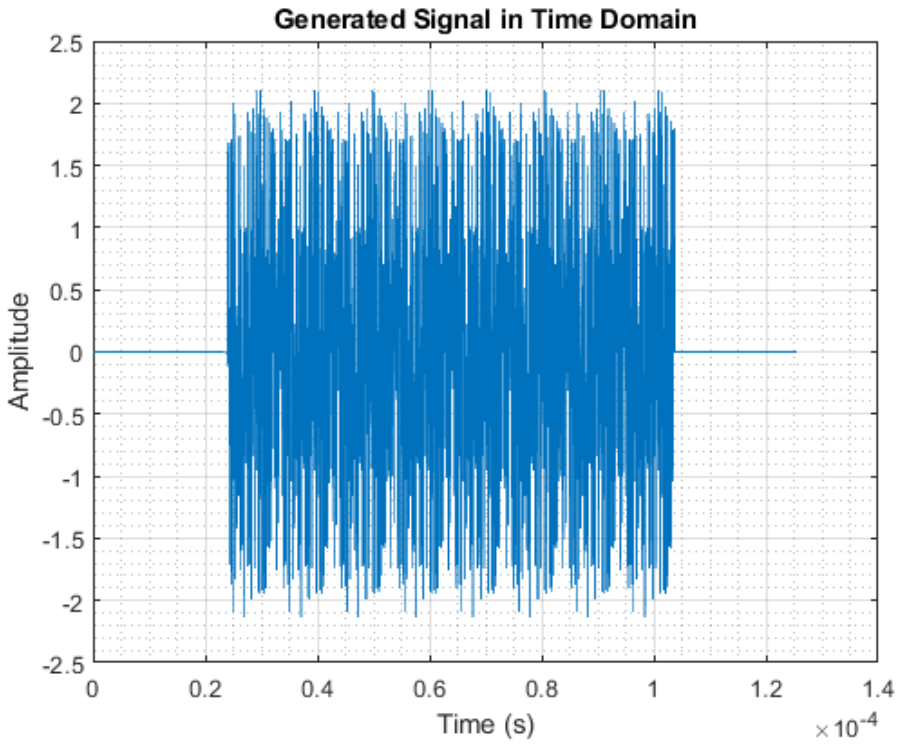

Figure 9: Signal used to calculate the time-delay in the system

1.5.6. Signal Interpolation

Due to the expensive nature of high sampling rate equipment, linear interpolation was used to approximate a smaller time resolution between received consecutive samples during post-processing. The received signal had samples of value zero placed between the original samples. This new signal is then sent through a lowpass filter to achieve an approximation of new samples.

This interpolation method provided a better approximation of the continuous-time signal. However, increasing the time resolution has limitations. As the added number of samples are increased, the perfect continuous time signal is better approximated. Having said that, the internal digital-to-analog and analog-to-digital converters (DAC and ADC respectively) have their own sampling resolution. Since said converters were used to transmit and receive the signal respectively, the closer the approximation to the perfect signal, the greater the deviation from

what was transmitted, due to the limitations of the ADCs and DACs. Despite this, a span of interpolation factors was used to see changes in stability between each factor. The factors used were two, four, eight and sixteen. These resulted in post-processing sample rates of 500 MS/s, 1GS/s, 2GS/s and 4 GS/s respectively. Results from each interpolation factor were compared and are later discussed in section 3.4.

1.5.7. Equipment Limitations

To verify that the system had at least one nanosecond resolution to better validate the interpolation, the trigger from the VSG was monitored via a Tektronix TDS7704B oscilloscope. This model of oscilloscope has a sampling rate of 20 GS/s, with a 7 GHz bandwidth, allowing a time resolution of 10 ps/sample. The trigger was set to repeat every 83.760 µs. Thus, the trigger has an average rise-time of 954.26 ps, with a standard deviation of 100.2 ps, throughout 43752 acquisitions. Thus, the maximum theoretical time resolution for the overall system is approximately 1 ns, equivalent to the factor of two interpolation. However, to see the effects of increased interpolation and instability of higher interpolation factors, the eight and sixteen-times interpolation were still observed. A screenshot from the oscilloscope can be seen in Figure 10.

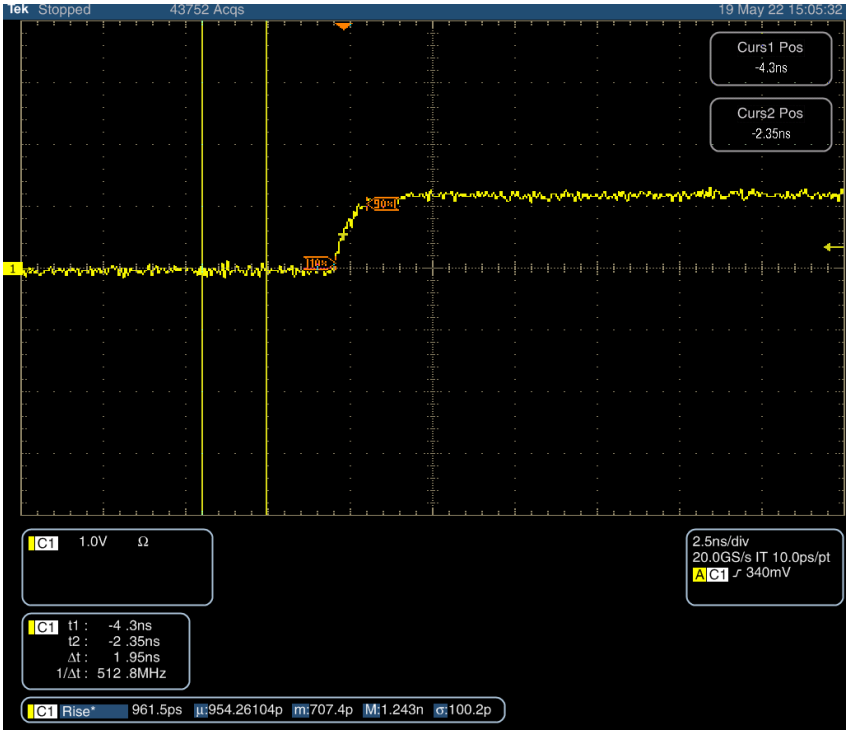

Figure 10: Screenshot of the VSG trigger using a high-sampling rate oscilloscope

2. Electrical Characterization of Silicate Sandcast

2.1. Experimental Setup

Due to the expensive nature of high frequency equipment, the sand casts had to be characterized on an electromagnetic level, to verify that the proposed imaging method was not prevented by this casting media. Multiple waveguides were designed to hold finely crushed sandcasts to perform testing. This methodology was adopted from a previous graduate student at Montana Technological University, measuring the electrical properties of different fluids in a drill pipe, using the pipe as a waveguide [19]. Three waveguides with nominal inner diameters of 19.05, 25.4, and 38.1 mm (three-quarter, one, and one and a half inches) were used, each made of 6061 aluminum pipes. All waveguides had variable lengths of 0.61, 0.91, and 1.22 m (two, three and four feet). The waveguides at their maximum length can be seen in Figure 12. To apply energy into the pipe, SMA Amphenol straight jack connectors were selected, as seen in Figure 11. Due to the nature of wave propagation through a waveguide, the connectors antenna had to extend to approximately half of the inner diameter of each waveguide, so pairs of connectors were cut to approximately 0.375 and 0.5 inches for the ¾” and 1” waveguides.

Figure 11: Straight-jack connectors used to launch the waveforms into the waveguides

Figure 12: Each waveguide used in its maximum length configuration

2.2. Waveguide Characterization

From each of the S-parameter curves created, as seen in Appendix A, a cutoff frequency is apparent. Using the cutoff frequency, a dielectric constant can be calculated by applying (10).

$$f_c = \frac{X_{mn} * c}{2\pi * r * \sqrt{\epsilon_{r_{medium}}}} \tag{10}$$

Where c is the speed of light, 2.98E8 meters per second, $\epsilon_{r_{medium}}$ is the dielectric constant of the material in the waveguide which defines a materials ability to store electric energy, r is the radius of the waveguide and X_{mn} is the n_{th} root of the m_{th} order Bessel function derivative, whose values can be seen in Table I.

Table I: n^{th} zeros of the derivative of the m^{th} order Bessel functions

	m = 0	**m = 1**	**m =2**	**m = 3**
n = 1	3.8318	1.8412	3.0542	4.2012
n = 2	70.156	5.3315	6.7062	8.0153
n = 3	10.1735	8.5363	9.9695	11.3459

If equation (10) is rearranged to find the dielectric constant, it goes to the form:

$$\epsilon_{r_{medium}} = \left(\frac{X_{mn} * c}{2\pi * r * f_c}\right)^2 \tag{11}$$

and a dielectric constant can be found based off the cutoff frequency of the waveguide.

Losses in a waveguide can be described by an attenuation constant, α [19]. This attenuation constant can be broken down into two components: losses due to propagation through a dielectric, α_k, and losses due to a conductor, α_c. The break-down of each component and the total attenuation constant can be seen in the following equations, with units in dB/m.

$$\alpha_c \cong \frac{1.08}{r} * \sqrt{\frac{\mu_{r_{pipe}} * \sqrt{\epsilon_{r_{medium}}}}{\sigma_{pipe} * r}} \tag{12}$$

$$\alpha_d \cong \frac{11.81 * tan\,\delta}{r} \tag{13}$$

$$\alpha = \frac{1.08}{r} * \sqrt{\frac{\mu_{r_{pipe}} * \sqrt{\epsilon_{r_{medium}}}}{\sigma_{pipe} * r}} + \frac{11.81 * tan\,\delta}{r} \tag{14}$$

This expression is true when the operating frequency is approximately 1.15 times the cutoff frequency [19], well within the operation zone of the waveguide. Here, $\mu_{r_{pipe}}$is the magnetic permeability of the waveguide pipe, σ_{pipe} is the conductivity of the waveguide and tan δ is the loss tangent of the dielectric.

To solve this equation for the loss tangent, first the attenuation due to the waveguide was found using air as a known dielectric.

To collect this data, a vector network analyzer (VNA) was used to collect the S-parameters of the pipe at the three variable lengths, by applying a known wide-band electrical signal. From the S-parameters, the maximum available gain, known as MAG or G_{MAX}, was calculated using equations (15) - (18) from Pozar [28].

$$\Delta = S_{11}S_{22} - S_{12}S_{21} \tag{15}$$

$$K = \frac{1 - |S_{11}|^2 - |S_{22}|^2 - |\Delta|^2}{2|S_{12}S_{21}|} \tag{16}$$

$$G_{MAX} = \frac{|S_{21}|}{|S_{12}|}(K - \sqrt{K^2 - 1}) \quad (17)$$

$$G_{MAX_{dB}} = 10 \times \log_{10}(G_{MAX}) \quad (18)$$

Here, Δ is the determinant of the scattering matrix and K is the Rollet's stability factor of the system. Now, the calculation for the MAG is only valid for unconditionally stable systems. Stability is defined as where K is greater than one and the magnitude of Δ is less than one [28]. Since this is a passive system, unlike an active device such as an amplifier or transistor, the unconditional stability criteria are always satisfied. The MAG for passive devices can never be greater that one, and any MAG of a value of less than one will be a result of real losses in the waveguide.

As the dielectric constant of air is approximately one, and the loss tangent for air is considered zero, or lossless, all losses in the waveguide will be due to the conductor, or α_c. Operating frequencies capable of operating in TE_{11} mode (the dominant operating mode) are defined as:

$$f = 1.15 * f_{c_{TE_{11}}} \quad (19)$$

where $f_{c_{TE_{11}}}$ is the cutoff frequency of the TE_{11} mode, which will be approximately the same as the cutoff frequency of the S-parameters. The recorded data from the 0.91 mm ID air case can be seen in Figure 13 with the compiled data in **Error! Reference source not found.**.

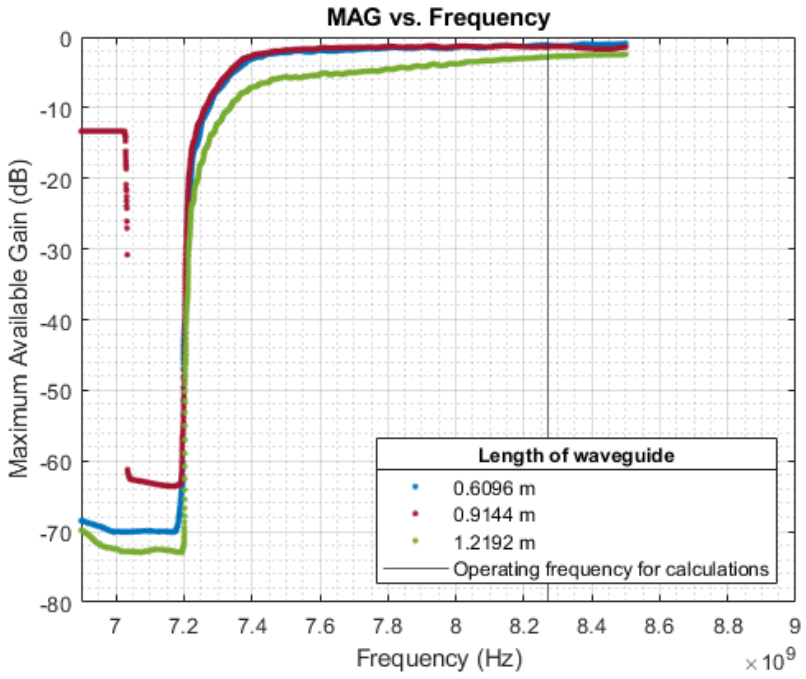

Figure 13: MAG in one-inch ID waveguide at varying lengths, with air as the dielectric

From this data, since the MAG is less than unity, this can be considered the real loss of the system, as previously discussed. The operating frequency, in this case, is approximately 8.27 GHz. Next, a linear least-squares fit is applied to the losses of each case at the frequency specified, and an attenuation constant was approximated. The data can be seen in Figure 14

In the one-inch case, the attenuation constant was found to be approximately 1.7104 dB/m. Next, using equation (14) and substituting the dielectric constant and loss tangent for air, a conductivity for the waveguide pipe is calculated, which was found to be 5.69E6 Siemens/meter.

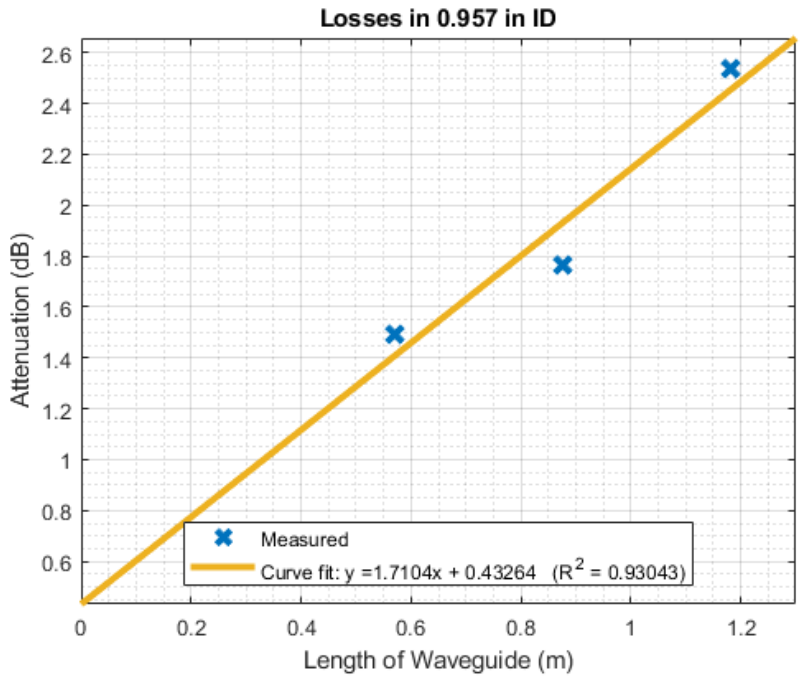

Figure 14: Measured and curve fit losses for one-inch ID waveguide through air

From the collected data, the dielectric constant and the loss tangent were back-calculated and found to be 1.0086 and 8.9338E-4 respectively, indicating an error of around .9% with respect to the dielectric constant of air. As with anything in air, this can depend heavily on atmospheric conditions and was considered negligible. It should be noted however, that the cutoff frequency for the three-quarter inch waveguide was too high to be observed using said VNA, which had a max frequency of 8.5 GHz. The calculated cutoff frequency in Table II was found using equation (10) and the accepted dielectric constant of air, 1.0005. Plots of the S-parameters for each test can be seen in Appendix A.

Table II: Calculated cutoff frequencies and estimated dielectric constant of 1" and 1.5" ID waveguides through air

ID (in)	Observed f_c (GHz)	Calculated f_c (GHz)
0.75	N/A	9.282
1	7.197	7.226
1.5	4.591	4.610

2.3. Sandcast characterization

The waveguides were filled with finely crushed sand casts and the process was repeated from the air measurements, using the calculated conductivity term to calculate the dielectric constant of the sand. The output data summarized in Table III.

From this data it can be concluded that the dielectric constant of the sand cast in question is around 2.57, matching closely with other measurements done by Matzler on quartz-based sand from Lake Superior in Ontario, Canada [20]. The calculated loss tangent was approximately 11E-4. In Figure 15, Figure 17 and Figure 19 the MAG and loss plots can be seen. The extrapolated loss plots can be seen in Figure 16, Figure 18 and Figure 20. The S-parameter plots can be seen in Appendix B.

Table III: Calculated dielectric constant and loss tangent values with cutoff frequency for each waveguide

Nominal ID (in)	**Measured ID (in)**	f_c **(GHz)**	f **(GHz)**	ϵ_r	$\tan\delta$
0.75	0.745	5.8062	6.6771	2.5731	11E-4
1.00	0.957	4.5066	5.1827	2.5674	14E-4
1.50	1.500	2.8721	3.3030	2.5731	10E-4

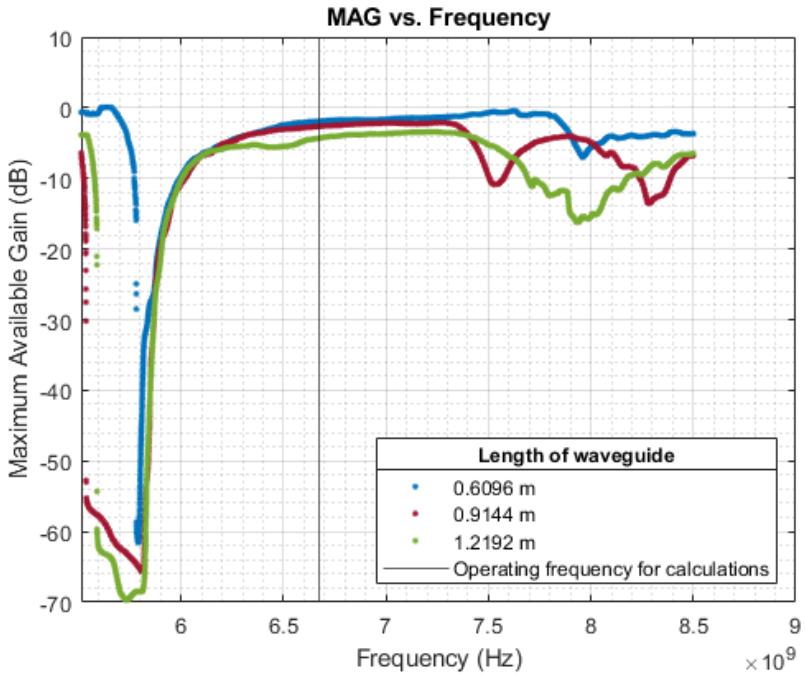

Figure 15: MAG in three-quarter-inch ID waveguide at varying lengths, with sand as the dielectric

With increasing inner diameter, the cutoff and operating frequencies decrease, with the three-quarter inch pipe having the largest operating frequency at 6.67 GHz. With each increase in waveguide length, the attenuation increases, due to the signal propagating through more sand.

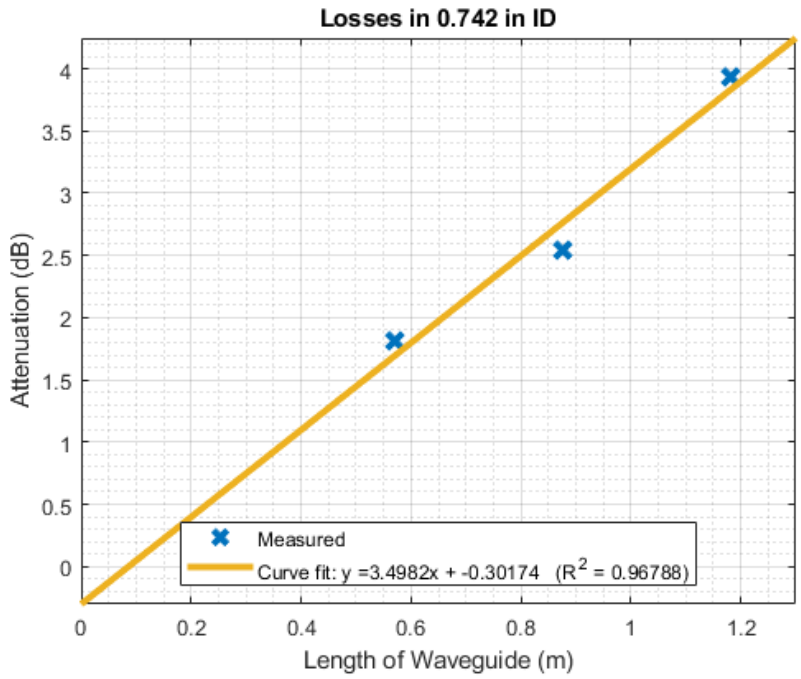

Figure 16: Measured and curve fit losses for three-quarter-inch ID waveguide through sand

The three intersecting points on each curve were then selected again, and the linear fit was applied. In Figure 16, the increasing effect from additional length and sand can be more easily seen, with the trend being closely linear.

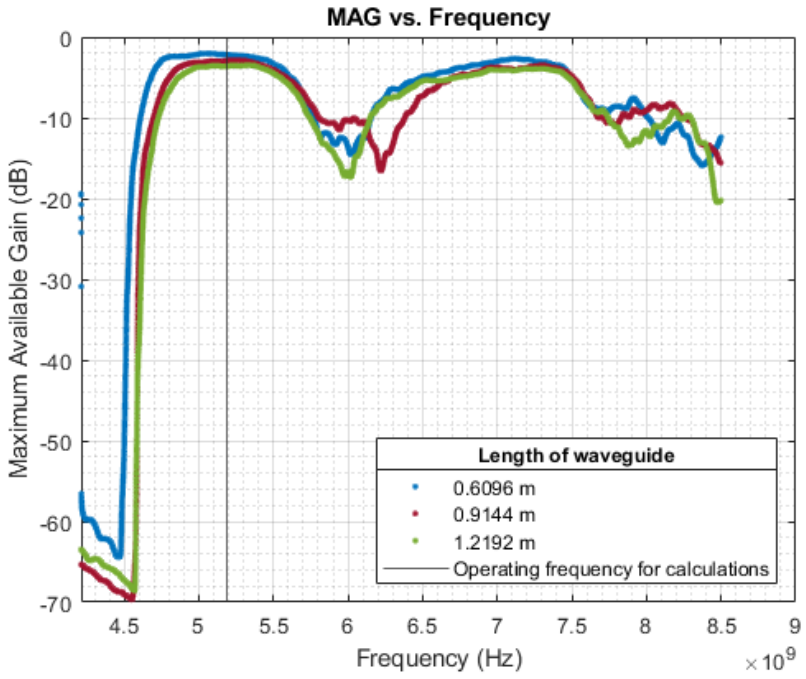

Figure 17: MAG in one-inch ID waveguide at varying lengths, with sand as the dielectric

In Figure 17, the operating frequency chosen was 5.1827 GHz, a smaller frequency than the 0.61 mm ID waveguide.

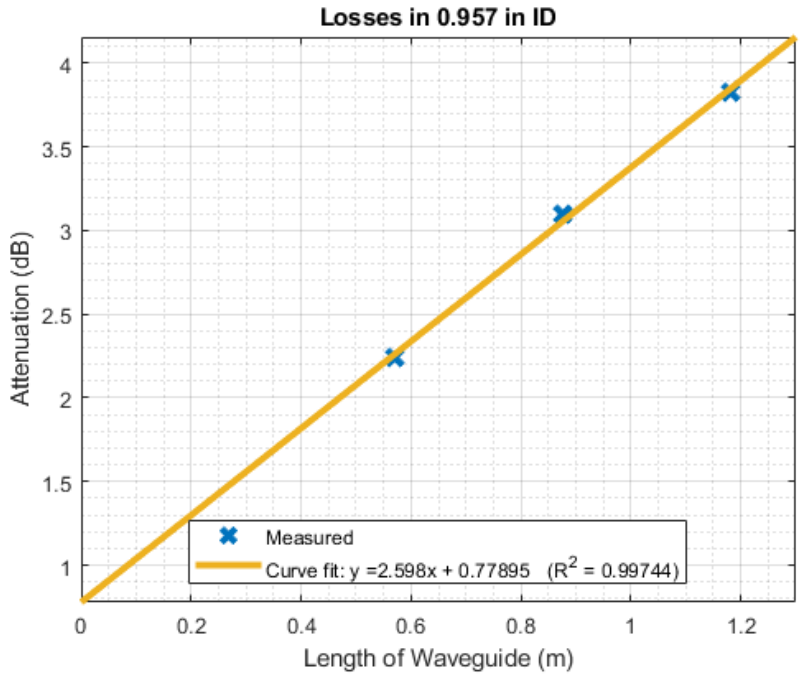

Figure 18: Measured and curve fit losses for one-inch ID waveguide through sand

As with the previous waveguides, the effect of additional dielectric increases the attenuation in the waveguide, with a linear trend. While the y-intercept in the previous case was negative, in the one-inch case, the intercept is positive. This is due to a discontinuity at zero meters, as there will be some additional inherent delay due to the system and can be largely ignored.

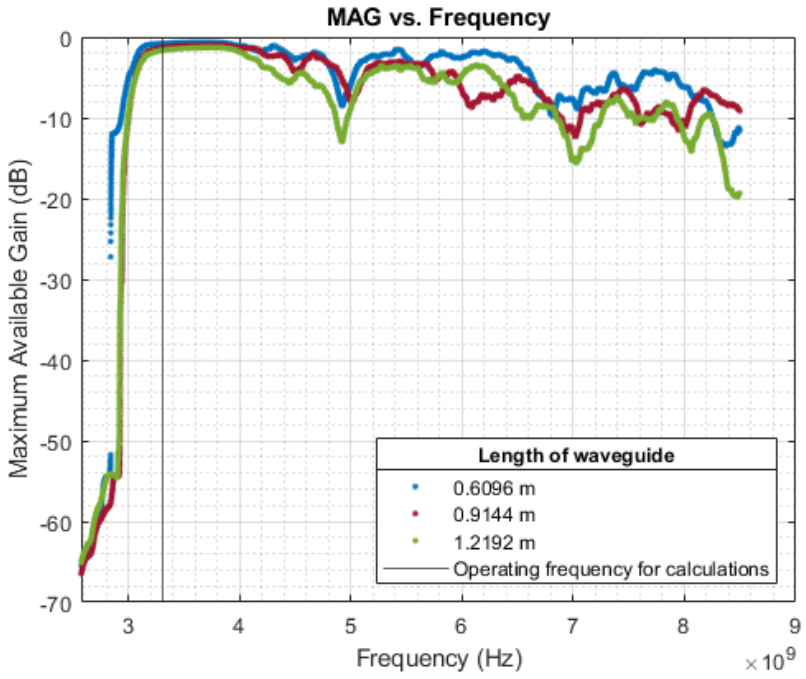

Figure 19: MAG in 1.5-inch ID waveguide at varying lengths, with sand as the dielectric

For the final case, the 1.5-inch inner diameter pipe was used. In Figure 19, the MAG curves are nearly on top of each other, indicating a declining trend of losses with respect to the increasing radius of the waveguide. You can also see this effect in the declining magnitude of the slopes in each of the loss plots.

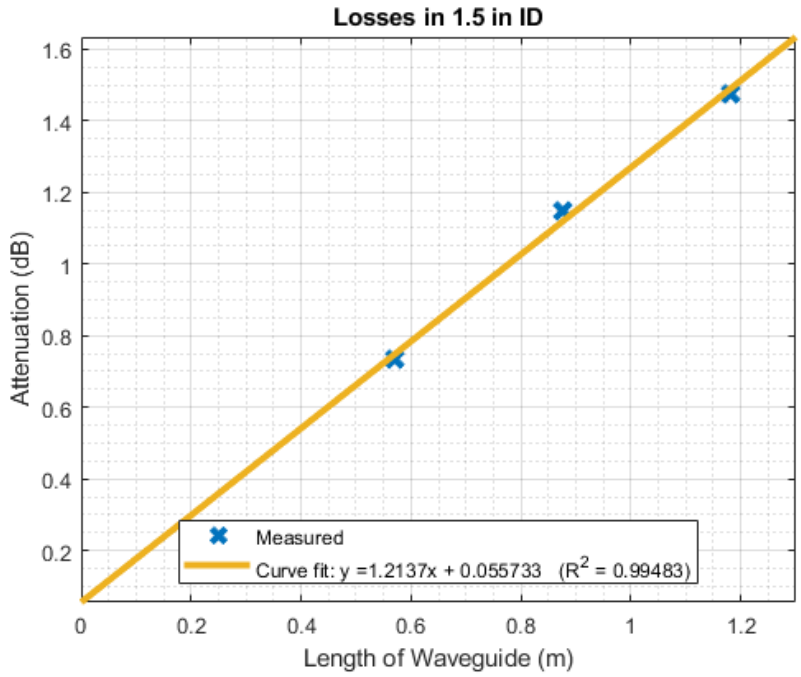

Figure 20: Measured and curve fit losses for 1.5-inch ID waveguide through sand

For the 1.5-inch waveguide, the loss with regards to distance appears to be the least steep, likely due to the change in diameter of the pipe causing the cutoff frequency of the waveguide to decrease. This reduction in viable operation frequency will cause the signal to attenuate less over the same distance, and will increase the signals ability to penetrate the material.

3. Single-path Model Over Open-air

3.1. Experimental Setup

To ensure that whatever path-delay measured was accurate, an experimental setup was created to measure a single-path delay. Figure 21 is a simplified model of a digital wireless communication system. d_i being the data transmitted, sent into the transmitter, thus creating transmission signal $\varphi_{Tx}(t)$. This signal is then transmitted through a propagation channel with frequency response *H(f)*, then added with any noise, $n_o(t)$ or interference, *i(t)* in the channel. The resulting signal, $\varphi_{Rx}(t)$ is received and down-converted to the bit-domain.

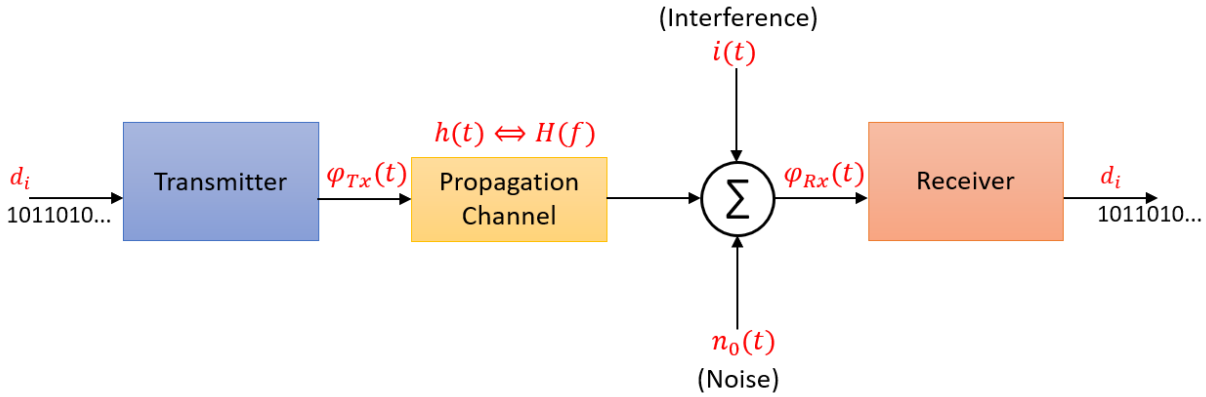

Figure 21: A common model for wireless communication systems

3.2. MATLAB and methodology

Using the model in Figure 21 as a rough outline, d_i is a pseudo-noise sequence of length five (PN5), concatenated eight times with silence periods at the beginning and end of the signal. Once the digital signal is constructed, it is then modulated via BPSK and sent through a raised-cosine filter. Samples of the resultant signal are sent to a VSG60A vector signal generator (VSG). The samples are upconverted to 5 GHz and played at a sample rate of 50 MHz. The resulting signal is then received via a SM200B spectrum analyzer (SA) at 250 MS/s that shares a 10 MHz clock reference and trigger with the VSG. The received samples are then post-processed in MATLAB.

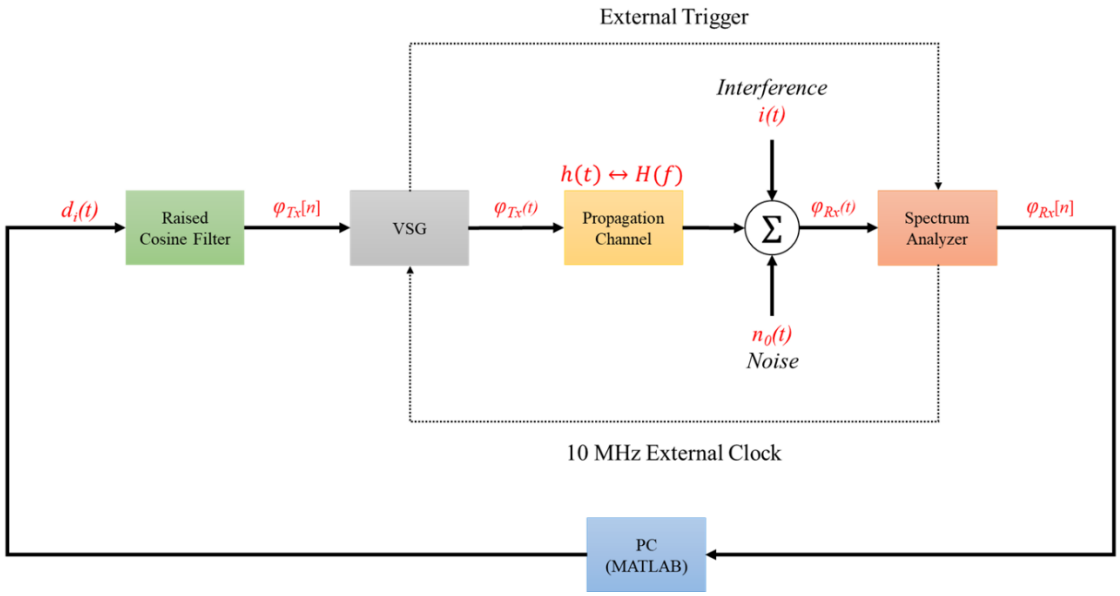

Figure 22: Block diagram of system in use

Once the signal has been received, samples are collected via SCPI, or Standard Commands for Programmable Instruments. These samples are read into MATLAB to calculate the time delay between transmitter and receiver. First, the received samples are read into the MATLAB program then, the ideal samples generated and sent to the VSG previously are interpolated by a factor of five to create an artificial transmitted sample rate of 250 MHz to match the received sample-rate. The transmitted and received signals are then further interpolated by a factor of two, four, eight and sixteen. Resulting in artificial sample rates of 500 MHz, 1 GHz, 2 GHz, and 4 GHz respectively. Each pair of signals are then cross correlated to find the sample delay between the two. The process repeats several times, resulting in an average time delay.

Before any experiments are done, a calibration is performed to ensure any natural time delay in the system, such as filters in the equipment and any delay due to cable lengths, are accounted for. First, a “zero-length” measurement is made to create a baseline. This is done by using an SMA coupler as the propagation channel, adding in theory, zero delay and having a gain

of one. This measurement is then performed several times, and an expected natural time-delay is recorded to be subtracted from the measured time-delay.

3.3. Equipment

3.3.1. Propagation channels

The first propagation channel observed were different lengths of cable, a single path from transmitter to receiver. Lengths of cable from 0.305 to 3.048 meters in 0.305 increments were observed, as well as propagation through different cables of lengths 7.67, 15.34 and 23.02 meters.

The second set of propagation channels were over-air at different distances. Here, two sets of horn antennas with beam width 30 and 60°s were used. The two antennas were pointed at each other and the signal transmitted. Between measurements, the distance between antennas was adjusted, observing the time-delay with respect to separation distance. Different polarities on the antennas were observed to have no effect on the time-delay.

3.3.2. Antennas

For the over-air measurements, two pairs of similar antennas were chosen. One pair having a beam width of 30° and the other with a beam width of 60°. The 30° antennas have a directivity gain of 19-dBi and the 60° antennas have a directivity gain of 13.8 dBi. Both have a frequency range of 4.9 to 6 GHz, and a beam width of 6 dB. To connect to the antennas, SMA to N-type adapters were used. The radiation patterns of both antennas can be seen in Figure 23 and Figure 24.

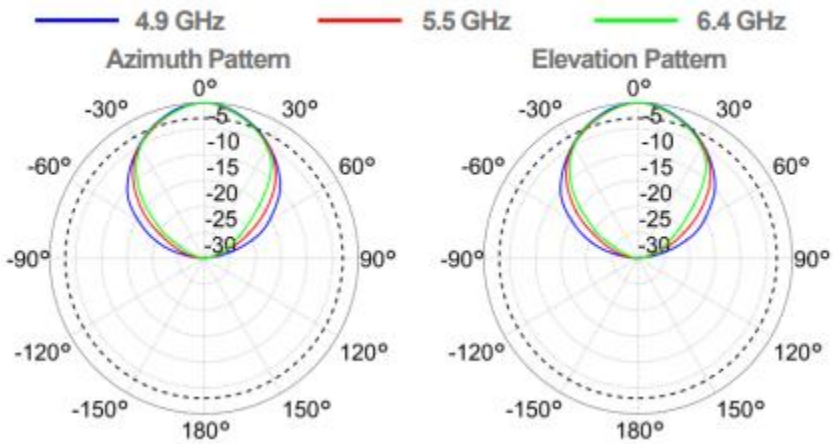

Figure 23: Azimuth and elevation patterns for 60° beamwidth antennas [33]

For the 60° beamwidth antennas, the maximum beamwidth is at -15 dB, about half of the maximum range of the antenna itself.

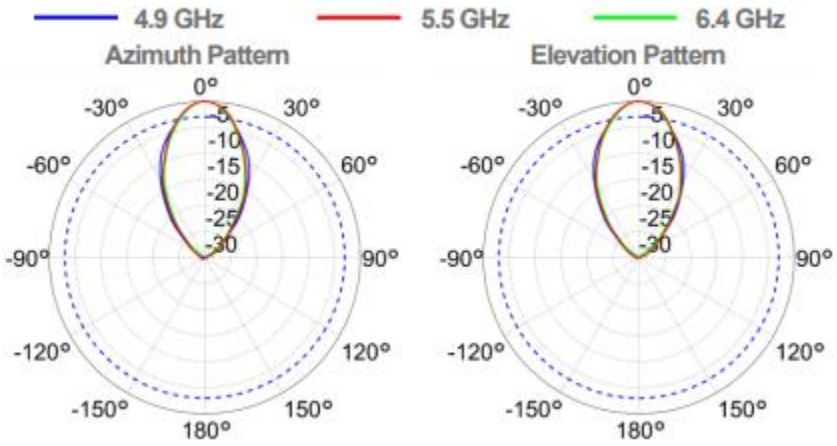

Figure 24: Azimuth and elevation patterns for 30° beamwidth antennas [34]

The 30° beamwidth antennas' maximum beamwidth is somewhere around -20 to -15 dB, approximately the same as the 60.

3.4. Results

3.4.1. Cable Measurements

The results for the cable experiments can be seen in Table IV. Here, the measured delay of each cable length was measured using the same VNA as previously mentioned and is compared to the calculated time-delay from the experimental setup. Each result was a product of

100 averaged measurements, with the average time delay of each interpolation factor per length of cable. The time-delay measured using the MATLAB system matches closely with those measured using the VNA, having a resolution of about 1 ns. A compilation of the cable results can be seen in Table IV.

Table IV: Measured time delays using various lengths of cable with varying interpolation factors

Cable Length (m)	Measured Delay via VNA (ns)	Calculated time delay w.r.t. interpolation factor (ns)				Average Time Delay (ns)
		2	4	8	16	
0.305	1.4	2	1	2	2	2
0.610	2.8	4	3	4	3	3
0.914	4.3	6	4	5	5	5
1.219	5.7	6	6	7	6	6
1.524	7.1	8	7	8	8	8
1.829	8.6	10	9	10	9	9
2.133	10.0	12	10	11	11	11
2.438	11.5	12	12	12	12	12
2.743	12.9	14	13	14	13	13
3.048	14.4	16	15	15	15	15
7.671	30.106	32	30	30	30	31
15.34	60.212	62	60	60	60	61
23.015	90.318	92	90	90	90	91

3.4.2. Indoor Over-air Measurements

After verifying the single-path measurement methodology was within one ns, the same model was applied to over air measurements. Using two sets of horn antennae, with beam widths of 30 and 60°, the same measurements were done as with the cable at varying distances. The propagation channel, in this case, being the distance in air between the antennas. The experimental setup can be seen in Figure 25 and plots of the resultant delay vs distance between antennas can be seen in Figure 25 - Figure 29.

Figure 25: Indoor path-delay experimental setup, used to test differences between both sets of antennas

In Figure 26 and Figure 27, when calculated delay is plotted against the separation distance, the delay appears to oscillate around a linear delay with slope of 3.15 ns /m, or approximately the inverse of the speed of light in air. The oscillations can be attributed to multi-path propagation, since the measurements were done inside in a lab environment, with metal shelves as well as multiple tables, the signal has many objects to reflect off of. Contributing proof of multi-path can be seen in the difference between the 30° and 60° antenna results. The 60° antenna appears to have increased deviations than the 30° antennas. Since the 30° antennas can be thought of as having half of the possible propagation paths, it makes sense that the 60° antennas would have a higher number of reflections.

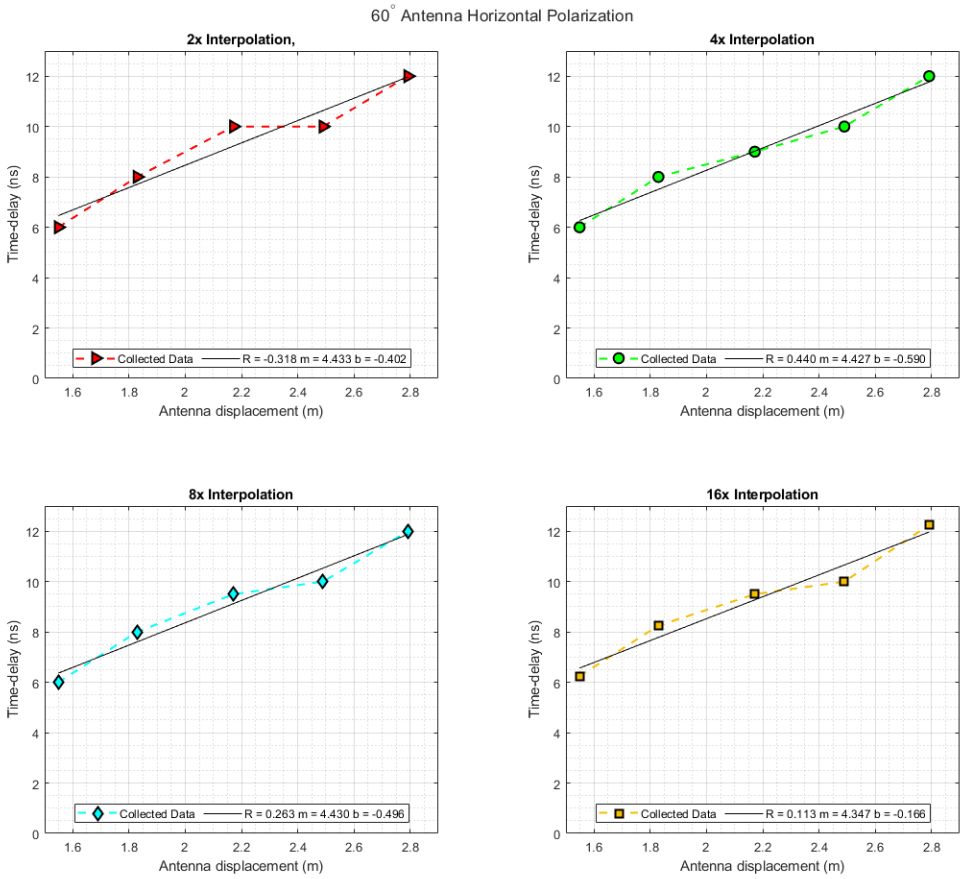

Figure 26: Indoor path-delay measurements, 60° bandwidth, horizontal polarization

In Figure 26, you can see the deviation from the linear relationship between separation distance of the antennas and time delay for the horizontally polarized 60° antenna. The ideal slope of the lines should be the inverse of the speed of light, or approximately 3.33 ns/m, while the delay for this data set is approximately 4.34 ns/m, indicating a large presence of multi-path propagation.

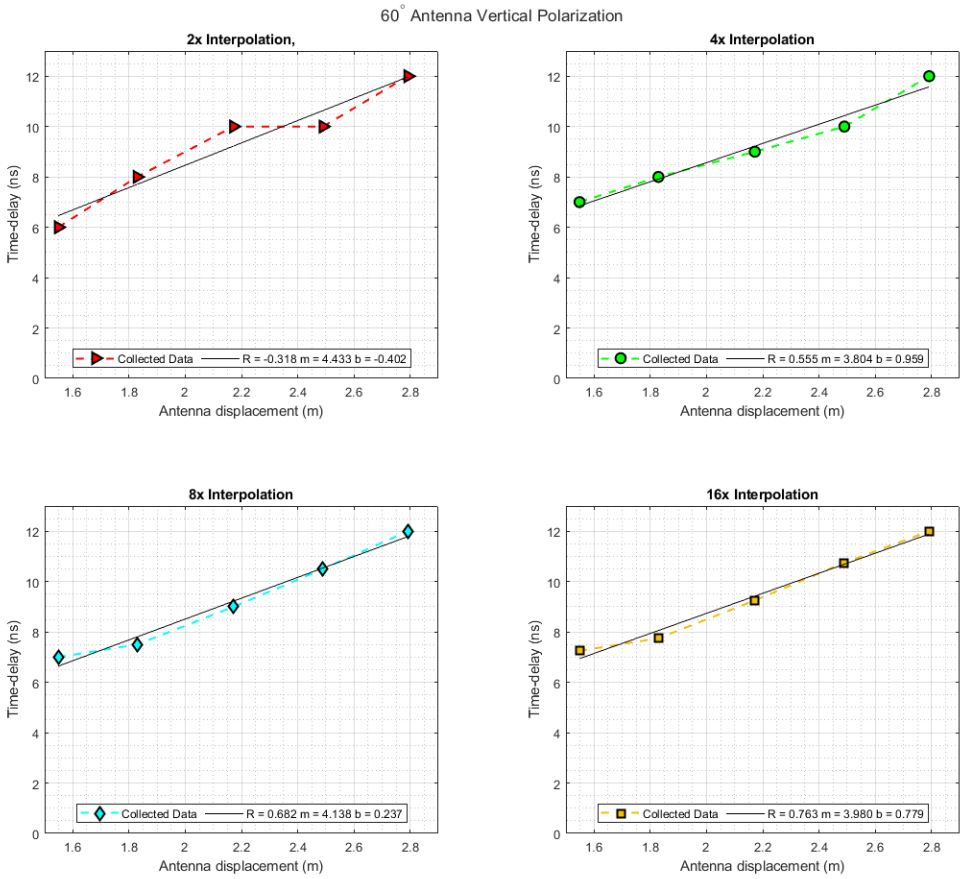

Figure 27: Indoor path-delay measurements, 60° bandwidth, vertical polarization

The vertically polarized results, using the 60° antenna, can be seen in Figure 27. The time-delay using the two times interpolation appears consistent with the horizontally polarized results, with the other interpolation factors varying slightly.

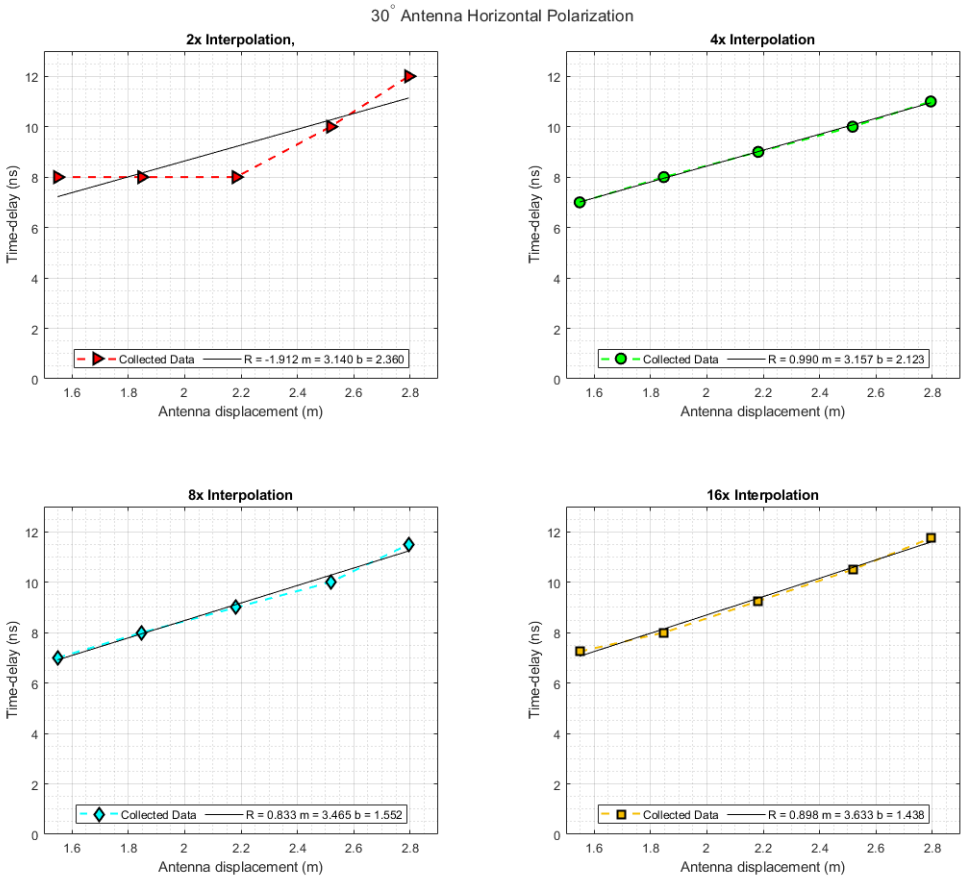

Figure 28: Indoor path-delay measurements, 30° bandwidth, horizontal polarization

Using the 30° antenna, we see a significant change in results, matching more closely with the expected results, with the two- and four-times interpolation getting a delay/m lower than the speed of light, which would be 3.34 ns/m. This can most likely be attributed to experimental and discretization error, as the fit line matches very closely with the collected data. The measured distance in this case may be somewhat inaccurate, leading to a miscalculation in velocity. The data can be seen in Figure 28.

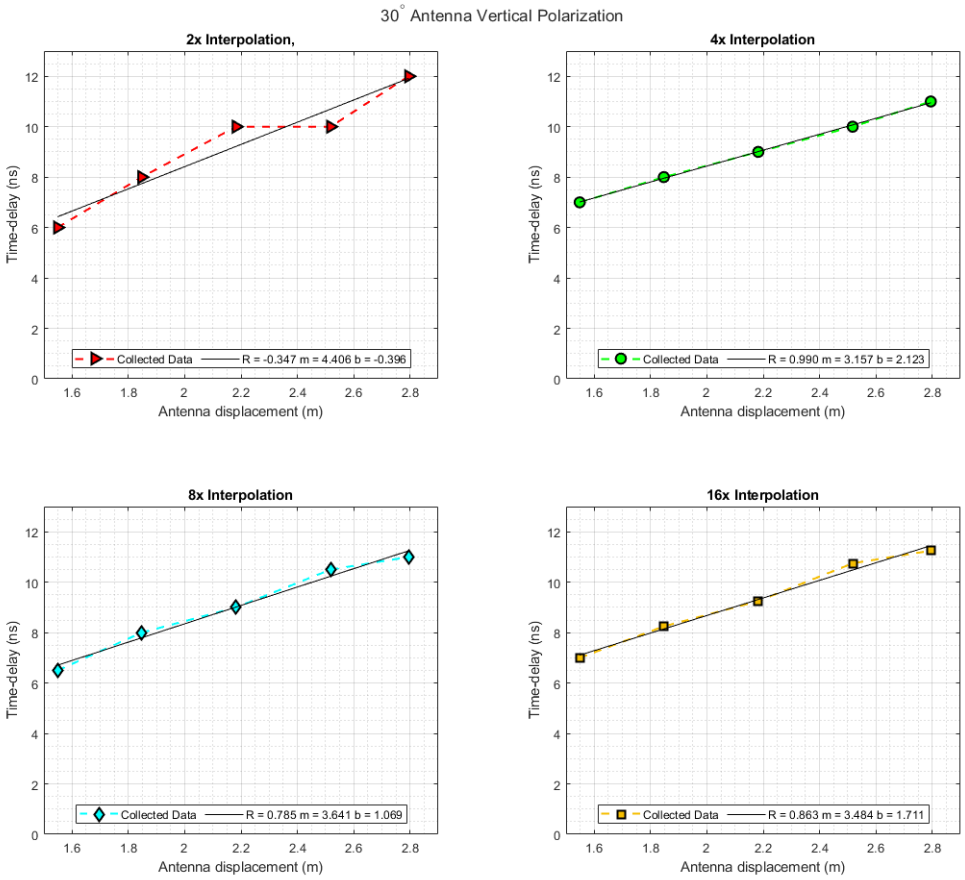

Figure 29: Indoor path-delay measurements, 30° bandwidth, vertical polarization

As with the horizontal results, the vertically polarized data fits much better with the 30° antenna than with the 60° antenna, with the highest correlation coefficient using the 30° antenna reaches 0.990, while the highest using the 60° antenna is 0.763. seen in Figure 29. Again, the two-times interpolation is the worst fit, while the four-, eight-, and sixteen- times interpolation fit much better to the data.

3.4.3. Outdoor Over-air Measurements

The same experiment was then performed outside, to see if the multi-path effect was mitigated. Here, the same measurements were taken with the 30° antennas and over a much wider distance range. The data can be seen plotted against antenna displacement in Figure 30.

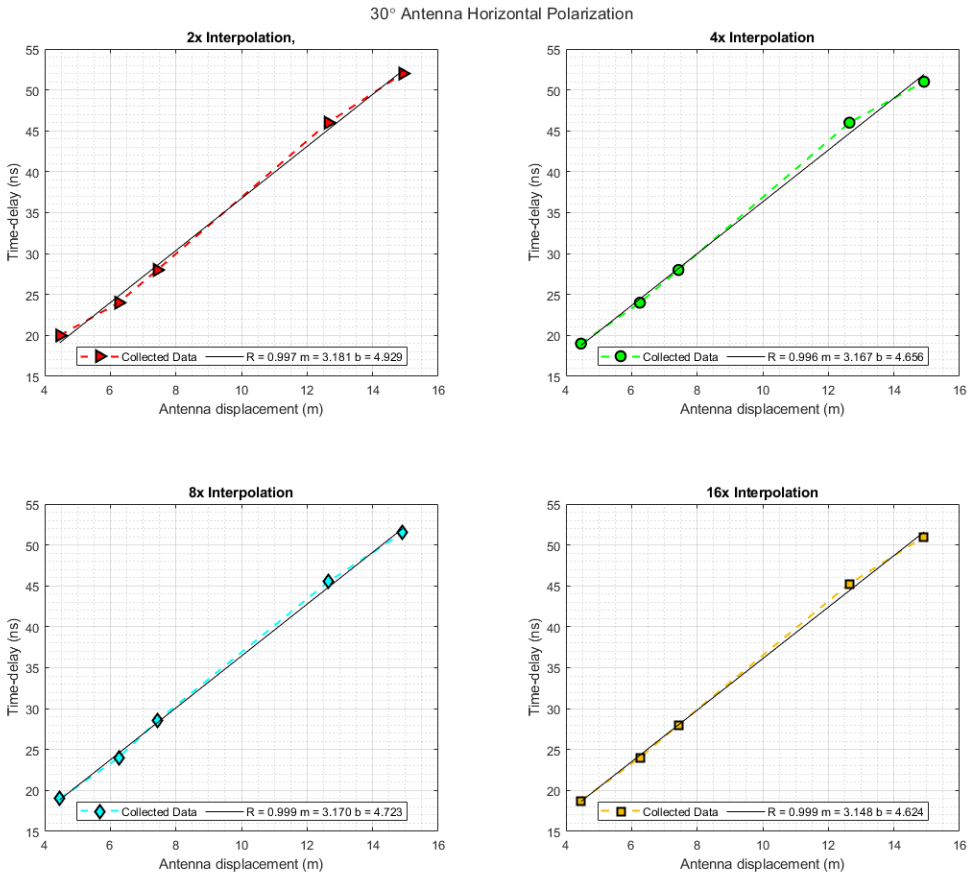

Figure 30: Outdoor path-delay measurements, 30° bandwidth, horizontal polarization

From this data, it can be seen that the deviations due to multi-path propagation have been reduced, with each curve having a much closer spread than the indoor measurements. Again, the delay is smaller than the speed of light, which could be attributed to experimental error.

4. Interference with Metal Sheet

4.1. Metal Suspension Frame

To test whether the system could detect metal, a suspension method was needed to hold a metal plate at a proper height. This was done via a wooden frame created out of 2x4” planks suspended using saw-horse ends. Aluminum metal was chosen, due to aluminums non-ferric nature. The sheet was attached to the frame via machine screws. Measurements were performed on the initial four-feet-by-four-feet, 16-gauge sheet and on a two foot, one-quarter inch by four inch cut of the same sheet. The transmission power on the VSG was set to 0 dBm for each case.

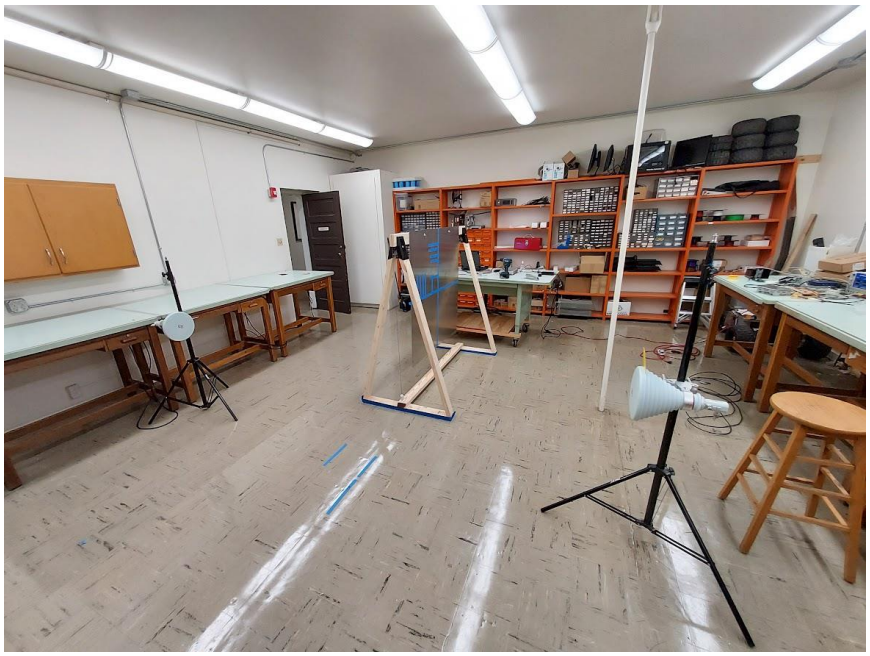

Figure 31: Experimental setup used to test change in path-delay and received channel power with increasing levels of interference

4.2. Experiments

Using the aluminum sheet and suspension frame, the same measurements as with the cables were made, along with received channel power. The antennas’ positions were fixed, and the distance from the metal sheet to the antennas was measured. In each test an average channel power of 0 dBm was used at the transmit side, while the SA had a reference power of -20 dBm.

4.2.1. Fixed Antenna, Blocking Test

For the first test, the metal plate was placed equidistant from both antennas and moved into and out of boresight, or the direct path, of the antennas. The frame was moved at centimeter steps, measured using a laser rangefinder attached to the metals edge and channel loss and time-delay were calculated. For the "zero-length" reference, the cables used to connect to the transmitter and receiver's respective antenna were connected using an SMA through. The distance from each antenna was marked with tape, to ensure the changing angle of incidence remained the same. Here, the distance where the metal edges, wooden frame leg and the center of metal were in boresight were recorded by measuring their distances from the edge of the plate. For this test, the antenna polarizations used were horizontal, vertical, and 45°-slant.

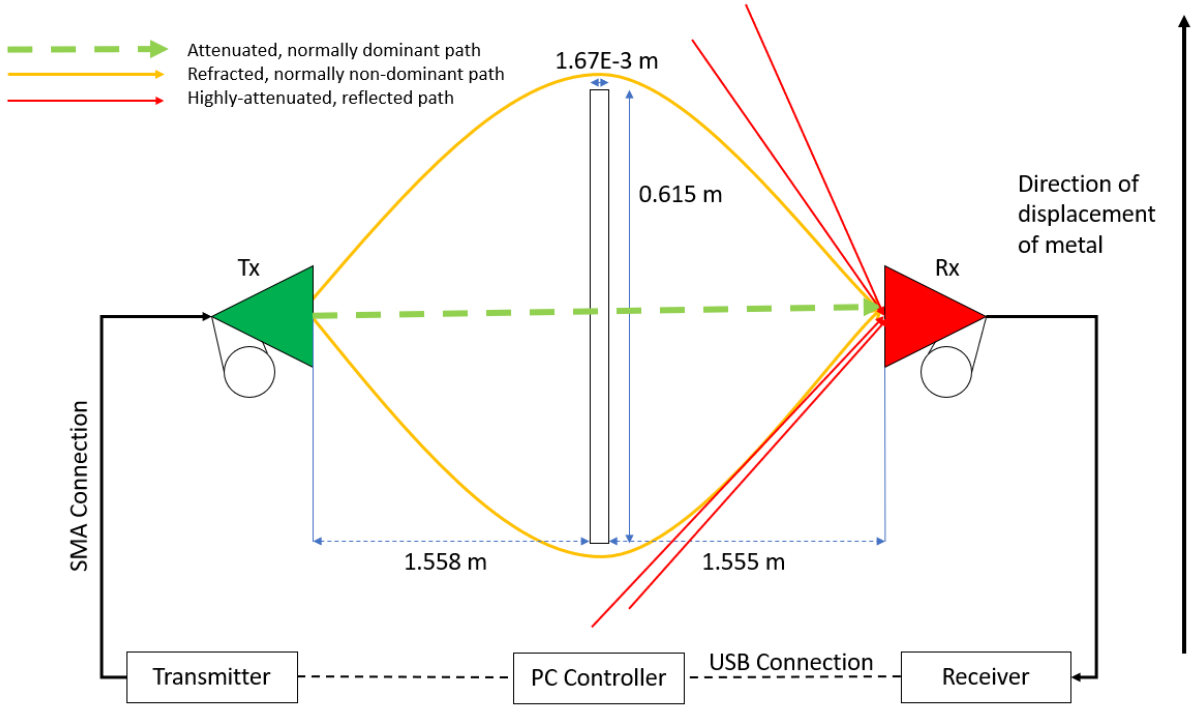

Figure 32: Diagram of the Blocking test experimental setup from an overhead view

With these measurements, the time-delay appears to become negative, indicating that the waveform has increased in velocity from the speed of light. These results lead to reason that the signal loss has become great enough that the correlation between transmitted and received has broken down, leading to the time-delay calculation to become unreliable. This effect can be seen in both the horizontal and vertically polarized measurements.

As for the 45°-slant polarized results, the same cannot be said. This is likely due to 45°-slant polarization having greater signal reliability than either horizontal or vertical, due to propagating in both planes. While the received power is similar to that of the other two sets, the time-delay is not as affected, indicating that the signal still has several paths available, while the signal is still being blocked.

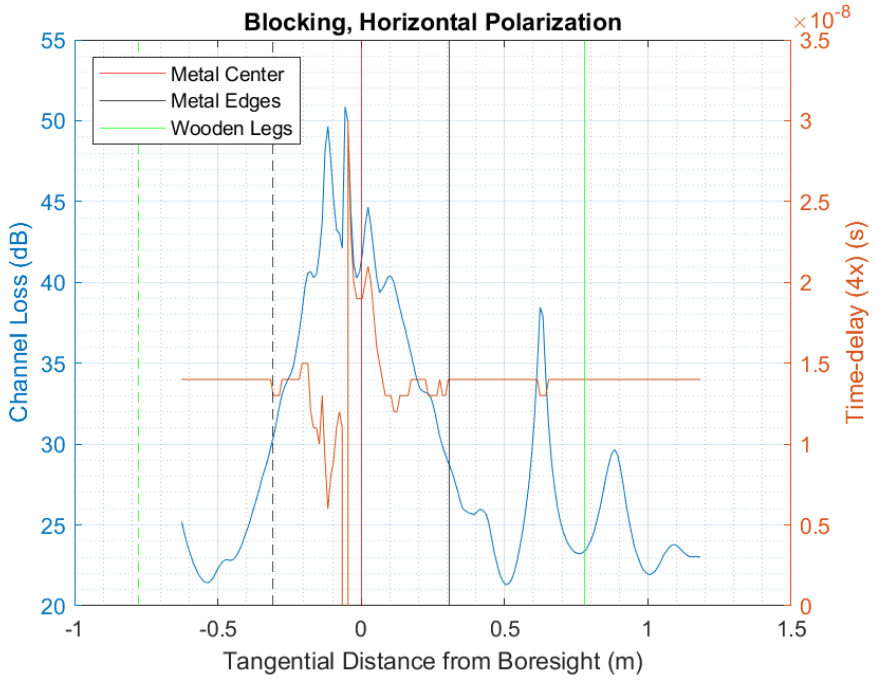

Figure 33: Experimental results using horizontal polarization during blocking test with the metal sheet

In Figure 33, the time delay and received power of the system can be seen. The x-axis indicates the distance from the direct line-of sight path to the center of the metal The time-delay used was the four times interpolation, as that is the maximum theoretical resolution of the

system. As the metal sheet begins to enter the propagation channel, the time-delay begins to steadily increase or decrease in magnitude, while the received channel loss increases steadily, reaching a maximum at approximately boresight. Once the metal leaves boresight, the received channel loss returns to relative normalcy. Due to the dimensions of the room used for measurement, and the size of the frame, the entire setup could not be sent through the channel entirely.

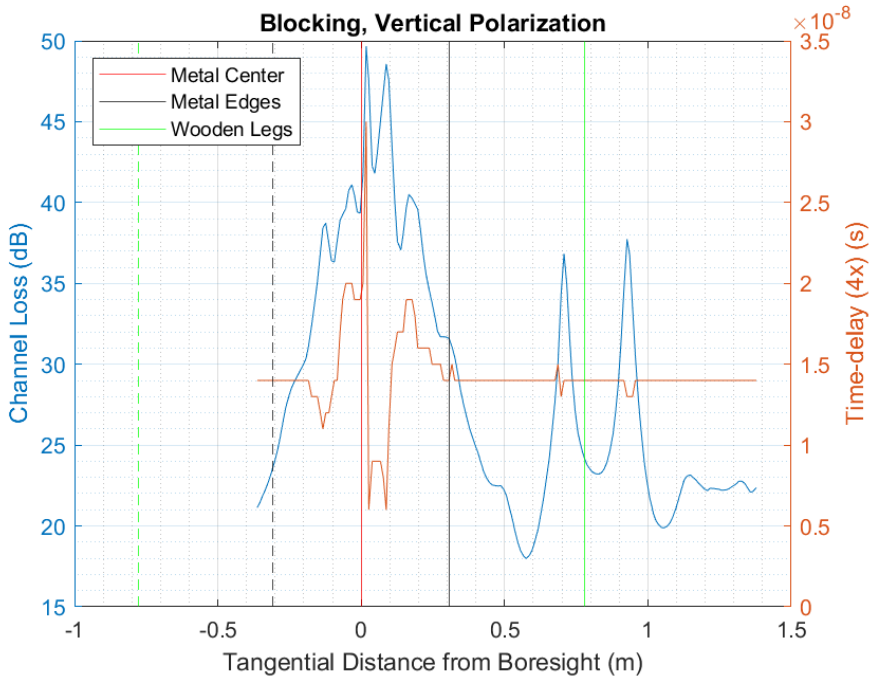

Figure 34: Experimental results using vertical polarization during interference test

As for vertical polarization, which can be seen in Figure 34, we see the same behavior as the horizontal. The loss steadily increases and decreases as the metal enters and leaves the propagation channel, while time-delay increases and becomes more erratic, then returning back to its initial value.

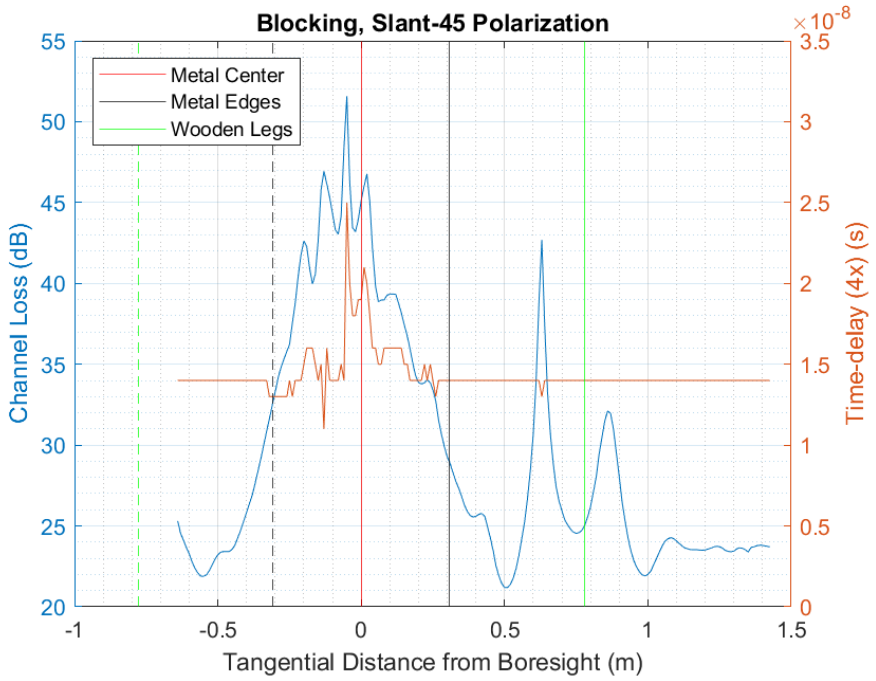

Figure 35: Experimental results using 45-slant polarization during interference test

The last polarization used was a 45°-slant, as seen in Figure 35. Here, a different behavior is seen in the time-delay. The time-delay appears to increase until reaching a maximum around boresight, then decreases back to its initial value. One reason for this would be the geometry of the metal sheet. Since the sheet is taller than it is wide, this would allow for a larger number of paths around the sheet, causing the effect of the sheet on the multi-path propagation of the system to be lower than that of horizontal or vertical polarization.

In each of the results, a trend can be seen around where the wooden legs are present. A ripple effect both before and after the leg where measurements were taken can be seen. This is likely due to the partial blocking of the signal caused by the wooden leg, blocking different Fresnel Zones as it passes through. This blocking would interfere with Fresnel Zones responsible for constructive and destructive interference at the antenna, causing certain locations of the leg to actually improve the received signal power, while others increase the loss. However, blocking

either type of Fresnel Zone would also cause an increase in time-delay, as the signal still must either travel through the leg, or around it.

4.2.2. Frame Cancellation (Blocking Test)

To make sure that the measurements observed were only due to the metal plate, post-processing was used to subtract the frames response from the metal plate measurements, after taking independent measurements with the frame. In Figure 36, a best-fit curve was fit to each dataset using cubic interpolation. Both curves were evaluated over the same range of distances as the metal data. The new evaluated datapoints from the wood frame curve were subtracted from the metal curve datapoints. This process was done for the horizontal, vertical, and 45°-slant datasets. The generated curves for other tests, with their respective data can be seen in Appendix C.

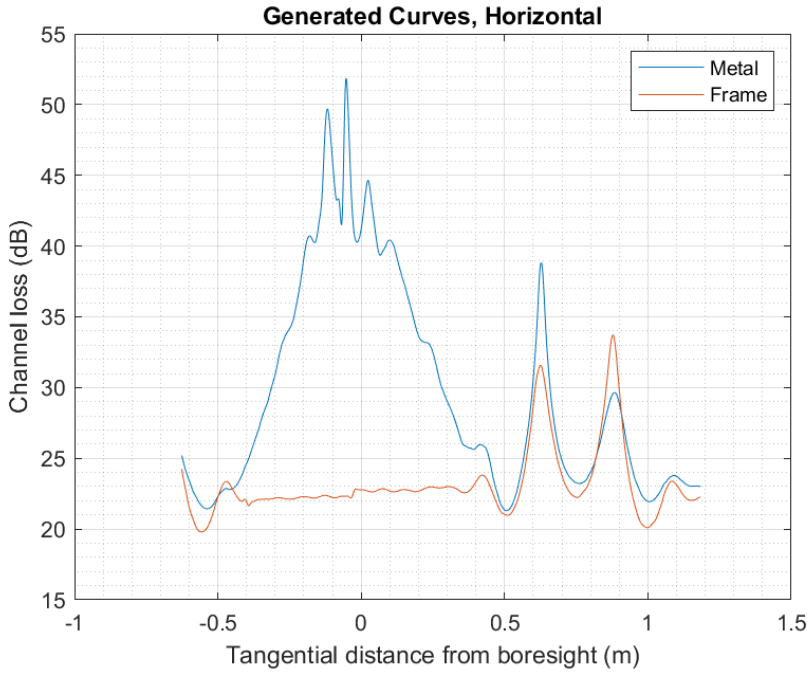

Figure 36: Experimental results using horizontal polarization during interference test and baseline testing

In Figure 36, the received power vs. distance curves from both testing with and without the metal sheet can be seen. At the approximate location of the first wooden leg, peaks in

channel loss are present in both cases, with some differing magnitude, leading to the theory that the losses due to the frame could be subtracted out.

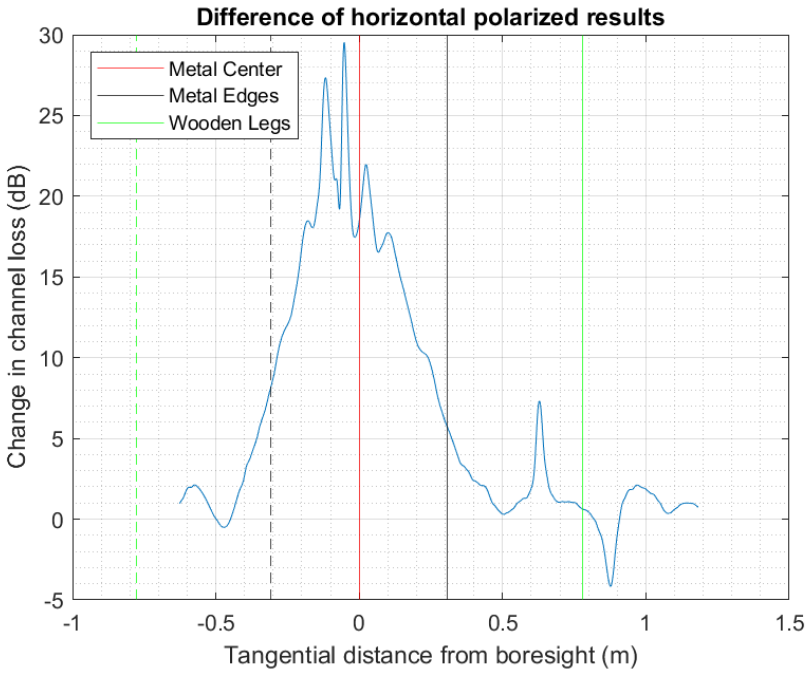

Figure 37: Difference of data curves from horizontal polarization

The result of the subtraction can be seen in Figure 37. The peaks are still present, but at much lower magnitudes, one of the peaks even being overcompensated for, while the portion due to the metal sheet is largely unaffected.

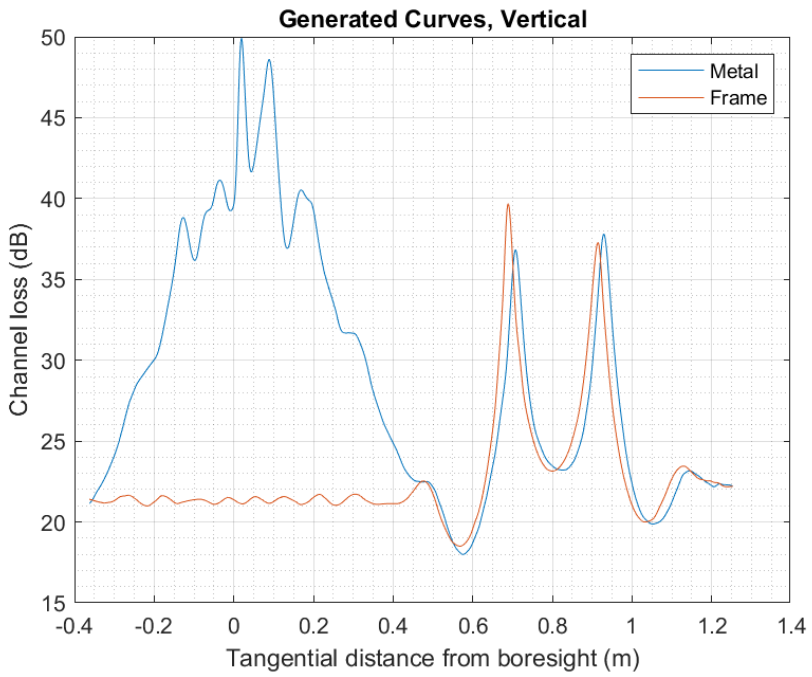

Figure 38: Experimental results using vertical polarization during interference test and baseline testing

As with the horizontal, the vertical results from both tests can be seen in Figure 38. Again, the peaks present due to the wooden legs are easily seen, and the wooden frame experiment results are subtracted from the metal sheet results.

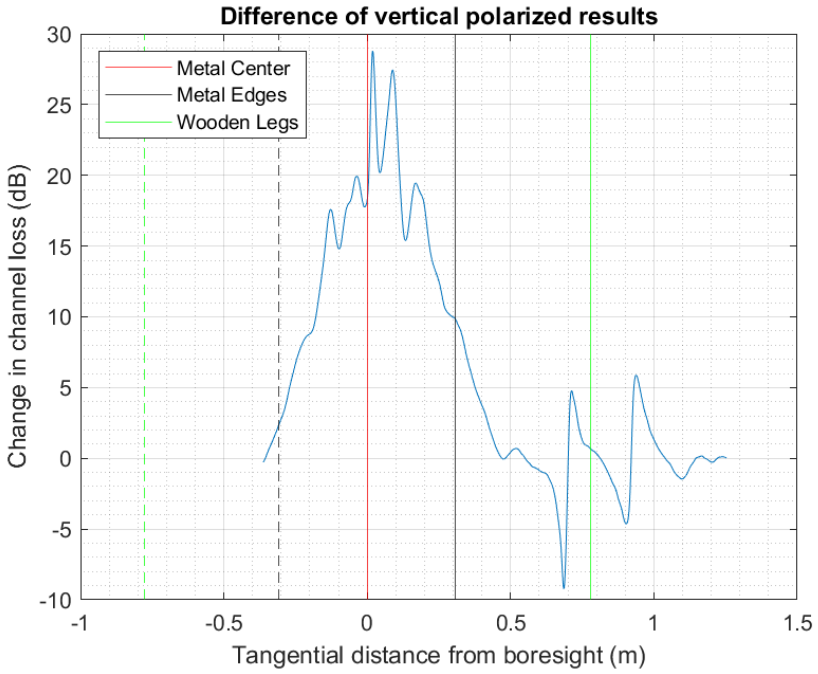

Figure 39:Difference of data curves from vertical polarization

Again, as with the horizontal, the difference is taken and a loss due to the metal sheet can be estimated. In Figure 39, due to the peaks being slightly offset, the interference due to the frame has been reduced, but not eliminated. This slight difference in peak location is likely due to experimental error. If the peaks from the frame measurements were shifted slightly to the right, the peaks would be eliminated, resulting in a flat response.

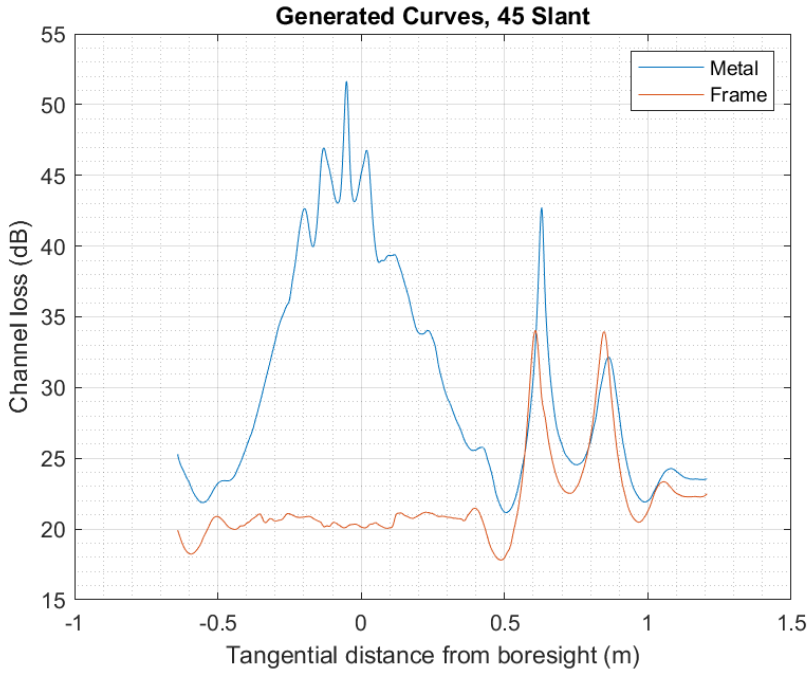

Figure 40: Experimental results using 45-slant polarization during interference test

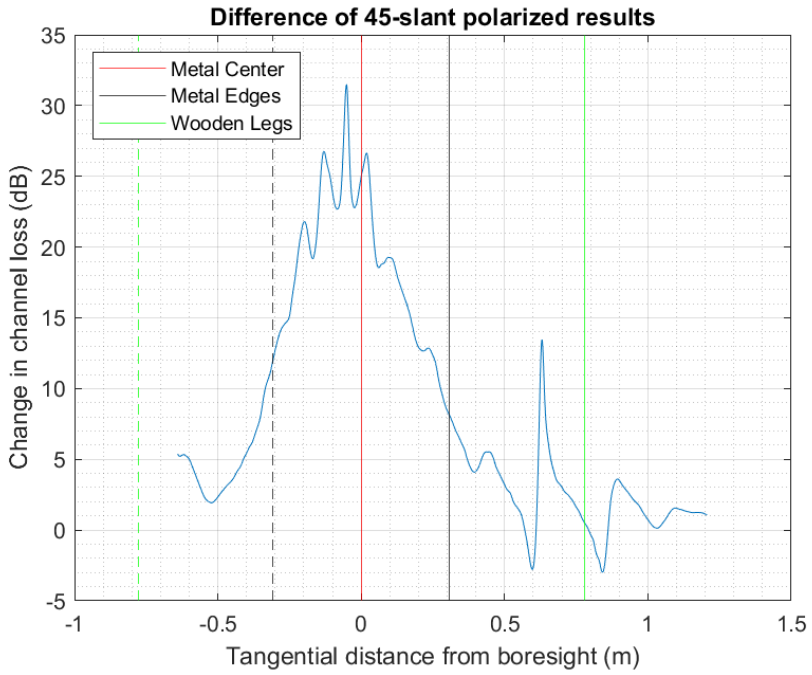

Figure 41: Difference of data curves from 45-slant polarization

4.2.3. Fixed object, changing angle

The next test that was explored was fixing the object in position, equidistant from both antennas, with the antennas moving in azimuth. Antenna azimuth angle was measured using a fixed protractor on the tripod attached to the antenna. A top-down diagram of the setup can be seen in Figure 42. The polarizations used for this case were horizontal and vertical. As with the blocking test, a reference measurement was taken of the setup, without the metal plate. Based on the blocking test and preliminary testing, the antennas were brought closer together, increasing the chance that the metal object will block the signal completely. The data collected from preliminary testing can be seen in Appendix E.

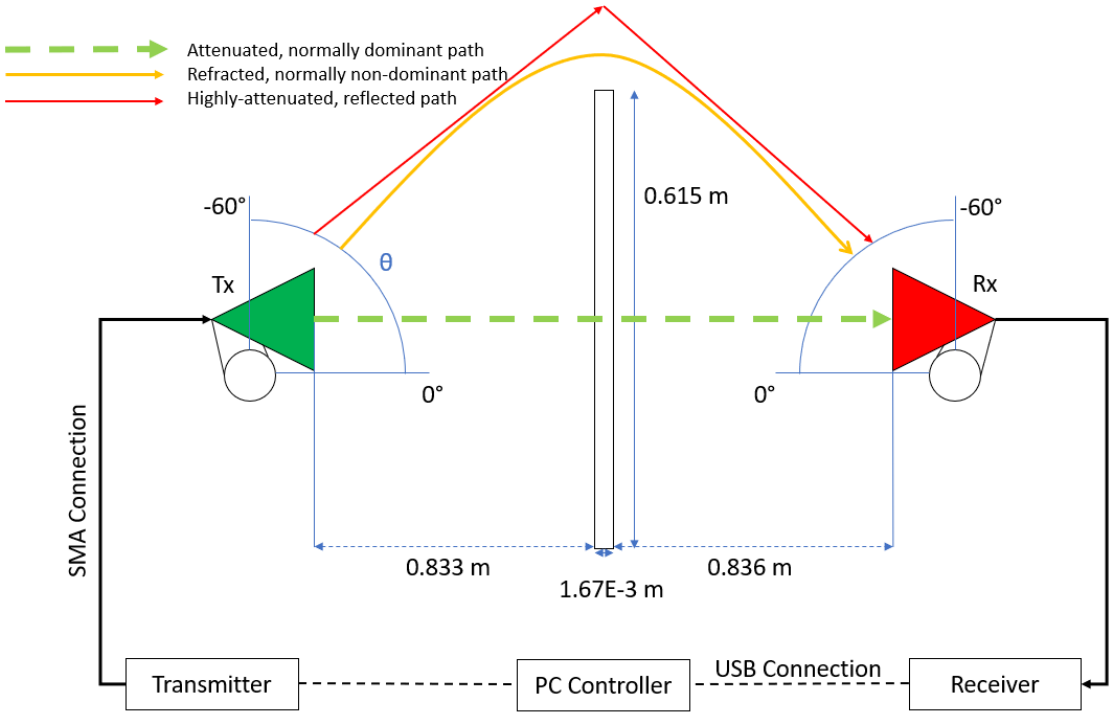

Figure 42: Diagram of the fixed object, changing angle experimental setup from an overhead view

From the results in Figure 43 - Figure 46, it becomes plain that a greater difference can be observed between the horizontal and vertical polarization. The horizontally polarized results have a much wider range of attenuation once the metal edge is reached, while the vertical

appears to remain constant. Due to the metal object being taller than it is wide, the horizontal polarization should not be blocked as much as the vertical, with the signal making its way around the object.

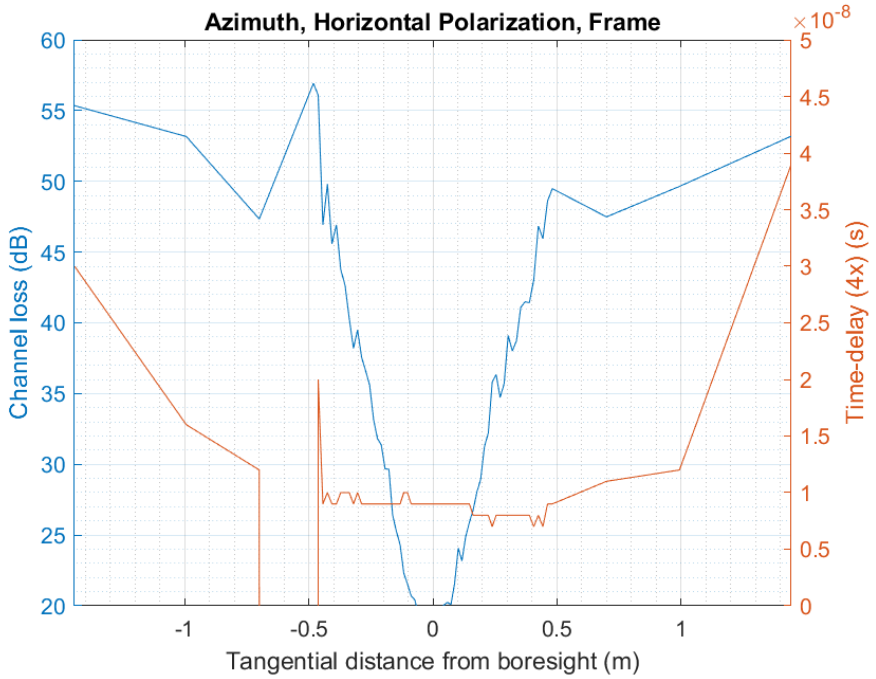

Figure 43: Azimuth testing results using horizontal polarization with wooden frame

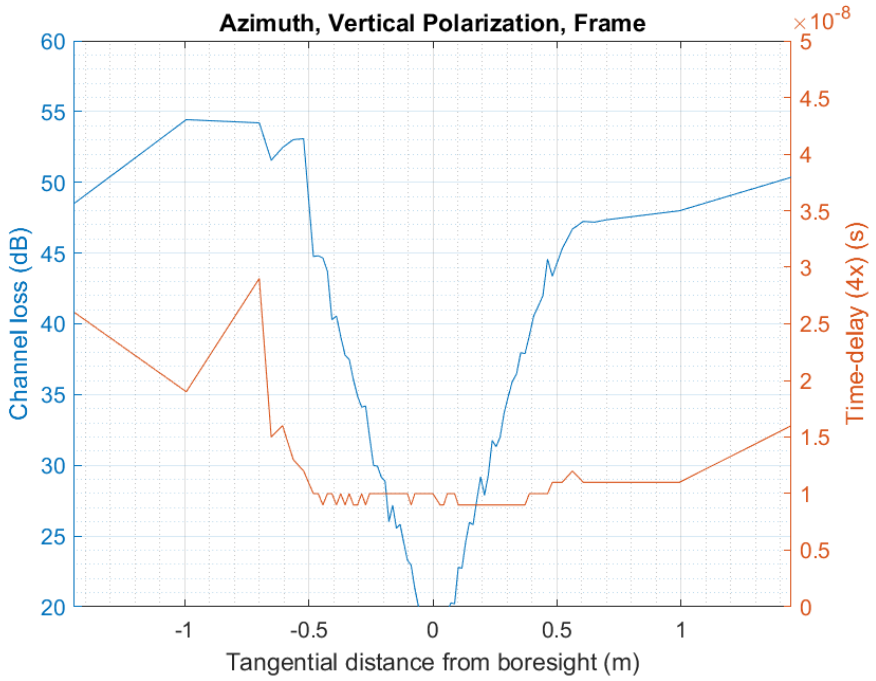

Figure 44: Azimuth testing results using vertical polarization with wooden frame

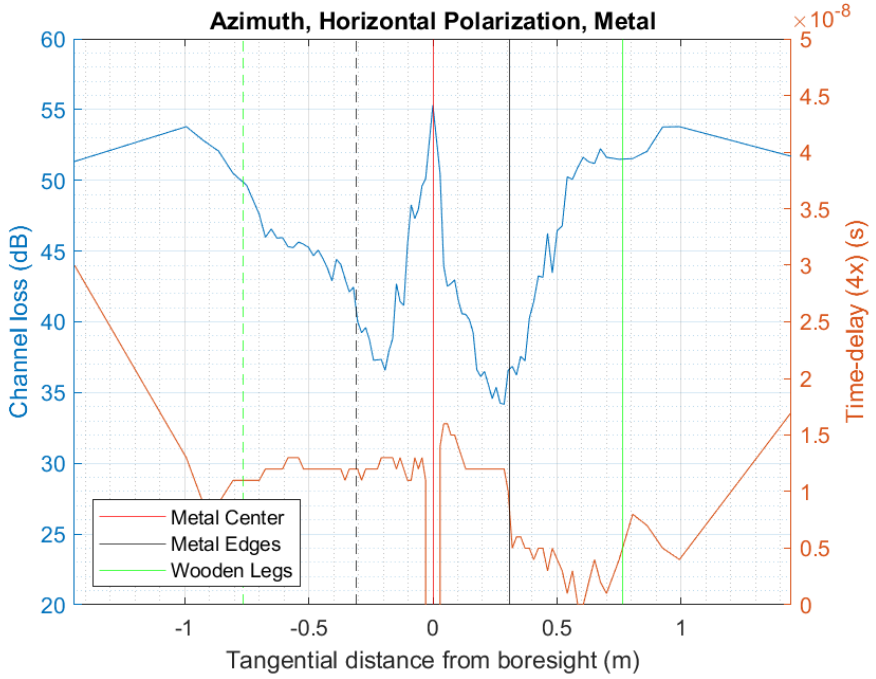

Figure 45: Azimuth testing results using horizontal polarization with metal plate

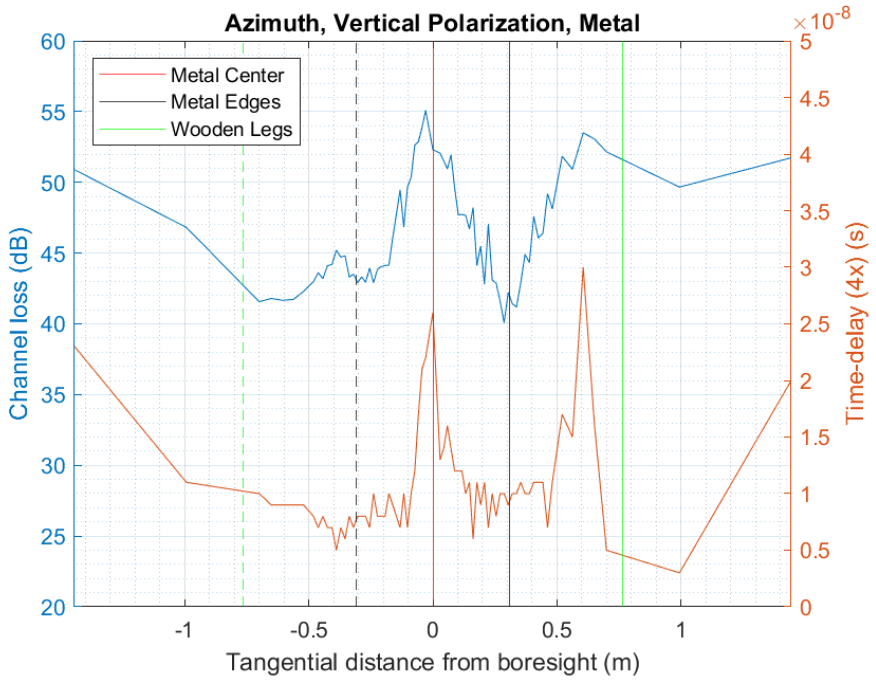

Figure 46: Azimuth testing results using vertical polarization with metal plate

4.2.1. Frame Cancellation (Changing Angle)

As with the blocking test, the results from the baseline test were subtracted from the experimental results by fitting a curve to both and evaluating them over the same distance. The resultant difference can be seen in Figure 43 and Figure 44.

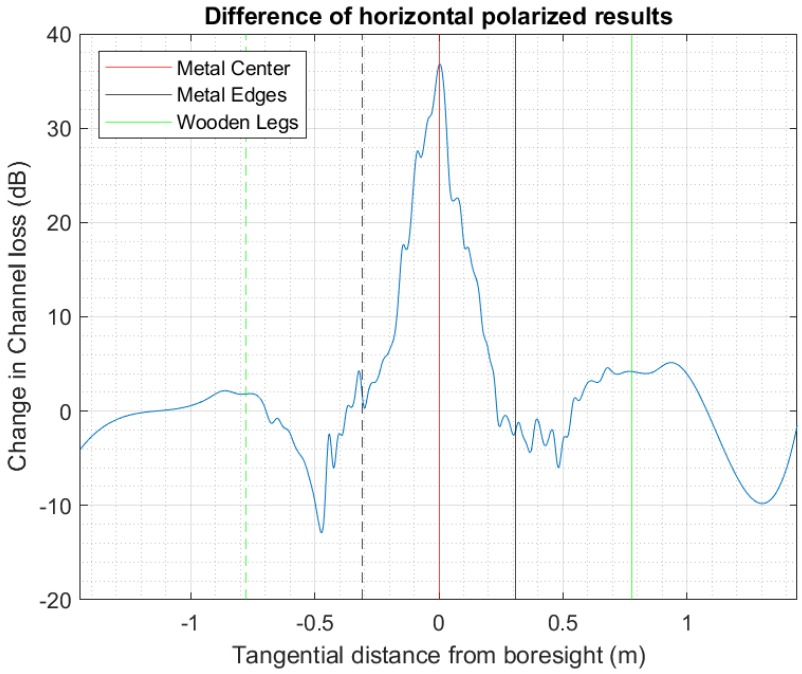

Figure 47: Difference of generated curves from azimuthal testing, horizontal polarization

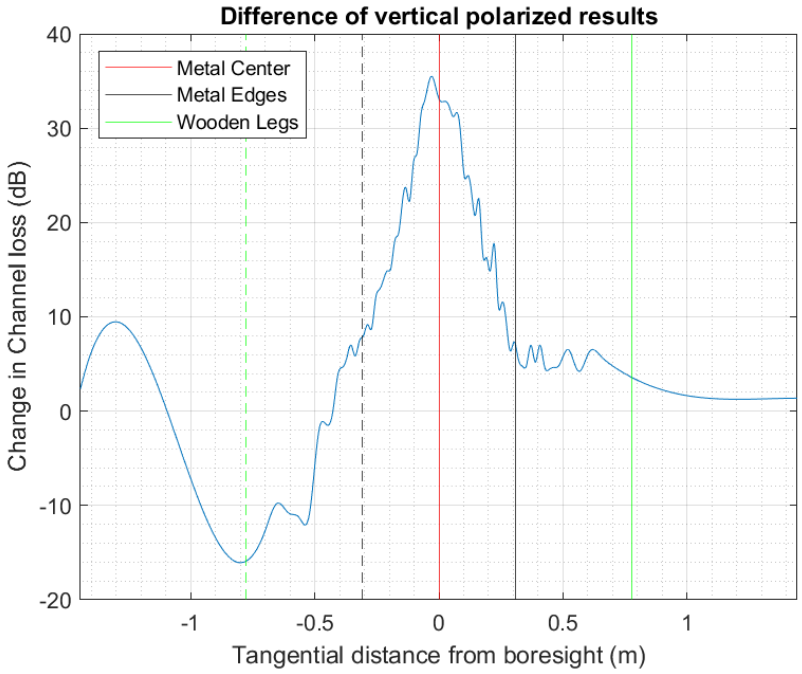

Figure 48: Difference of generated curves from azimuthal testing, vertical polarization

4.2.2. Reflection Testing (Set One)

The third test was reflection. With both antennas on the same side, and the object placed at a fixed, equal distance from both, the transmit and receive antennas azimuth angle was swept. As the transmit antennas azimuth angle was set, the receive antennas angle was adjusted to match that of the transmit to allow for the most optimal reflection to be the dominant path. A diagram of the setup can be seen in Figure 49. Two antenna separation distances, denoted as S in Figure 49, and two distances from the metal sheet, denoted as d, were used.

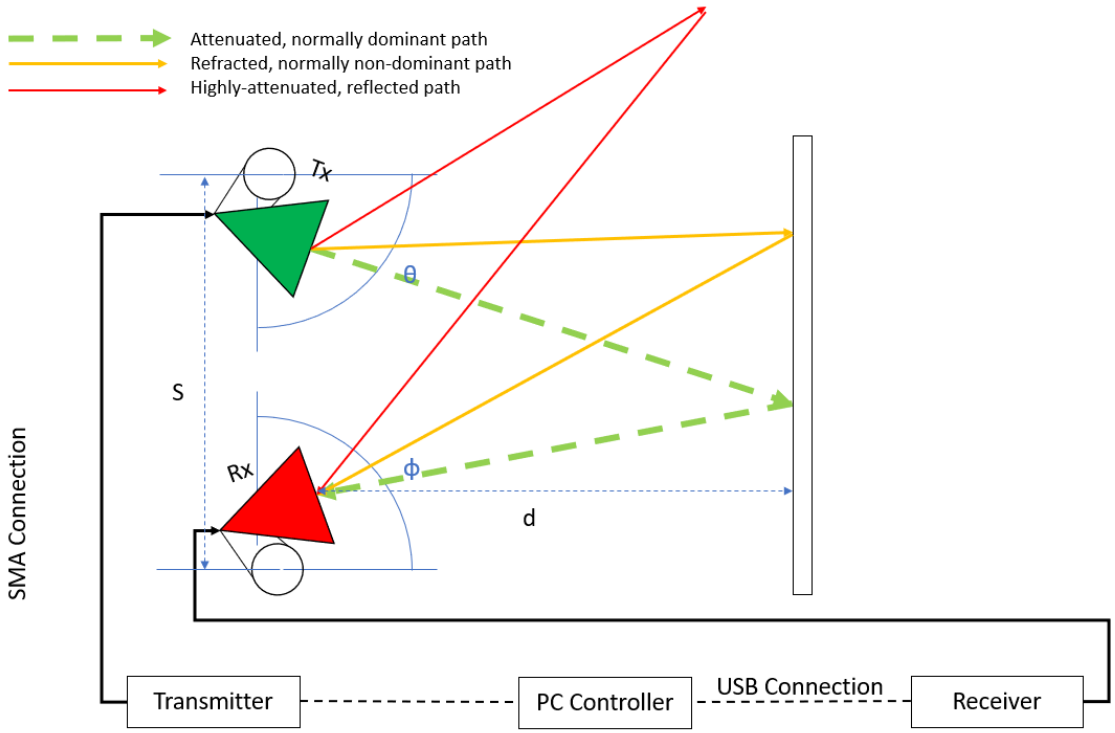

Figure 49: Diagram of initial reflection test

The two separation distances used were 1.22 m and 2.11 m, while the two distances from the plate used were 0.833 m and 1.544 m respectively. Horizontal and vertical polarizations were used. Here, later distance from bore site is defined as the distance from where the antennas were pointed at the center of the metal sheet.

From the results seen in Figure 50 - Figure 53, a different trend arises than the previous tests. The vertical appears to have a more stable time delay response than that of the horizontal. This is due to nearly the entire signal being reflected, again a result of the geometry of the metal. The horizontal can only get partial reflections, resulting in a more chaotic trend. The horizontal also has much larger oscillations, again due to the partial reflections, reflecting select Fresnel zones at a time, while the vertical remains constant. Due to the nature of the reflections, this makes sense. Since the vertically polarized signal will be either completely reflected or not reflected at all and will result in a lower perceived resolution. Meanwhile, the horizontally polarized signal will have a much wider range of losses, due to having different degrees of partial reflection.

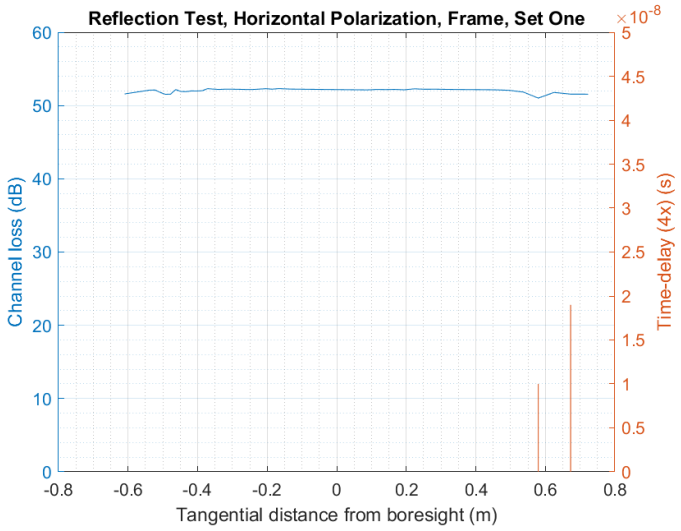

Figure 50: Reflection testing results using horizontal polarization with wooden frame

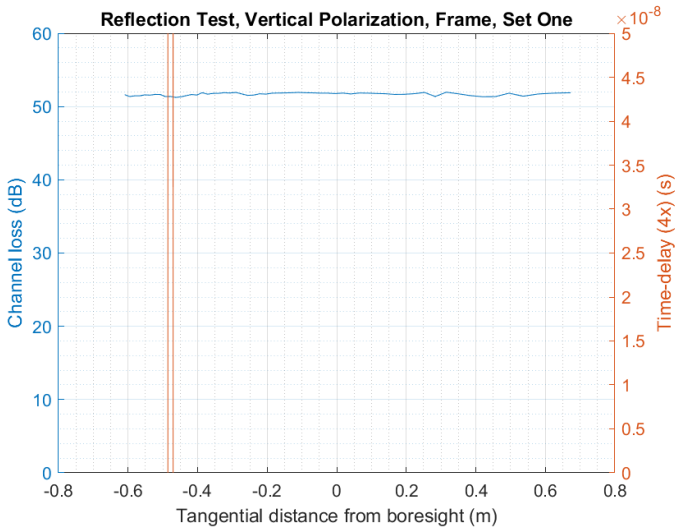

Figure 51: Reflection testing results using vertical polarization with wooden frame

In both Figure 50 and Figure 51, the baseline measurements are quite flat without a reflecting object, indicating minimal reflections in the room, and that any reflection received by the system will be due to the metal sheet itself.

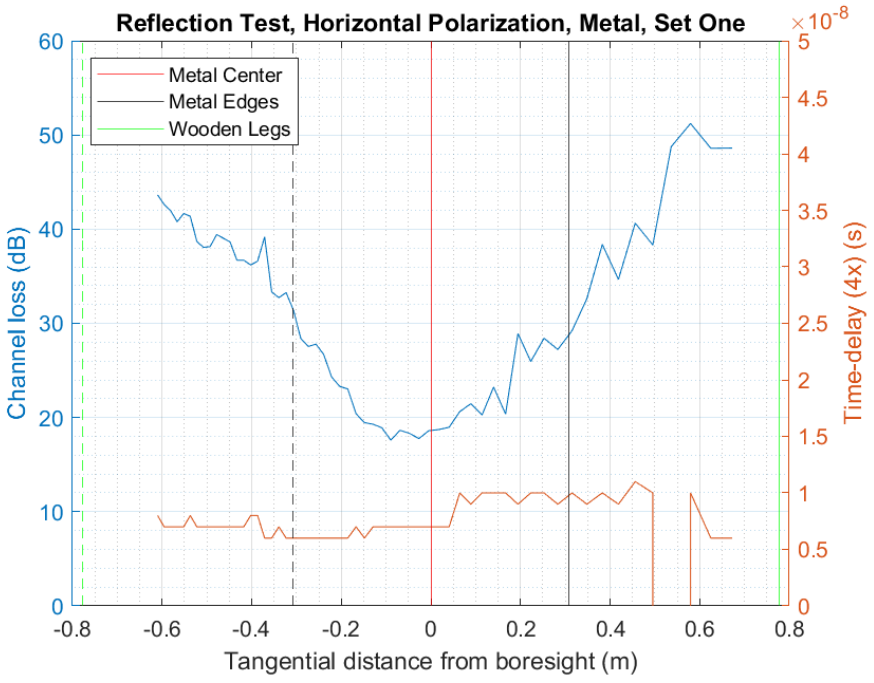

Figure 52: Reflection testing results using horizontal polarization with metal sheet

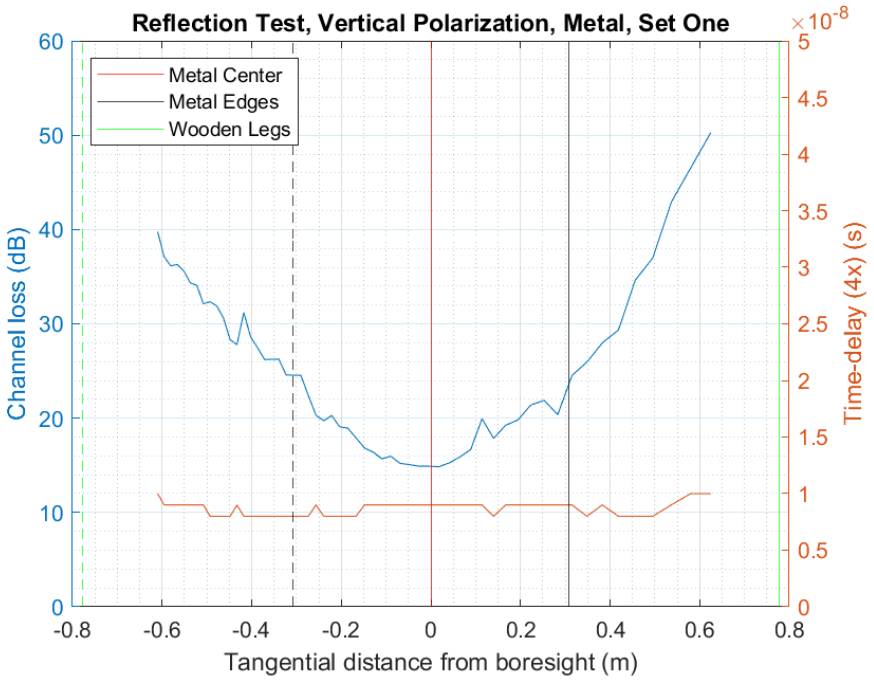

Figure 53: Reflection testing results using vertical polarization with metal sheet

With the metal sheet present, the time-delay when using the horizontal polarization (Figure 52) appears to be somewhat chaotic, or at the very least, more so than the vertical (Figure 53). This effect is caused by the differing height and length of the metal sheet, causing the horizontally polarized signal to reflect partially off of the metal sheet, while the vertical reflects more completely, having a larger surface to reflect off of.

4.2.3. Frame Cancellation (Reflection Testing First Set)

For the baseline measurements, seen in Figure 50 and Figure 51, the response is flat, due to a lack of reflecting objects in the channel. This causes the corrected results to appear like the noncorrected.

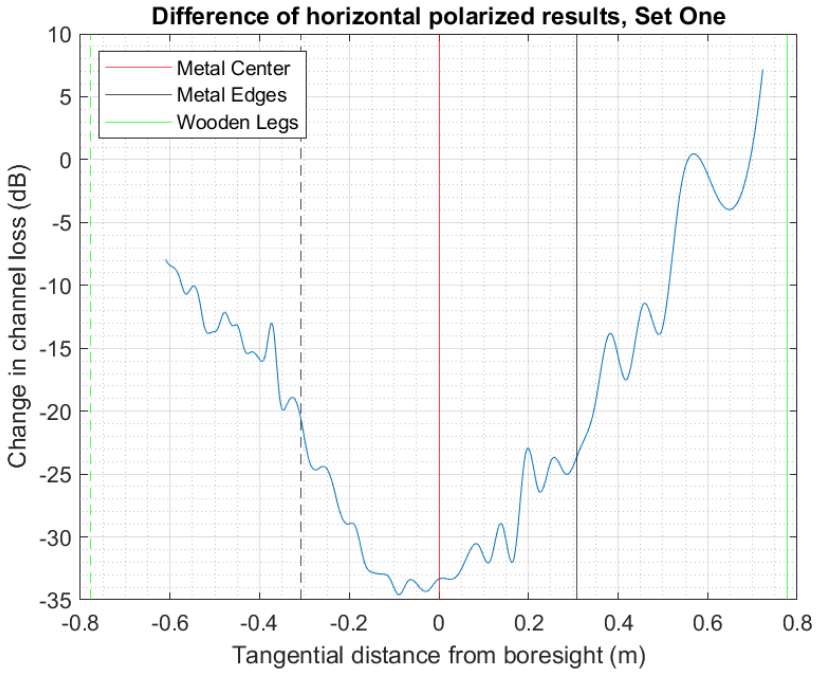

Figure 54: Reflection testing results using horizontal polarization with wooden frame

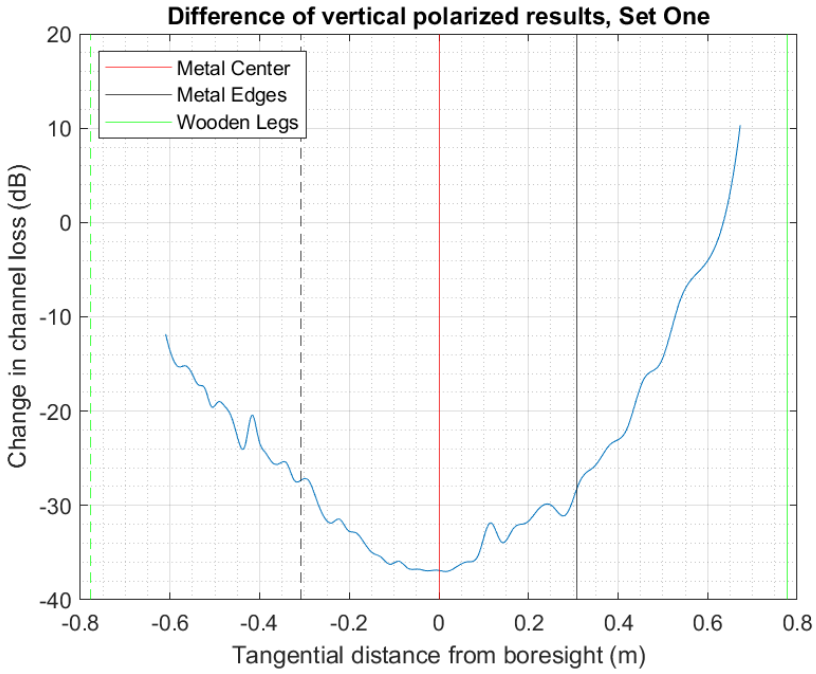

Figure 55: Reflection testing results using vertical polarization with wooden frame

Again, the vertically polarized results remain more stable throughout the measurements, while the horizontal oscillates throughout.

4.2.4. Reflection Tests (Second Set)

For the second set of reflection tests, the separation distance (S) used was 2.11 meters, and the lateral distance from the sheet (d) was 1.544 meters. The results can be seen in Figure 77 - Figure 80. Here, the magnitude of the baseline time delay results from the wooden frame were much larger than those previous.

With regards to the metal results, the time-delay was more stable than at the closer distance. For the vertical power results, the slope was less steep than with the horizontal, due to the geometry of the metal sheet itself. With this test, the power did not seem to oscillate as much as previous tests, which may be caused by the object being in the channel, at least partially, at all times, leading to the most dominant Fresnel zones being present throughout the experiment.

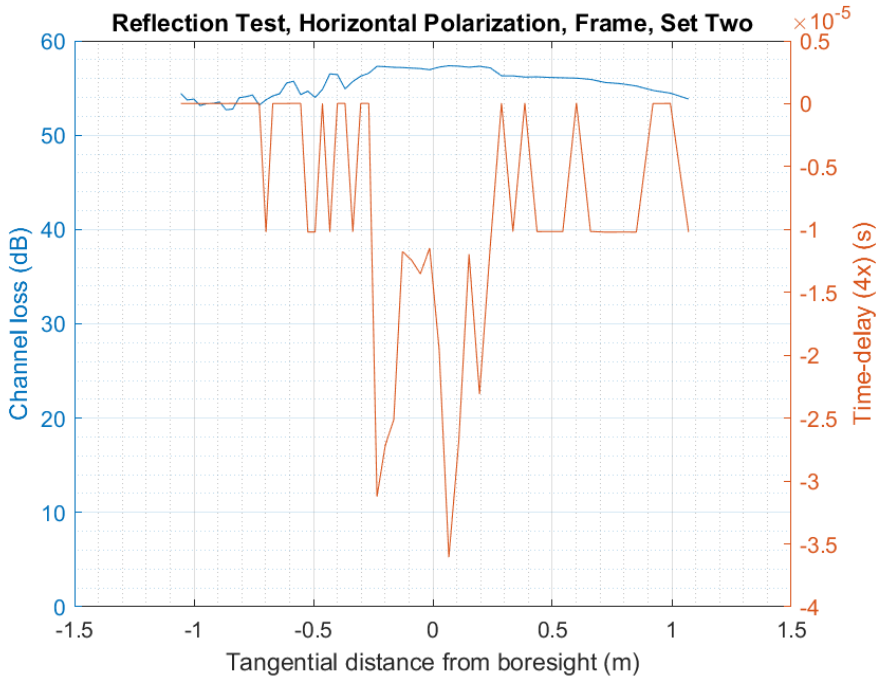

Figure 56: Reflection testing results using horizontal polarization with wooden frame, at a distance of 2.11 meters

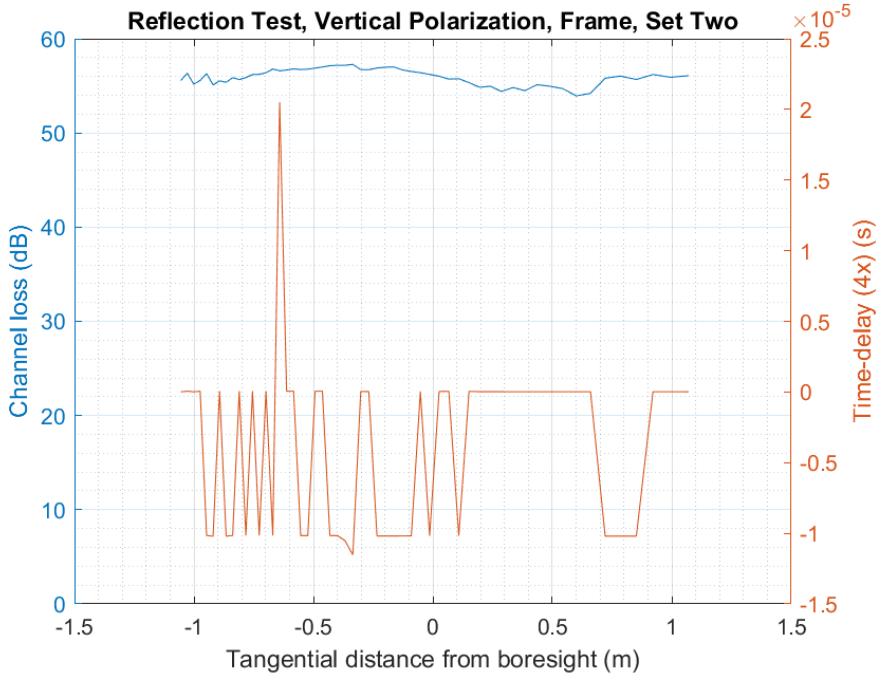

Figure 57: : Reflection testing results using vertical polarization with wooden frame, at a distance of 2.11 meters

For the baseline measurements, shown in Figure 56 and Figure 57, the time-delay measurement was very indecipherable. Again, this is due to the lack of reflecting surfaces in the room without the sheet of metal. This leads to higher power loss, and degradation of the time-delay measurements.

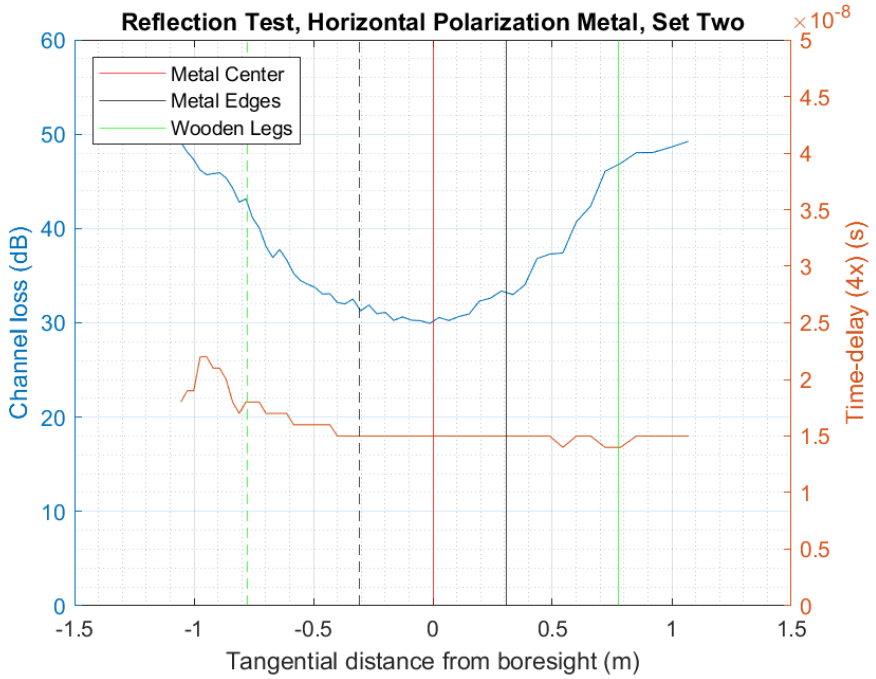

Figure 58: : Reflection testing results using horizontal polarization with a metal sheet, at a distance of 2.11 meters

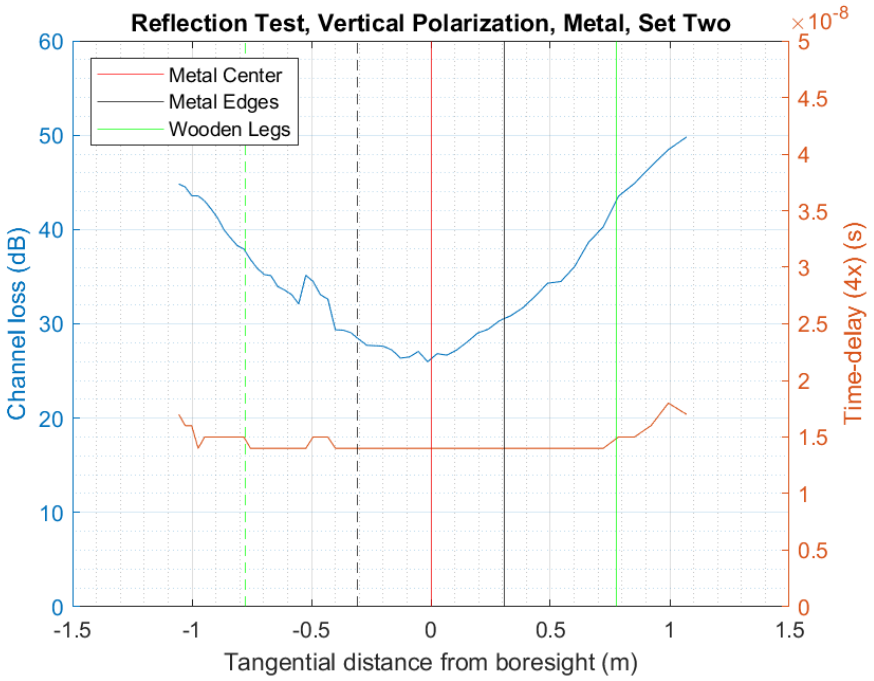

Figure 59: Reflection testing results using vertical polarization with a metal sheet, at a distance of 2.11 meters

At the farther distance, results from the second set differ from those previously. Both polarizations appear to be relatively constant, with a blip in the vertical measurements around -0.5 meters. This change in shape is due to the signal propagating farther in space, allowing the field to spread out over a greater distance and causing the vertical to no longer be completely reflected off of the sheet. The lack of oscillations likely due to this as well. With the field being more spread out, and the sheet taking up a smaller portion of the propagation channel, the received signal will be less sensitive to movements. The horizontal results can be seen in Figure 58 and the vertical in Figure 59.

4.2.5. Frame Cancellation (Reflection Testing, Second Set)

As with the first set, the baseline measurements were fairly flat in power, with some reflection at the center. For the difference between the two sets, both show oscillations

throughout, however the horizontal shows more numerous oscillations, while the vertical contains a large oscillation at -0.5 meters.

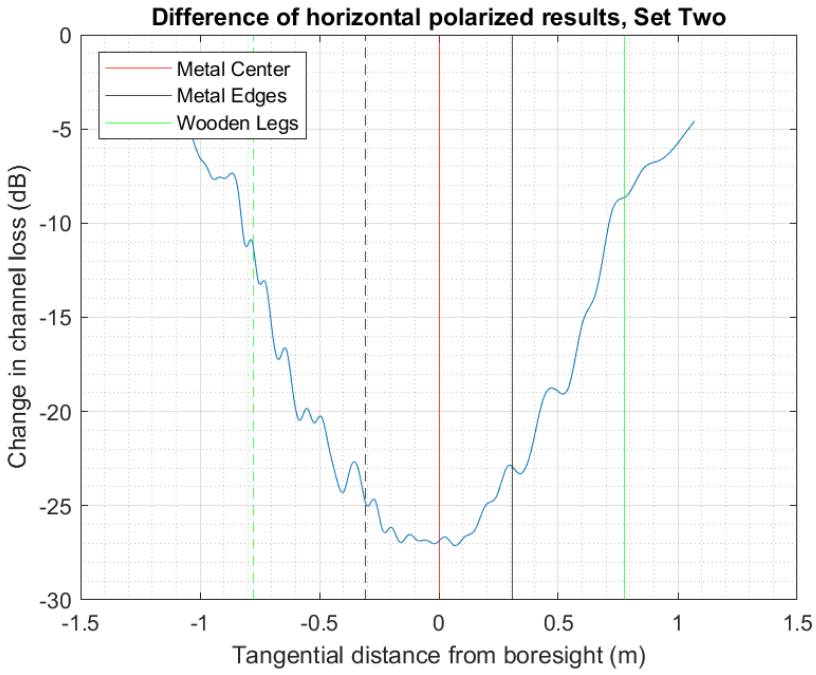

Figure 60: Difference of generated curves from reflection testing, horizontal polarization, S = 2.11 m

With the cancellation, the horizontal results (Figure 60) appear to regain their oscillations as with the measurements taken at the closer distance. These oscillations are a combination of the slight oscillations in both the baseline and the metal measurement, and appear to be random.

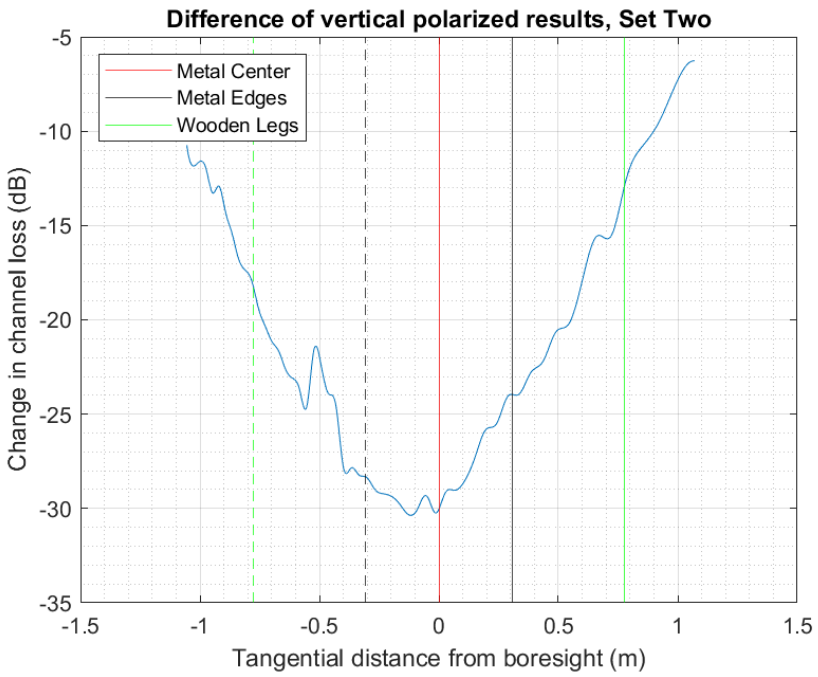

Figure 61: Difference of generated curves from reflection testing, vertical polarization, S = 2.11 m

With the results from Figure 61, the blip from the metal measurements has been somewhat emphasized, along with any oscillations present in both the baseline and the metal measurements. The oscillations as compared to the horizontal case, however, still are lower in amplitude. The vertical therefore is still being properly reflected, with low partial reflections.

4.2.6. Optimal Reflection

The final experiment was the optimal reflection test. The setup was very similar to the reflection test, with minor changes. First, the distance between antennas was set to double that of the distance from the sheet, and the azimuthal angle on both antennas was set to 45°. This allowed an optimal reflection angle of 90°from transmit to receive, should the sheet be present. Next, the sheet was moved from outside the propagation channel of the antennas, then through the channel, similar to the blocking test.

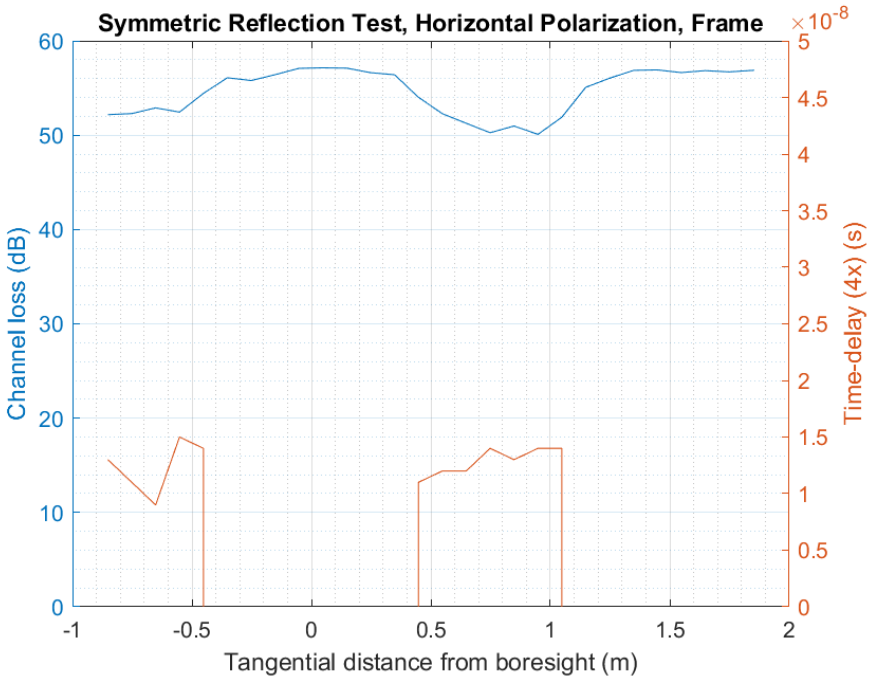

Figure 62: Reflection testing results using horizontal polarization with wooden frame

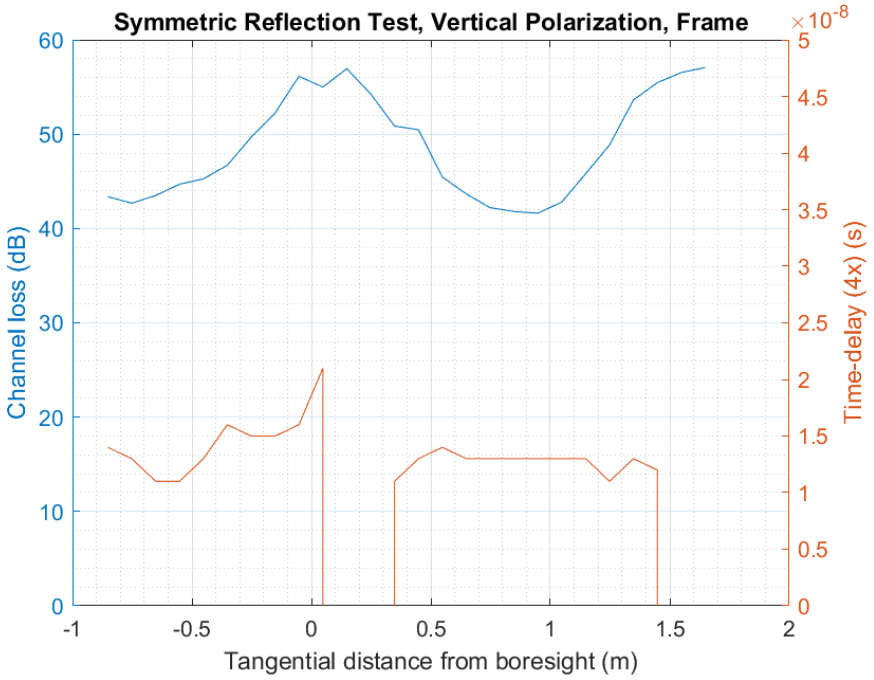

Figure 63: Reflection testing results using vertical polarization with wooden frame

For the baseline measurements with an optimal reflection, there is some deviation between the original reflection measurements already. In Figure 62, the horizontal baseline shows higher oscillations than the normal reflection experiment, most likely due to the ability of the system to better reflect the transmitted signal at the matched angle, while the time-delay remains rather uninformative. As for the vertical results in Figure 63, the oscillations are even larger. These results are somewhat expected, since the legs of the frame are oriented vertically, having a larger surface area for the vertically polarized signal to reflect off of.

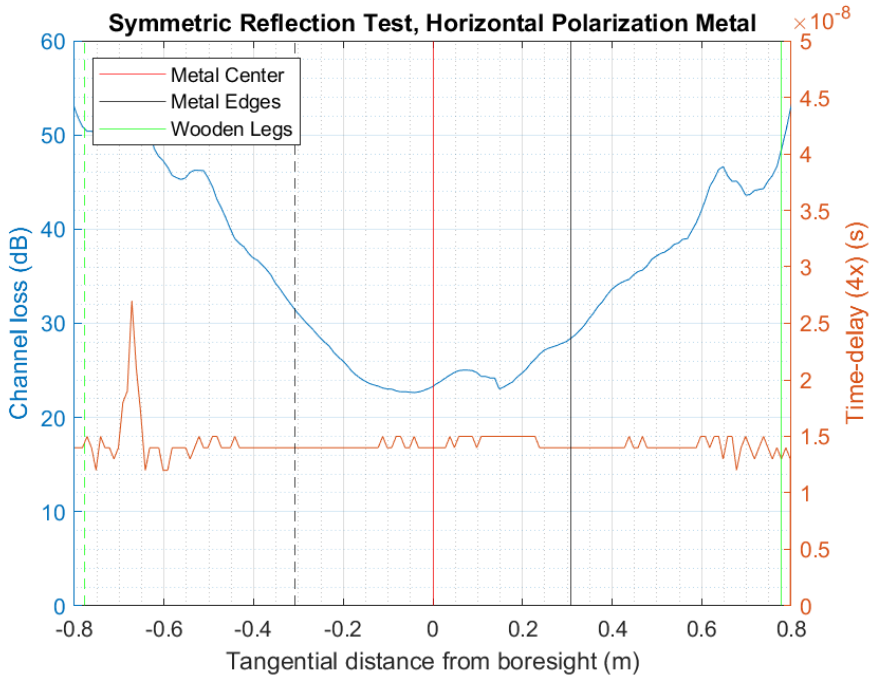

Figure 64: Reflection testing results using horizontal polarization with metal sheet

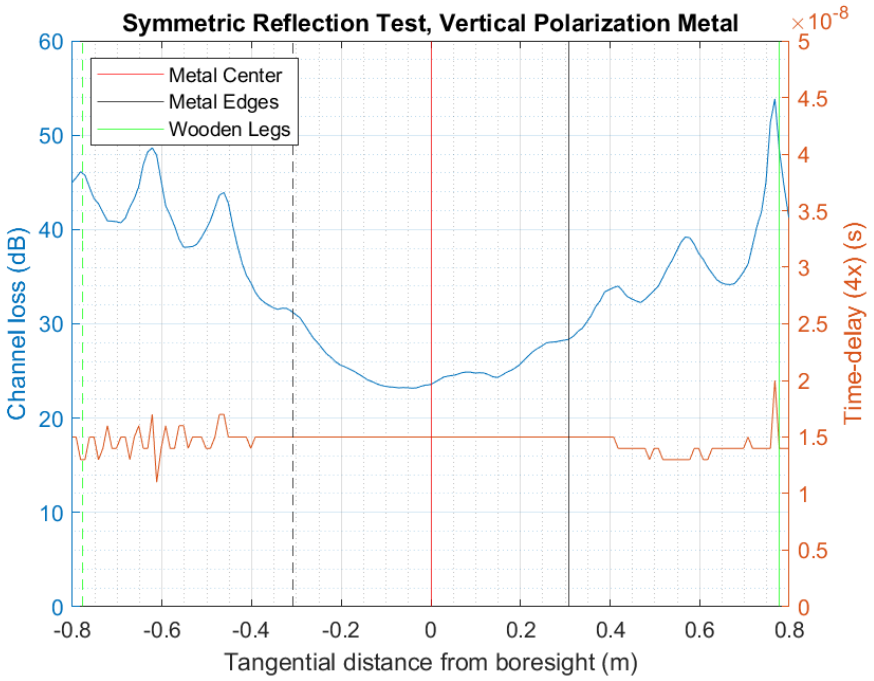

Figure 65: Reflection testing results using vertical polarization with metal sheet

When the metal is present for the optimal reflection, the results look similar to the original reflected test. In Figure 64, the horizontal results appear much more stable than their respective counterpart in the original test, while the vertical in Figure 65 contains much higher oscillations. This behavior is again caused by the geometry of the metal sheet. Any misalignments when moving the frame during the experiment would cause the vertical polarization to reflect wildly, while the horizontal will be resilient to misalignments of the plate.

4.2.7. Frame Cancellation (Optimal Reflection)

With respect to the initial reflection tests, there appears to be larger reflections off of the wooden legs, due to a more optimal reflection from them to the receiver. In this test, the vertical appears to be more sensitive to movement than the horizontal, repeating the pattern as shown in the blocking test. This may be due to the metal not being perfectly aligned at all times with the antennas while moving through the channel.

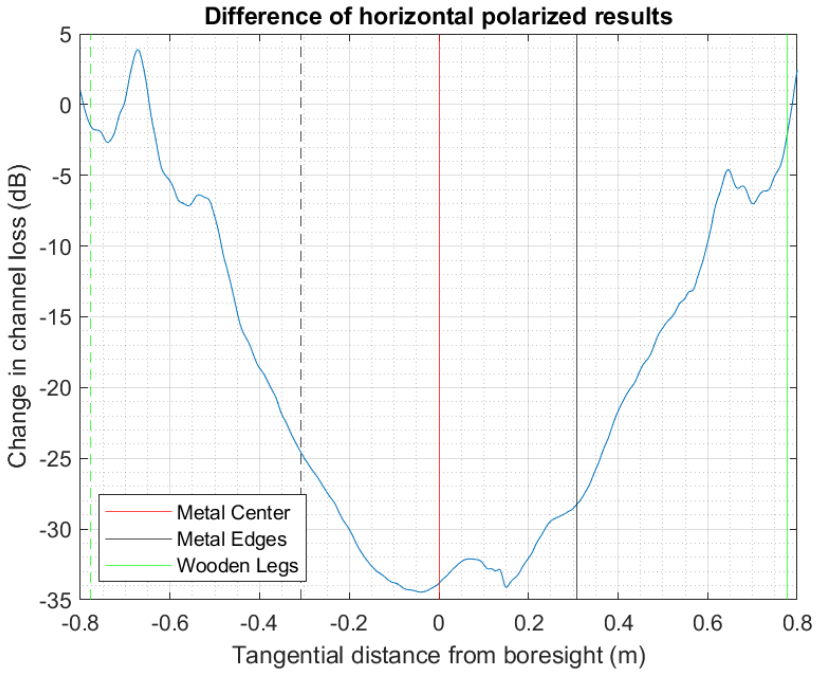

Figure 66: Difference of generated curves from reflection testing, horizontal polarization, S = 2.11 m

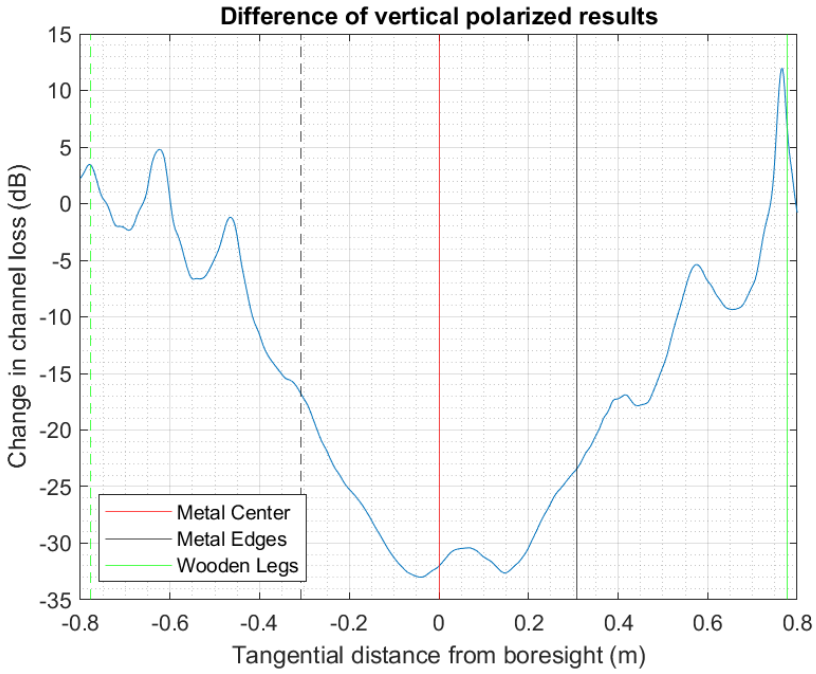

Figure 67: Difference of generated curves from reflection testing, vertical polarization, S = 2.11 m

5. Summary Analysis

5.1. Result Validation

To validate this work's results, the electric field of the signal will be observed. Using equations from Molisch on reflection [35] and on diffraction [36].

In this system, the overall losses can be broken down into three main factors: the free-space losses from transmitter to the reflecting object, the reflection off of said object, and the free space loss from the reflecting object to the receiver. The received power of a system in free-space can be described by [37]:

$$P_{RX}(d) = P_{TX} G_{TX} \frac{1}{4\pi d^2} A_{RX} \tag{20}$$

where P_{RX} is the received power, P_{TX} is the transmit power, G_{TX} is the antenna gain in the direction of the receive antenna, d is the propagation distance between the transmit and receive, and A_{RX} is the effective area of the receiver antenna. With this, the only non-constant value is the distance the signal in question is traveling, causing any losses caused by the sheet that aren't due to reflection and refraction to be linear with distance.

With respect to reflection, from Molisch, the reflection coefficient (ρ) for both TE and TM waves is -1 on an ideally conducting surface [35]. From this, when the entire signal is applied to the sheet, there will be minimal losses due to the actual reflection itself, as some energy will be absorbed by the aluminum sheet. However, until the angle of incidence is correct for propagating directly to the receive antenna, losses observed will be greater than the "perfect" angle for the reflection case, due to the directivity of the antennas used. As for the optimal reflection case, as the metal enters the propagation channel, more and more of the signal should be reflected to the receive. When comparing the two polarizations used, the vertical, in theory,

should be more sensitive around the metal edges than the horizontal, while the horizontal will have a steady increase and decrease throughout.

For the tests monitoring the refraction of the signal, the equation for the total electric field can be observed, along with its respective components.

$$E_{total} = e^{-jk_0x}\left(\frac{1}{2} - \frac{e^{-j\frac{\pi}{4}}}{\sqrt{2}}F(v_f)\right) \tag{21}$$

$$F(v_F) = \int_0^{v_F} e^{-j\pi\frac{t^2}{2}}\,dt \tag{22}$$

$$\theta_d = \tan^{-1}\left(\frac{h_s - h_{TX}}{d_{TX}}\right) + \tan^{-1}\left(\frac{h_s - h_{RX}}{d_{RX}}\right) \tag{23}$$

$$v_F = \theta_d\sqrt{\frac{2d_{TX}d_{RX}}{\lambda(d_{TX} - d_{RX})}} \tag{24}$$

Going from top to bottom, E_{total} is the total electric field, $F(v_F)$ is the Fresnel integral, θ_d is the diffraction angle, and v_F is the Fresnel parameter obtained from θ_d. These equations are approximate, neglecting the polarization of the incident field, but can be used to approximate the effect of the "screen" on the field [35]. Should the diffraction angle be zero degrees, the Fresnel integral also becomes zero, causing the total field to simplify down to:

$$E_{total} = e^{-jk_0x}\left(\frac{1}{2}\right) \tag{25}$$

In equation (25), the exponential term represents the incident field, with k_0 being the wavenumber of the signal, and *x* is the x-coordinate. Regarding the test setup, this term will remain a constant throughout. With the load at the receiver being a constant, when the electric field is converted to dB, the resultant is approximately a -6 dB difference, as the signal begins to

diffract at zero degrees. A plot of the total field strength vs. the diffraction angle can be seen in Figure 68.

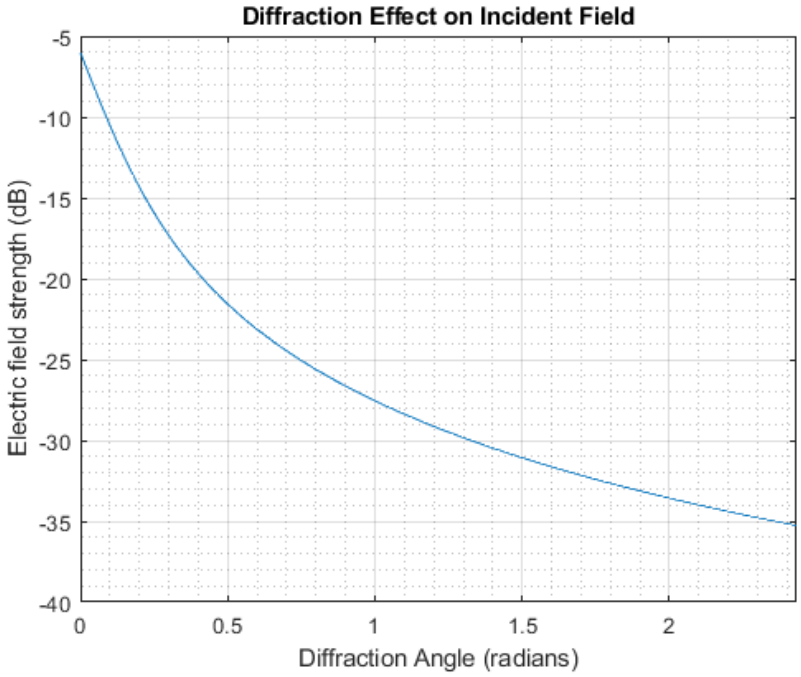

Figure 68: Simulated magnitude of the Fresnel integral term of equation (25) with respect to diffraction angle

As the diffraction angle increases, the field strength decreases at an exponential rate, similar to the overall shapes of the observed results. With the blocking test, a 6 dB difference at the edge was found between the baseline measurements and measurements with the metal present, matching with equation(25), seen in Figure 37 and Figure 39 at 0.3 meters. The same relationship can be seen in the azimuthal test results, seen in Figure 47and Figure 48 at 0.3 meters, and in the symmetric reflection results, seen in Figure 66 and Figure 67.

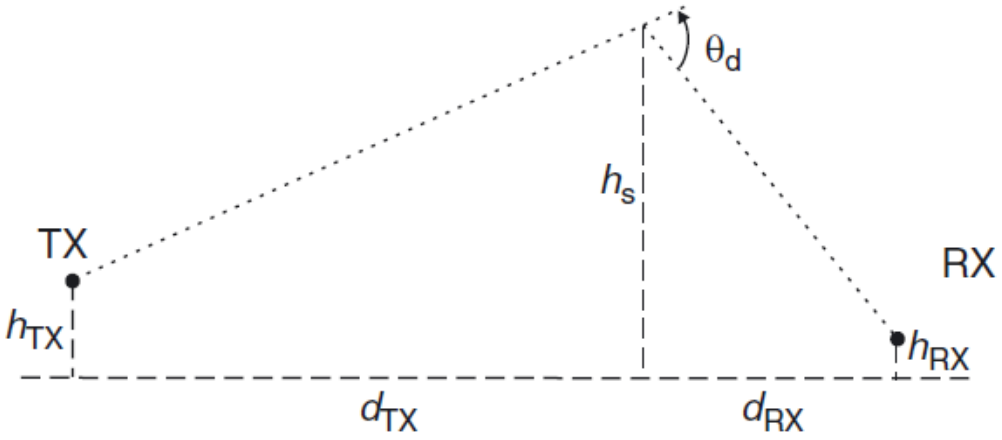

Figure 69: Diagram of the geometry described by equation (21), acquired from Molisch [35]

5.2. Resolution of System

To define the resolution for the system, the slopes of each response will be used. Each experiment resulted in a response with a bell curve-like shape. The slope on the left side, and the right side of the slope was observed, then depending on the sign of the slope, was divided by three or negative three, to negate any sign issues. The total results for each test can be seen below in Table V. To calculate the resolution, the slopes of the two linear sections of each difference curve were calculated. The slopes were then converted to dB per centimeter and plugged into equation (26), where the sign of the numerator matches the sign of the slope. This equation tells us how large of a distance change results in the loss of the system doubling, a large enough change in loss to discern past noise. Based on these results, the average resolution achieved was 5.27 cm.

$$\Delta = \frac{\pm 3\ dB}{slope} \tag{26}$$

Table V: Slopes and Resolutions of each Test

Test Name	Polarization	Left Hand Slope (dB/m)	Right Hand Slope (dB/m)	Left Hand Resolution (cm)	Right Hand Resolution (cm)	Average Resolution (cm)
Blocking Test	Horizontal	66.58	-49.73	4.51	6.03	5.27
	Vertical	78.14	-65.37	3.84	4.59	4.22
	45-Slant	91.37	-53.21	3.28	5.64	4.46
Azimuthal Sweep	Horizontal	120.37	-133.51	2.49	2.25	2.37
	Vertical	93.56	-81.69	3.21	3.67	6.88
Reflection (Set 1)	Horizontal	-71.80	68.76	4.18	4.36	4.27
	Vertical	-45.54	40.48	6.59	7.41	7.00
Reflection (Set 2)	Horizontal	-33.95	29.49	8.84	10.17	9.51
	Vertical	-87.25	62.18	3.44	4.82	4.13
Symmetric Reflection	Horizontal	-68.33	50.49	4.39	5.94	5.17
	Vertical	-63.26	62.92	4.74	4.77	4.76

6. Conclusions

Based on the data gathered, the proposed system using received channel power as the detection metric seems promising. To achieve smaller resolutions and resolve smaller distances, a larger carrier frequency would be necessary. As for a path-delay based approach, a system with a higher baseband sampling rate, or the ability to capture the raw upconverted signal is needed

6.1. Future Work

6.1.1. Machine-learning

To improve metal edge detection, one route could be a machine learning algorithm, to detect where the edge of the metal object is based on this data. This would most likely take the form of a semi-supervised model.

6.1.2. Different materials

Another route to explore would be using different types of metal for the same type of object to observe differences in behavior between them and aluminum. For example, iron or steel. As both of these materials are magnetic, one being an alloy of the other, the presence of

ferric objects could affect the propagation path, thus throwing off measurements. As the both are commonly used to cast parts, this would be an important property to observe.

6.1.3. System Improvements

Several improvements to the current system could be made to improve data collection and distance/angle precision. One such improvement would be the automation of distance measurement and object movement, which could be done via a feedback control system and stepper motors, controlled through MATLAB. Through this, the system resolution could be confirmed through much finer position steps and allow larger volume of data collection. The antennas azimuth position could also be automated, to allow more accurate azimuthal steps, and would allow the antennas to track the object as it moves through the propagation channel.

The step from one-dimensional measurements to two-dimensional would require additional antennas to the system, either electronically switched in or manually inserted. This would allow the system to measure the number of reflections produced by the object and allow multiple “angles of attack” to propagate the signal. As reflections increase from the baseline, this would indicate a presence of a metal object.

In terms of resolution, this would be improved via an increase in propagation frequency from the 5 GHz band. This would increase the propagation channels sensitivity to metal objects and require new equipment to propagate such a signal. To operate in the 20 GHz band easily, a carrier frequency of 24 GHz would most likely need to be used, as it is reserved for amateur radio from 24.0 GHz to 24.025 GHz, per FCC frequency allocation [38]. On top of this, a receiver with a larger base-band sampling rate will be necessary to detect the smaller sample delays.

As for the time-delay calculation, the cross-correlation used to calculate sample delay is very much dependent on the received channel power of the system. When the channel loss begins to be too great for the signal to propagate, the time-delay calculations fall apart, resulting in nonsensical data. To avoid this in the future, larger transmission powers will need to be used to overcome the resulting channel losses due to the metal object.

References

[1] M. Radivojevic, T. Tehren, E. Pernicka, D. Slijivar, M. Brauns and D. Boric, "On the origings of extractive metallurgy: new evidence from Europe," *Journal of Archaeological Science,* vol. 37, no. 11, pp. 2775-2787, 2010.

[2] ASM International, Casting Design and Performance, ASM International, 2009.

[3] United States Environmental Protection Agency, "Industrial Radiography," 14 July 2022. [Online]. Available: https://www.epa.gov/radtown/industrial-radiography#:~:text=People%20and%20businesses%20who%20want,of%20equipment%20and%20radiation%20sources.. [Accessed 24 October 2022].

[4] United States Nuclear Regulatroy Commission, "PART 34 - LICENSES FOR INDUSTRIAL RADIOGRAPHY AND RADIATION SAFETY REQUIREMENTS FOR INDUSTRIAL RAIDOGRAPHIC OPERATIONS," 30 November 2020. [Online]. Available: https://www.nrc.gov/reading-rm/doc-collections/cfr/part034/full-text.html#part034-0001. [Accessed 24 October 2022].

[5] R. R. Edelman, "The History of MR imaging as Seen through the Pages of Radiology," *Radiology,* vol. 273, pp. S181 - S200, 2014.

[6] Cleveland Clinic, "Magnetic Resonance Imaging (MRI)," 29 October 2019. [Online]. Available: https://my.clevelandclinic.org/health/diagnostics/4876-magnetic-resonance-imaging-mri.

[7] S. Currie, N. Hoggard, I. J. Craven, M. Hadjivassiliou and I. D. Wilkinson, "Understanding MRI: basic MR physics for physicians," *Postgraduate Medical Journal,* vol. 89, p. 209–223, 2013.

[8] Mayo Clinic, "MRI," 2021. [Online]. Available: https://www.mayoclinic.org/tests-procedures/mri/about/pac-20384768.

[9] European Space Agency, "MRI brain scan," 27 June 2019. [Online]. Available: http://www.esa.int/ESA_Multimedia/Images/2013/06/MRI_brain_scan.

[10] The American Society for Nondestructive Testing, "Introduction to Nondestructive Testing," 2021. [Online]. Available: https://asnt.org/MajorSiteSections/About/Introduction_to_Nondestructive_Testing.

[11] The Graduate Engineer, "What Is MPI (Magnetic Particle Inspection)," 2 November 2021. [Online]. Available: https://thegraduateengineer.com/what-is-mpi-magnetic-particle-inspection/. [Accessed 17 April 2022].

[12] Mayo Clinic, "Ultrasound," 2021. [Online]. Available: https://www.mayoclinic.org/tests-procedures/ultrasound/about/pac-20395177.

[13] National Institute of Biomedical Imaging and Bioengineering, "Ultrasound," [Online]. Available: https://www.nibib.nih.gov/science-education/science-topics/ultrasound.

[14] Orlando Heart & Vascular Institute, "Diagnostic Ultrasound Testing," 2021. [Online]. Available: https://www.mayoclinic.org/tests-procedures/mri/about/pac-20384768.

[15] D. Halliday, R. Resnick and J. Walker, Funamentals of Physics (Volume 2), Wiley, 1996.

[16] B. Fell, "Basic Radar Concepts: An Introduction To Radar For Optical Engineers," in *Effective Utilization of Optics in Radar Systems*, 1977.

[17] J. D. Gibson, The Mobile Communications Handbook, Boca Ration, Florida: CRS Press, 1999.

[18] R. L. Jesch, "DIELECTRIC MEASUREMENTS OF FIVE DIFFERENT SOIL TEXTURAL TYPES AS FUNCTIONS OF FREQUENCY AND MOISTURE CONTENT," National Bureau of Standards, Boulder, CO, 1978.

[19] P. Cote, "DOWNHOLE RF COMMUNICATION CHARACTERIZATION AND MODELING OF WAVEGUIDE PROPAGATION IN A FLUID-FILLED DRILL PIPE," 2019.

[20] C. Matzler and A. Murk, "Complex dielectric constant of dry sand in the 0.1 to 2 GHz range," 2010.

[21] J. Wang, "The dielectric properties of soil-water mixtures at microwave frequencies," *Radio Science*, vol. 15, no. 5, pp. 977 - 985, 1980.

[22] J. M. Walker, A. Prokop, C. Lynagh, B. Vuksanovich, B. Conner, K. Rogers, J. Thiel and E. MacDonald, "Real-time process monitoring of core shifts during metal casting with wireless sensing and 3D sand printing," *Additive Manufacturing*, vol. 27, pp. 54-60, 2019.

[23] D. Fitting, W. P. Dube and T. A. Siewert, "High Energy X-Ray Diffraction Technique for Monitoring Solidification of Single Crystal Castings," 1 June 1998.

[Online]. Available: https://www.nist.gov/publications/high-energy-x-ray-diffraction-technique-monitoring-solidification-single-crystal. [Accessed 22 July 2022].

[24] H. Bendjama, K. Gherfi, D. Idiou and J. Bast, "Condition Monitoring of Casting Process using Multivariate Statistical Method," in *ADVCOMP*, Rome, 2014.

[25] B. Wei, A. Varshney, N. Patwari, W. Hu, T. Voigt and C. C.T, "dRTI: Directional Radio Tomographic Imaging," *IPSN '15: Proceedings of the 14th International Conference on Information Processing in Sensor Networks*, pp. 166-177, 2015.

[26] S. L. H. Xu, F. Gao and Z. Wang, "Compressive Sensing Based Radio Tomographic," *Sensors*, vol. 19, no. 3, p. 439, 2019.

[27] Tkgd2007, "Coaxial cable," [Online]. Available: https://en.wikipedia.org/wiki/Coaxial_cable#/media/File:Coaxial_cable_cutaway.svg.

[28] D. M. Pozar, Microwave Engineering, Hoboken, NJ: John Wiley & Sons, 2012.

[29] SuperManu, "Electromagnetic radiation," [Online]. Available: https://en.wikipedia.org/wiki/Electromagnetic_radiation#/media/File:Onde_electromagnetique.svg.

[30] A. Barrantes, "Fresnel Zone Calculator," Omni Calculator, 6 April 2022. [Online]. Available: https://www.omnicalculator.com/physics/fresnel-zone. [Accessed 14 June 2022].

[31] J. Golio and M. Golio, The RF and microwave handbook, 2nd ed., CRC Press, Taylor and Francis Group, 2008.

[32] Federal Communications Commission, *FCC 03-287*, Washington D.C., 2003.

[33] KP Performance Anetnnas, "KP-5HA-60 Product Data Sheet," Inifinite Electronics Inc., 2020. [Online]. Available: https://www.kpperformance.com/Content/Images/Downloadables/Datasheets/KP-5HA-60_datasheets_US.pdf. [Accessed 17 January 2022].

[34] KP Performance Antennas, "KP-5HA-30 Product Data Sheet," Infinite Electronics Inc., 2020. [Online]. Available: https://www.kpperformance.com/Content/Images/Downloadables/Datasheets/KP-5HA-30_datasheets_US.pdf. [Accessed 17 January 2022].

[35] A. F. Molisch, "Reflection and Transmission," in *Wireless Communications,* Los Angeles , John Wiley and Sons, Ltd, 2010, pp. 49-53.

[36] A. F. Molisch, "Diffraction," in *Wireless Communications*, Los Angeles, John Wiley and Sons, Ltd, 2010, pp. 54-55.

[37] A. F. Molisch, "Free Space Attenuation," in *Wireless Communication*, Los Angeles, John Wiley And Sons Ltd., 2010, pp. 47-48.

[38] National Telecommunications and Information Administration, "U.S. Frequency Allocatoin Chart," October 2003. [Online]. Available: https://www.ntia.doc.gov/files/ntia/publications/2003-allochrt.pdf. [Accessed 5 October 2022].

[39] R. A. Pooley, "Fundamental Physics of MR Imaging," *RadioGraphics,* vol. 25, pp. 1087-1099, 2005.

[40] C. Balanis, Advanced Engineering Electromagnetics, John Wiley & Sons, 1989.

Appendix A: S-parameter plots with air as the dielectric

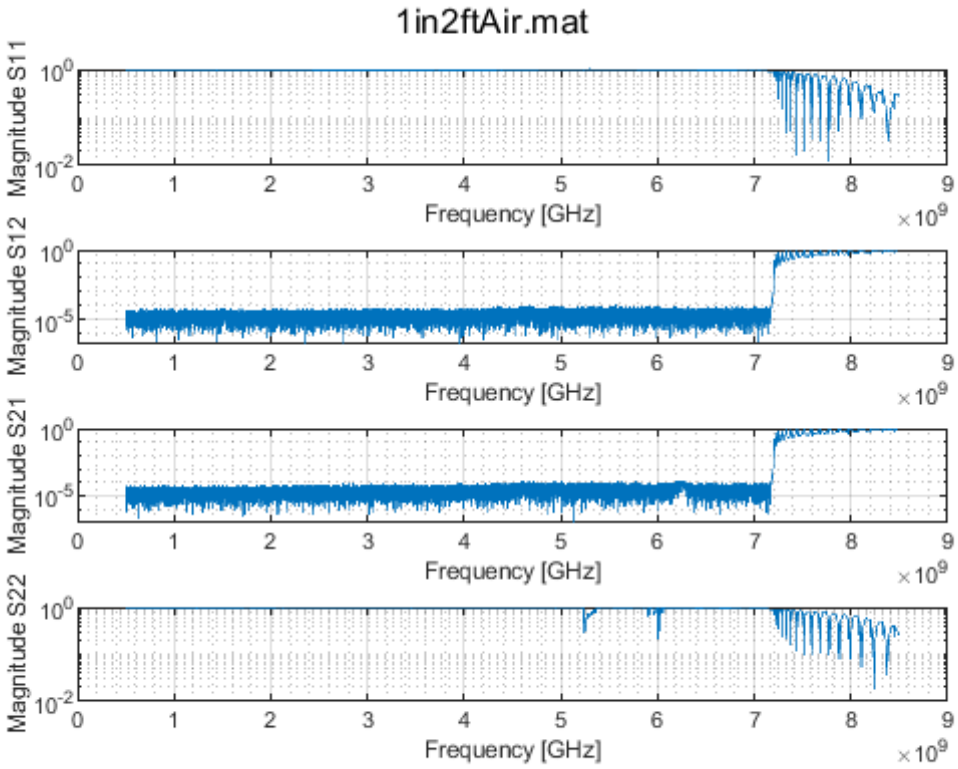

Figure 70: S-parameters results from one-inch inner diameter waveguide at two foot length

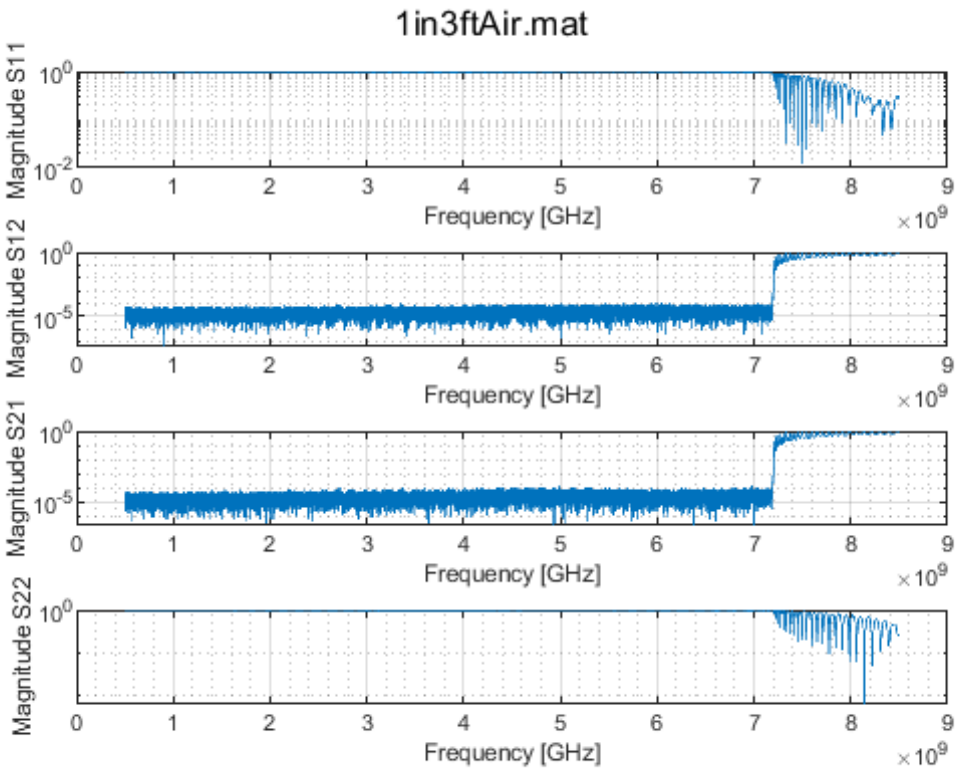

Figure 71: S-parameter results from one-inch inner diameter waveguide at three foot length

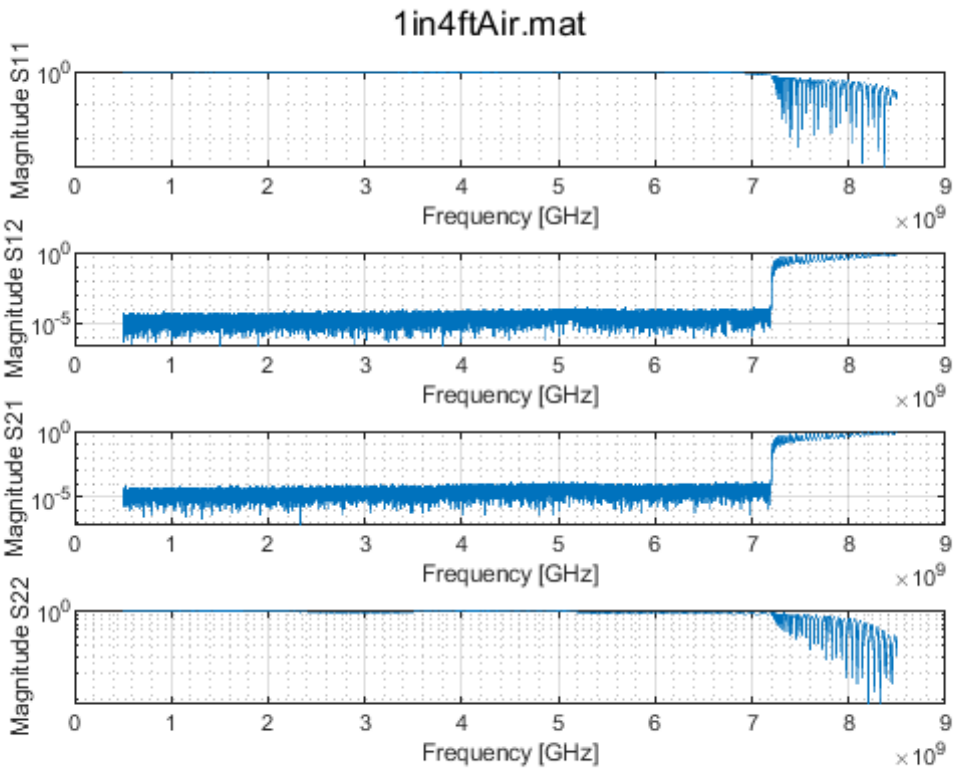

Figure 72: S-parameter results from one-inch inner diameter waveguide at four foot length

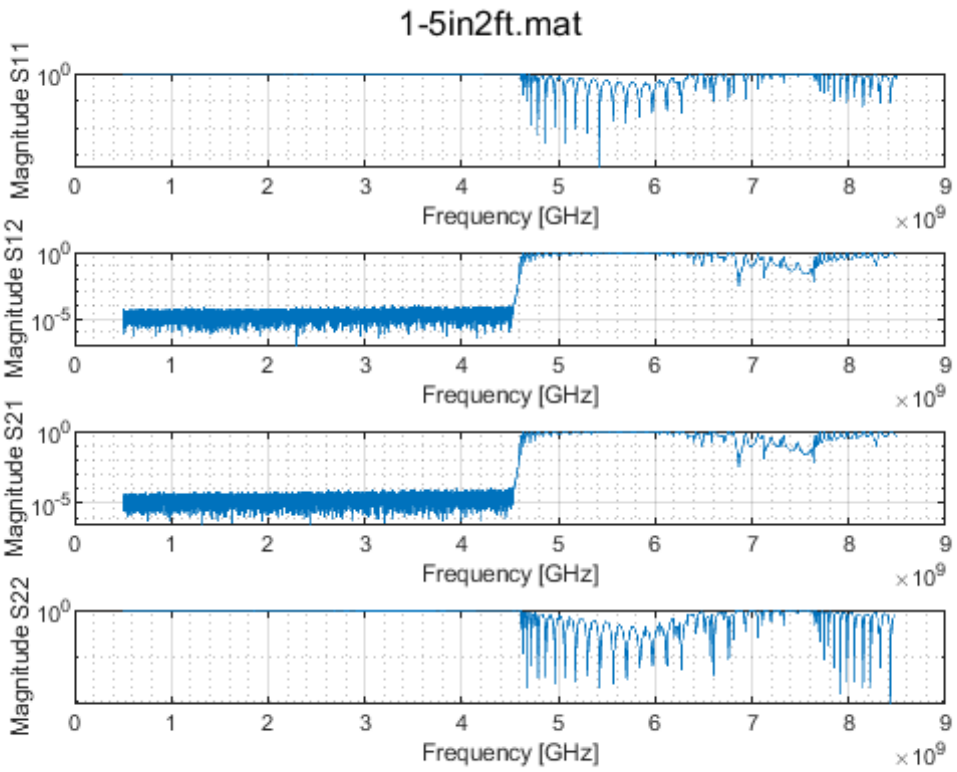

Figure 73: S-parameter results from 1.5-inch inner diameter waveguide at two-foot length

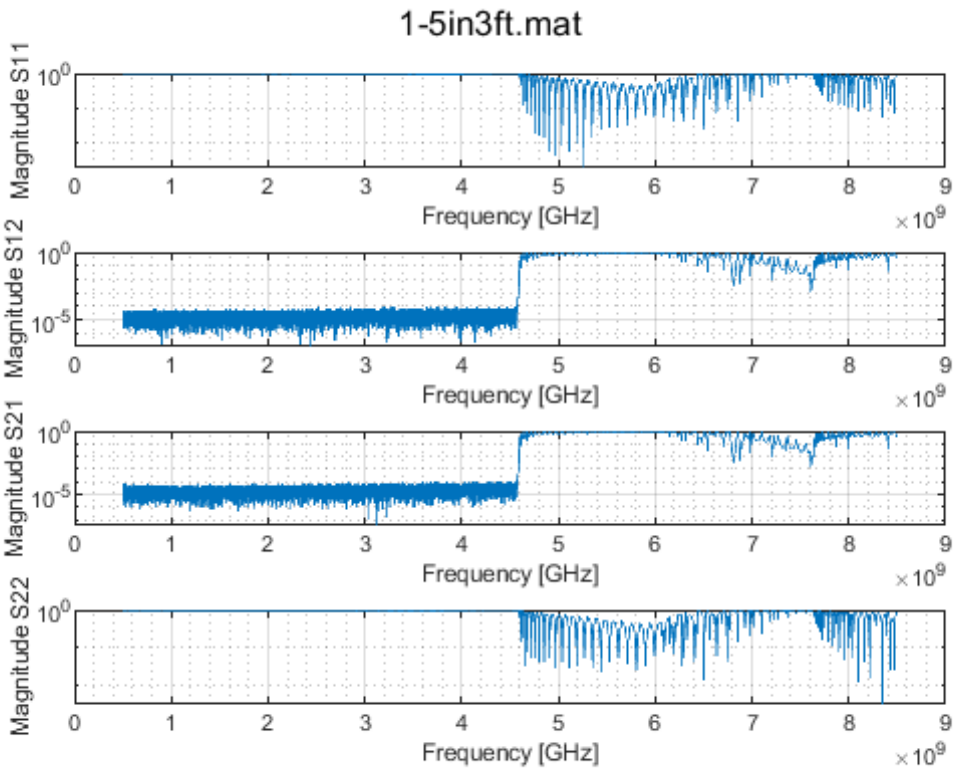

Figure 74: S-parameter results from 1.5-inch inner diameter waveguide at three-foot length

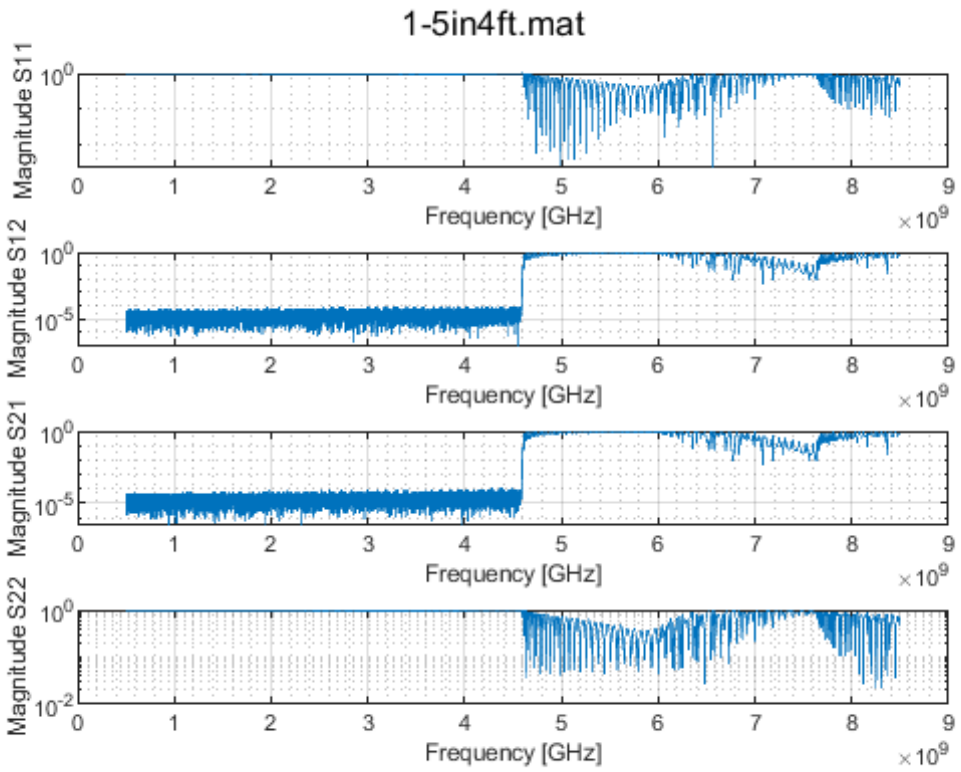

Figure 75: S-parameter results from 1.5-inch inner diameter waveguide at four-foot length

Appendix B: S-parameter plots with cast sand as the dielectric

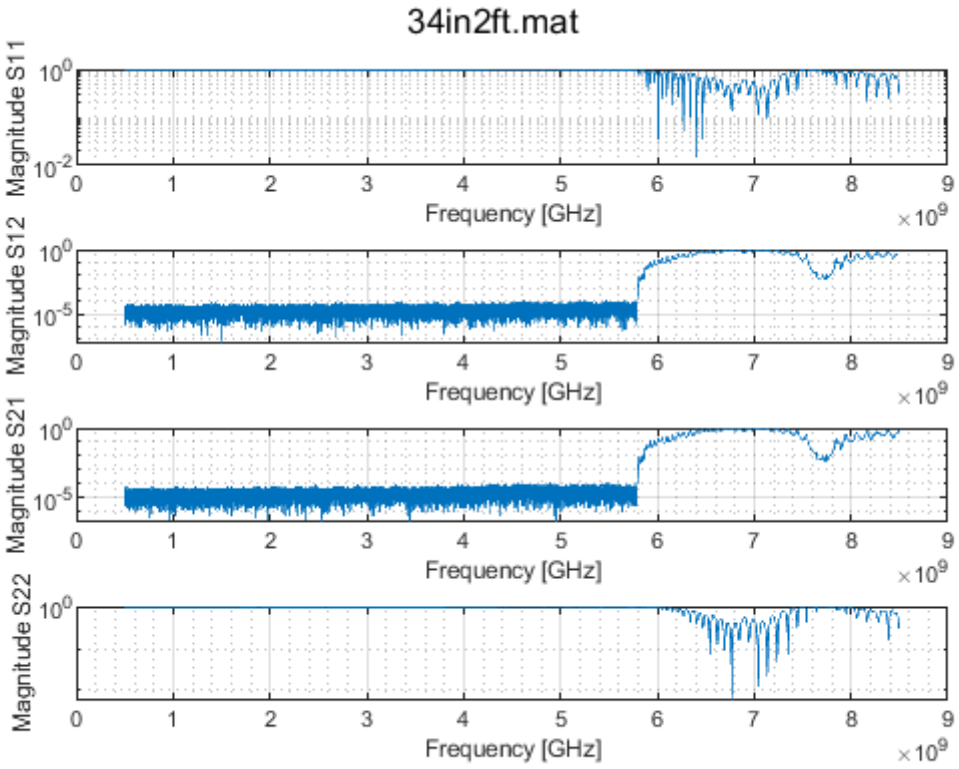

Figure 76: S-parameter results from 0.75-inch inner diameter waveguide at two-foot length

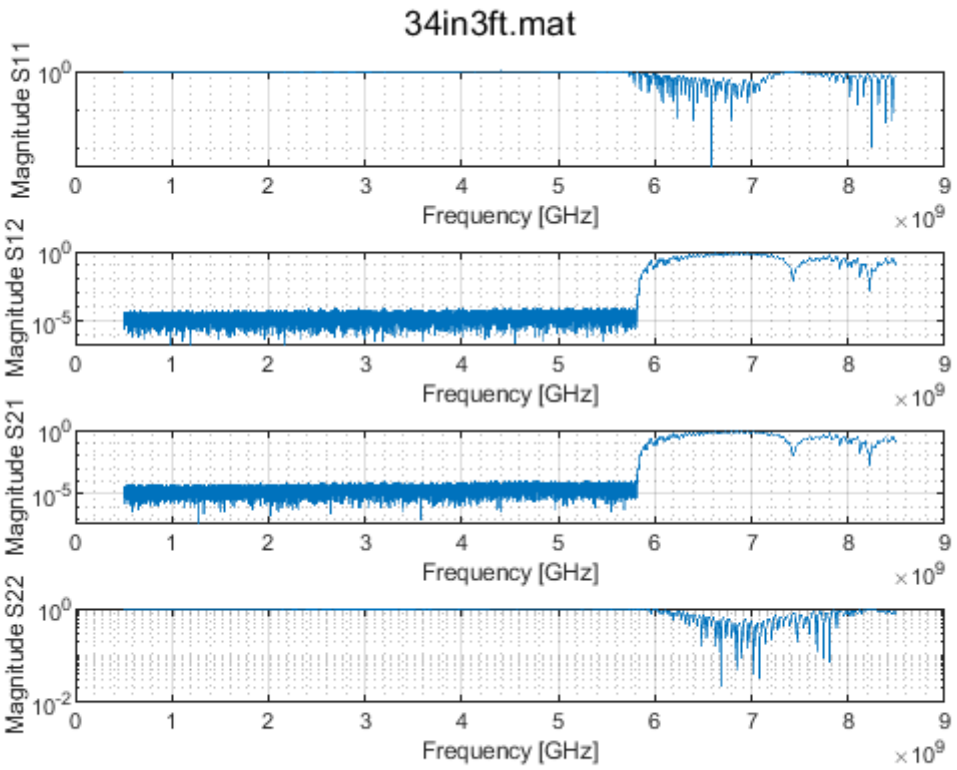

Figure 77: S-parameter results from 0.75-inch inner diameter waveguide at three-foot length

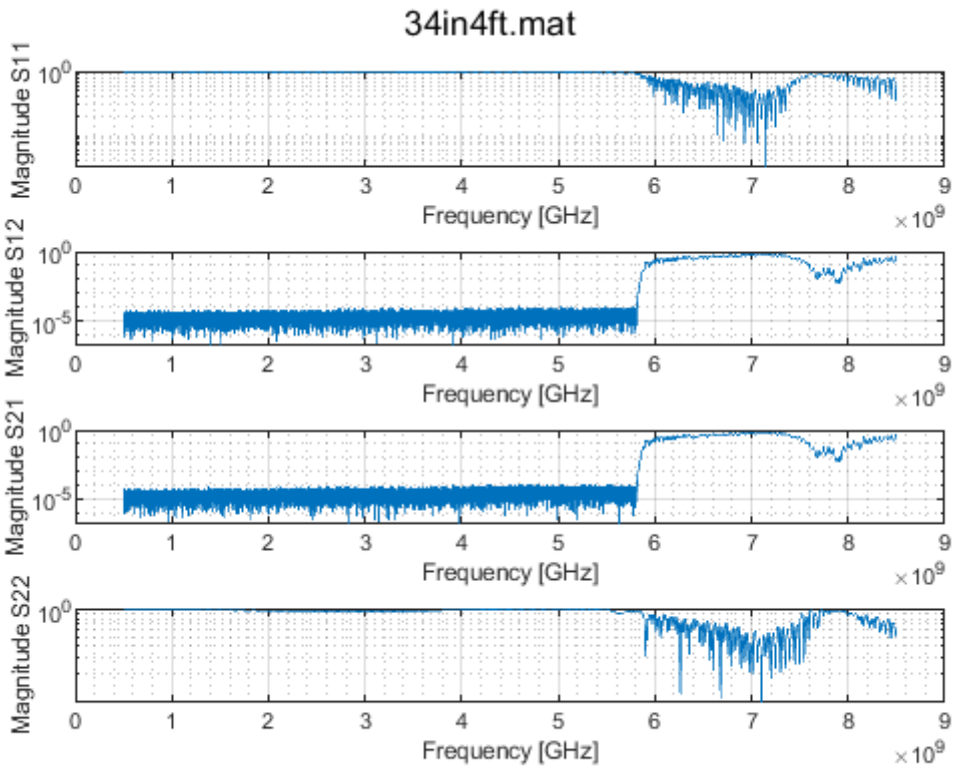

Figure 78: S-parameter results from 0.75-inch inner diameter waveguide at four-foot length

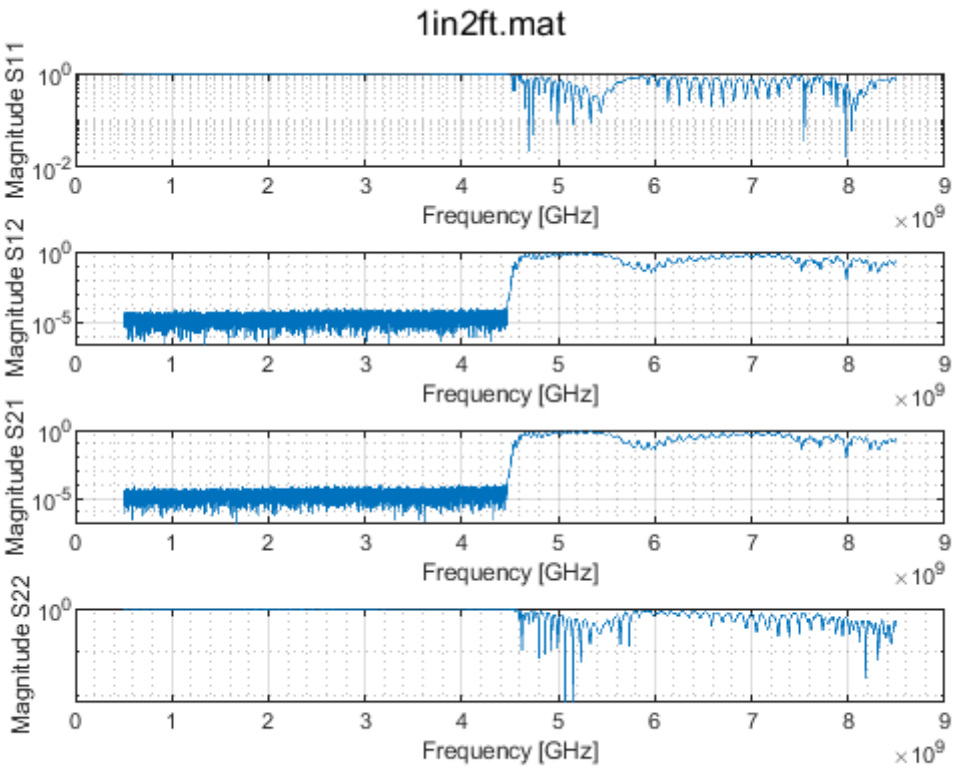

Figure 79: S-parameter results from one-inch inner diameter waveguide at two-foot length

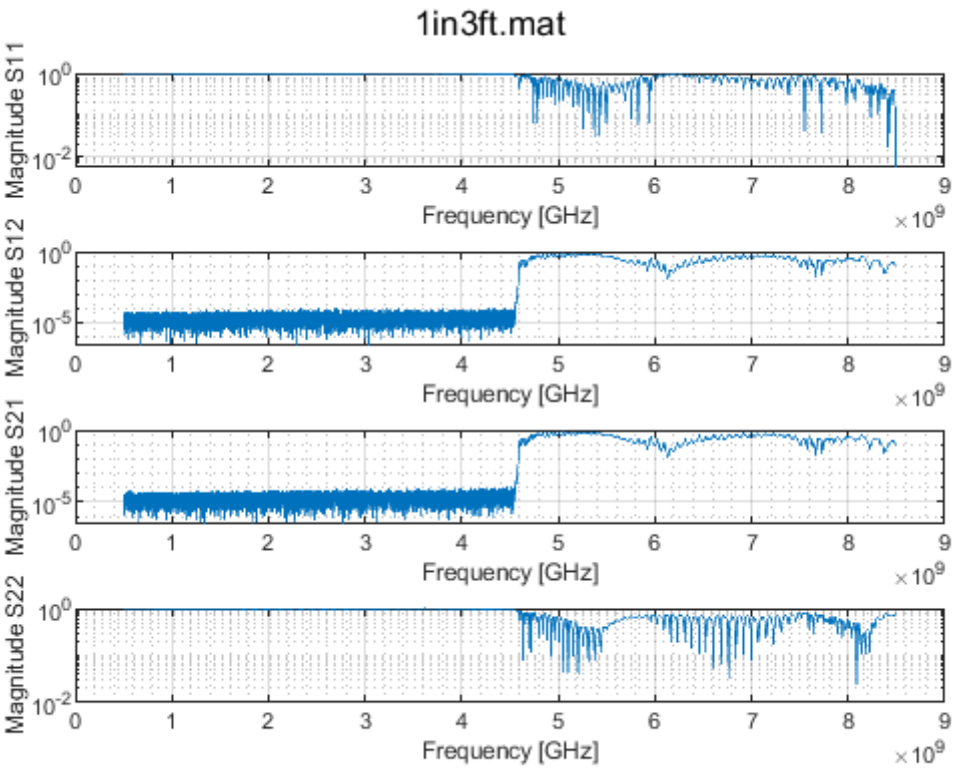

Figure 80: S-parameter results from one-inch inner diameter waveguide at three-foot length

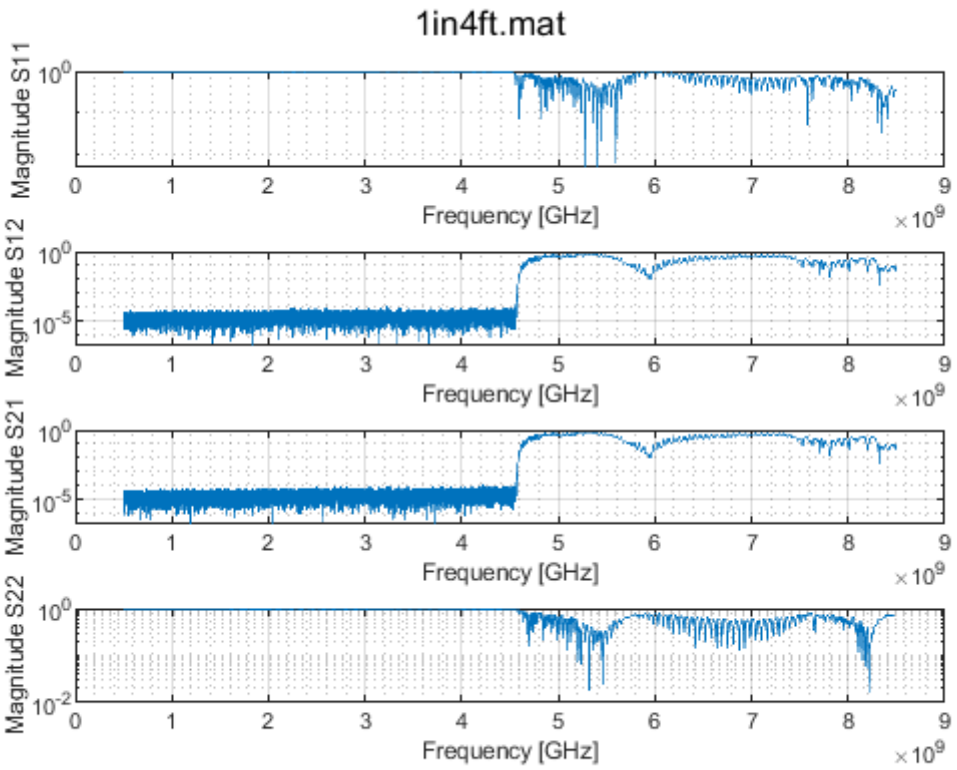

Figure 81: S-parameter results from one-inch inner diameter waveguide at four-foot length

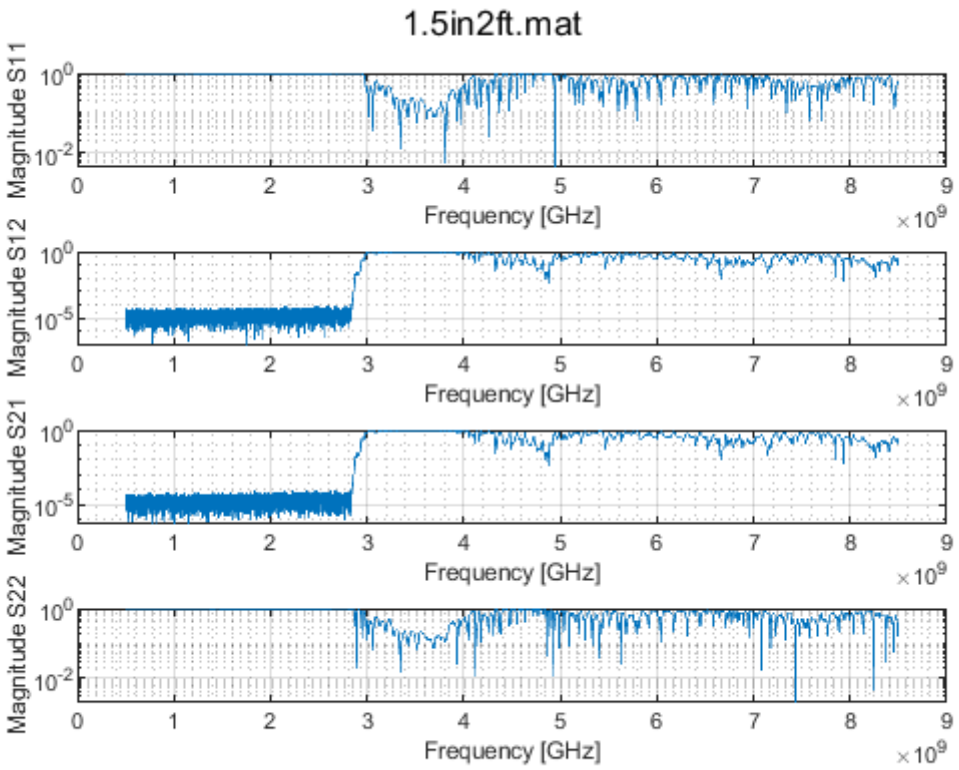

Figure 82: S-parameter results from 1.5-inch inner diameter waveguide at two-foot length

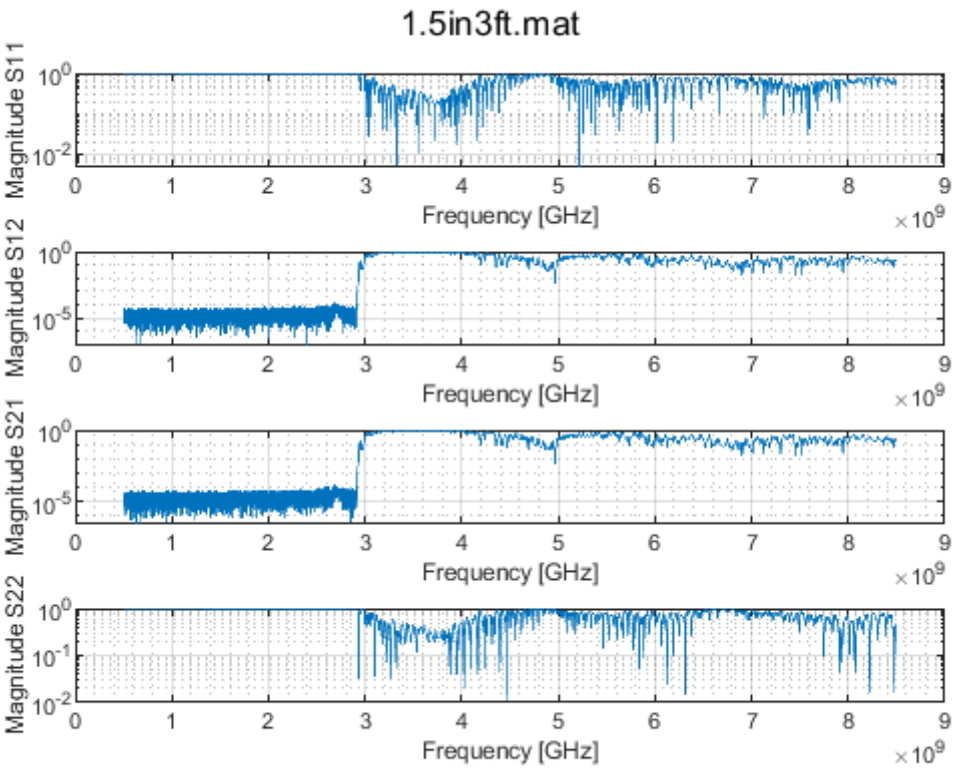

Figure 83: S-parameter results from 1.5-inch inner diameter waveguide at three-foot length

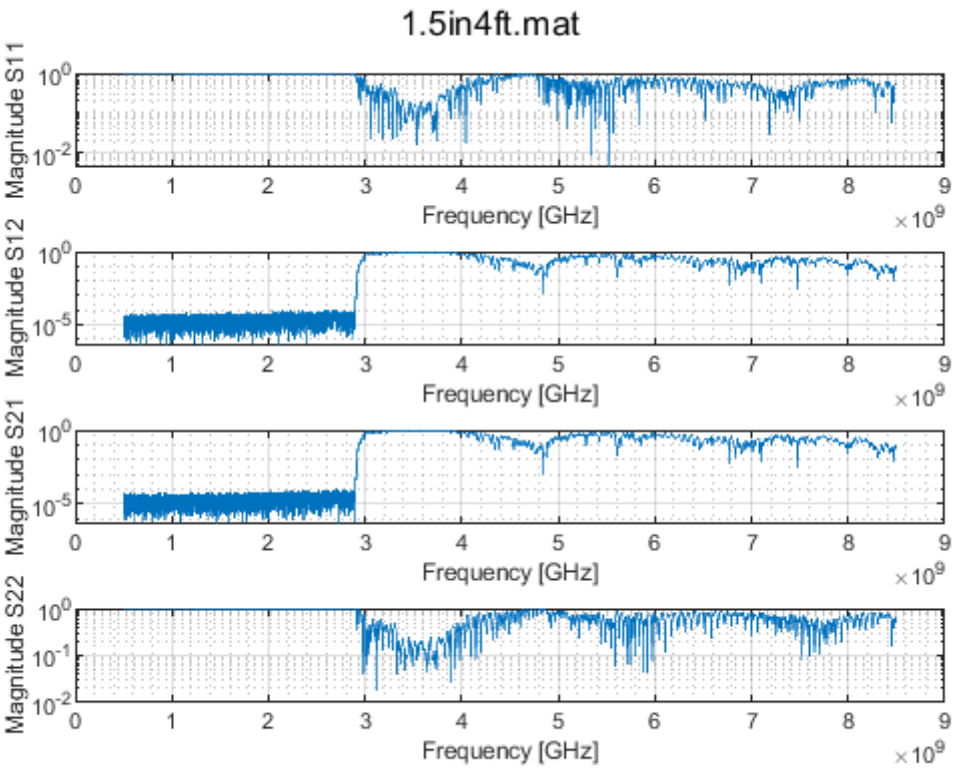

Figure 84: S-parameter results from 1.5-inch inner diameter waveguide at four-foot length

Appendix C: Generated Curves for Blocking Test

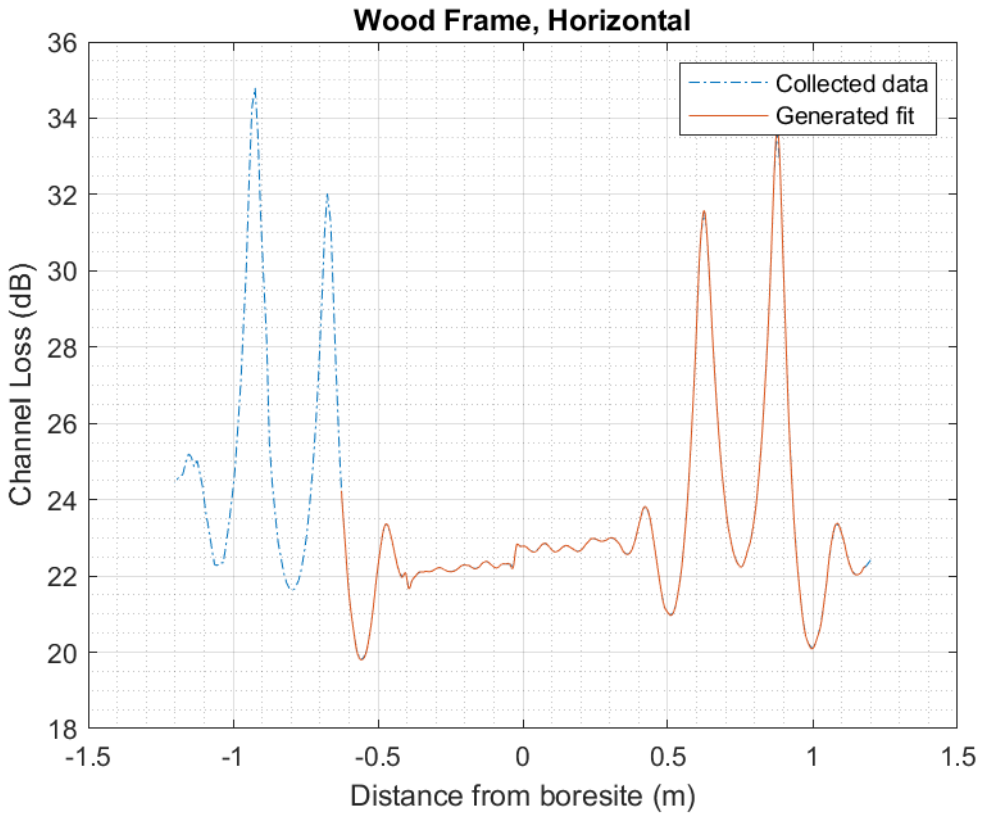

Figure 85: Collected data and best fit curve for wood frame, horizontal polarization

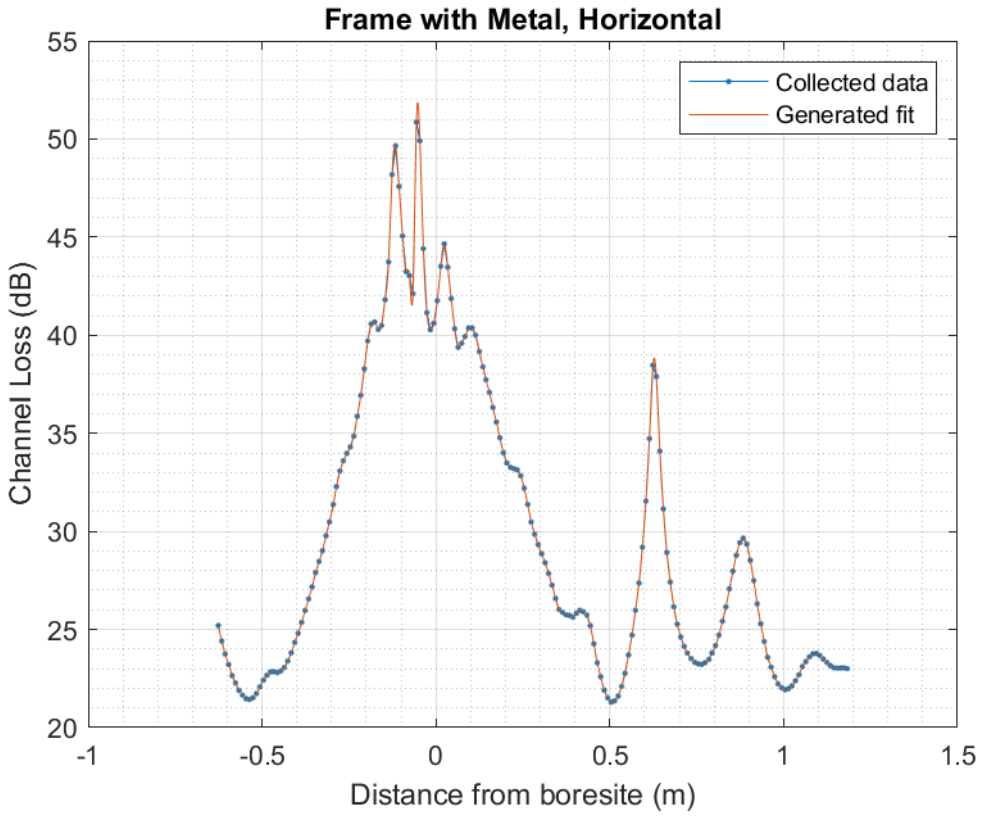

Figure 86: Collected data and best fit curve for frame with metal, horizontal polarization

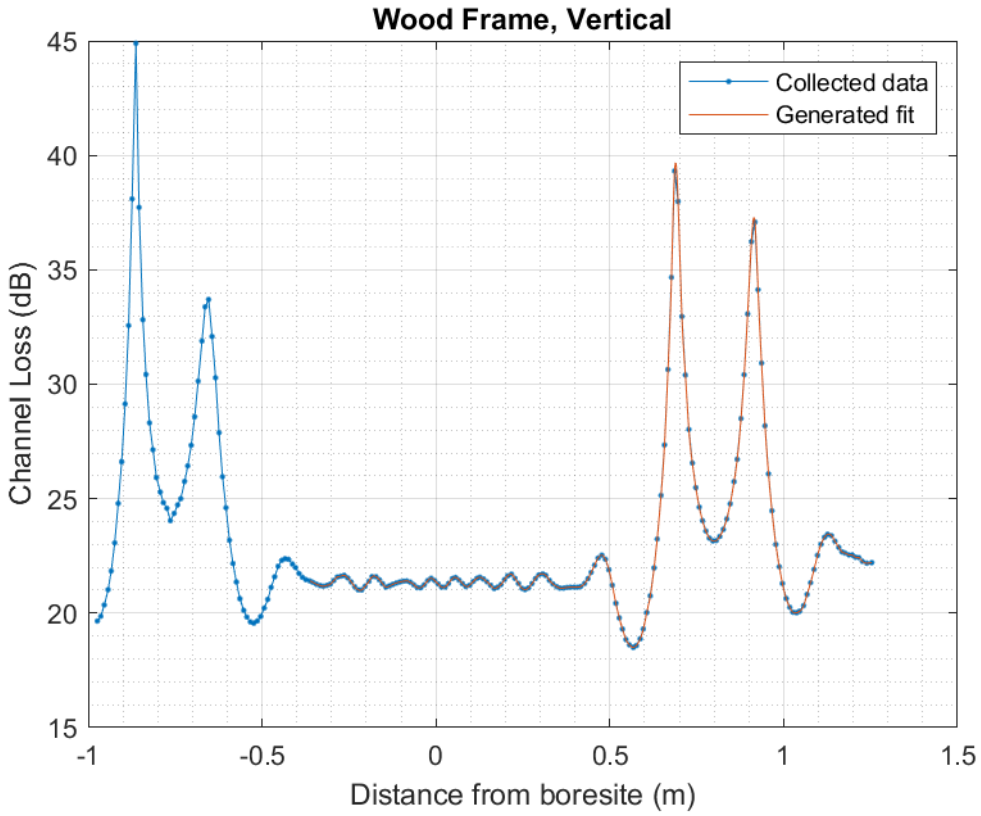

Figure 87: Collected data and best fit curve for wood frame, vertical polarization

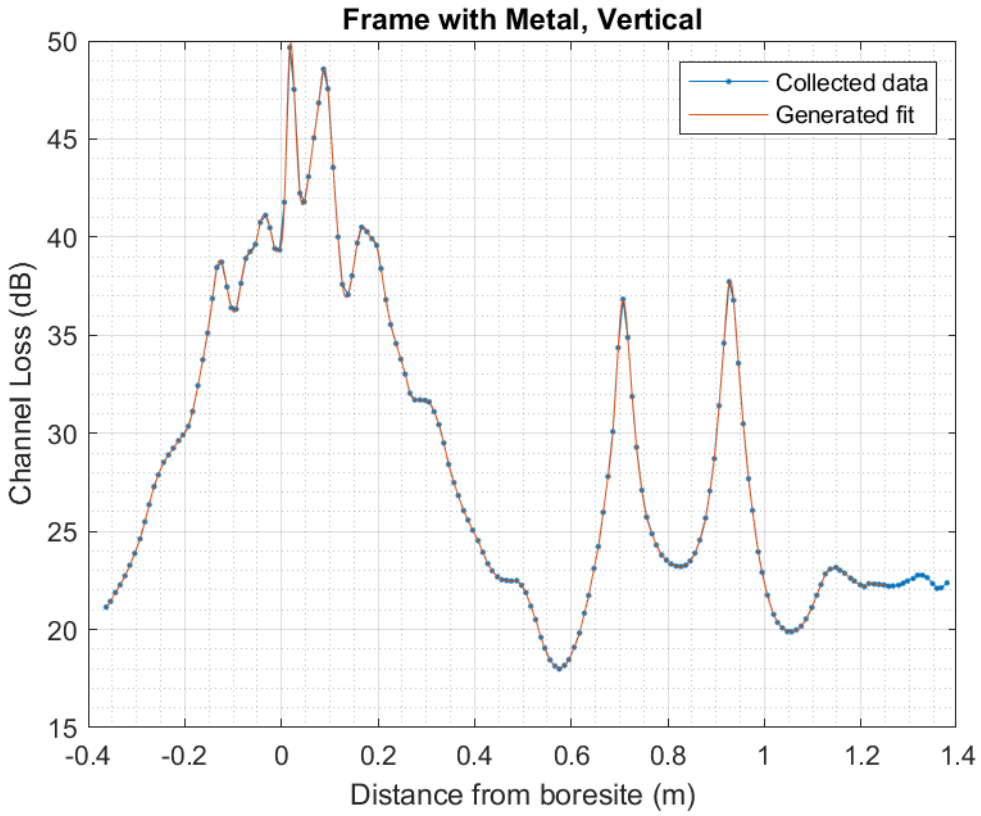

Figure 88: Collected data and best fit curve for wood frame, vertical polarization

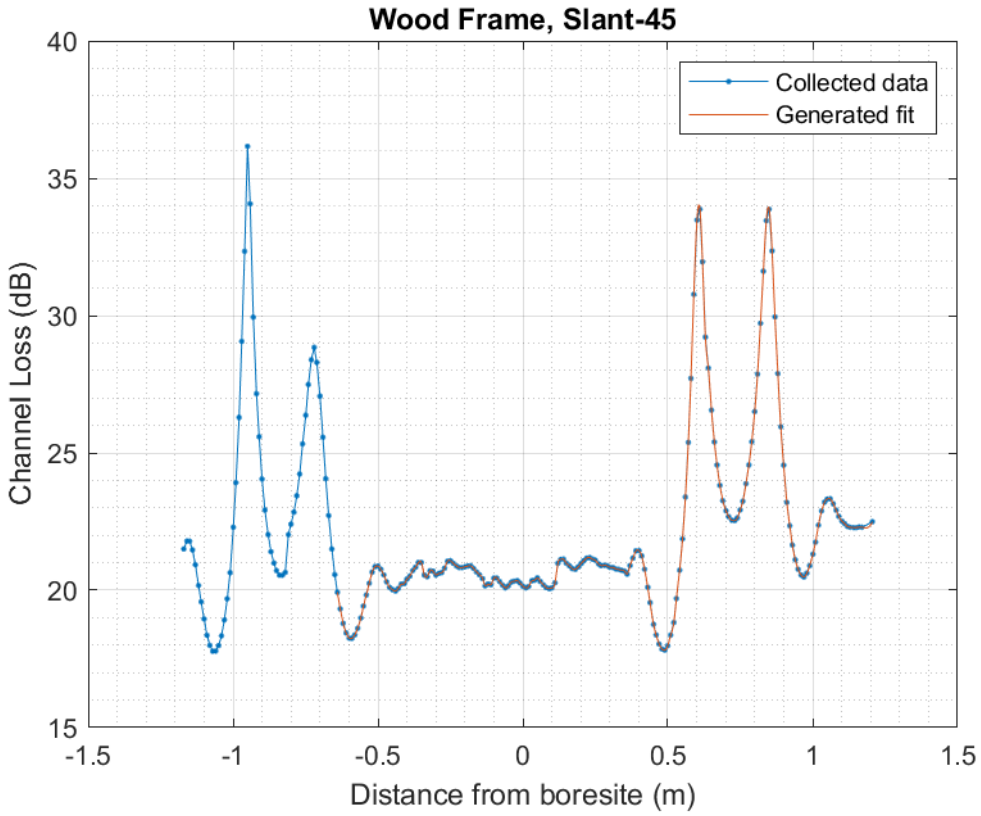

Figure 89: Collected data and best fit curve for wood frame, vertical polarization

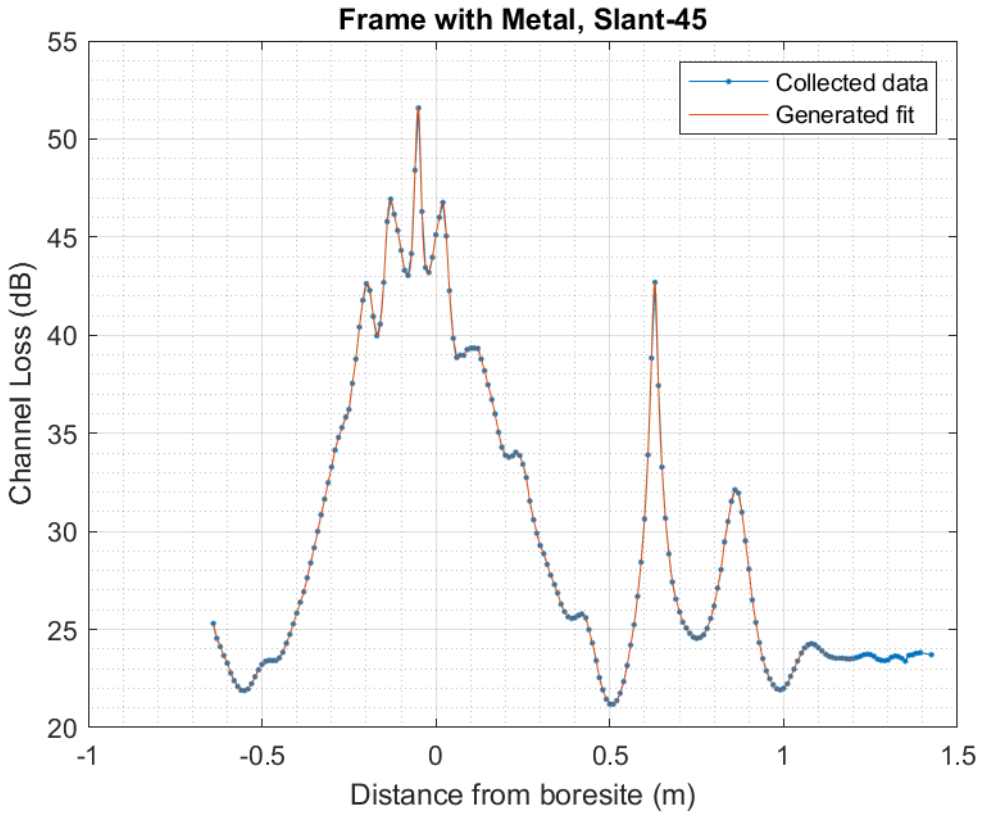

Figure 90: Collected data and best fit curve for wood frame, vertical polarization

Appendix D: Collected Azimuthal Testing Data at 1.558 m

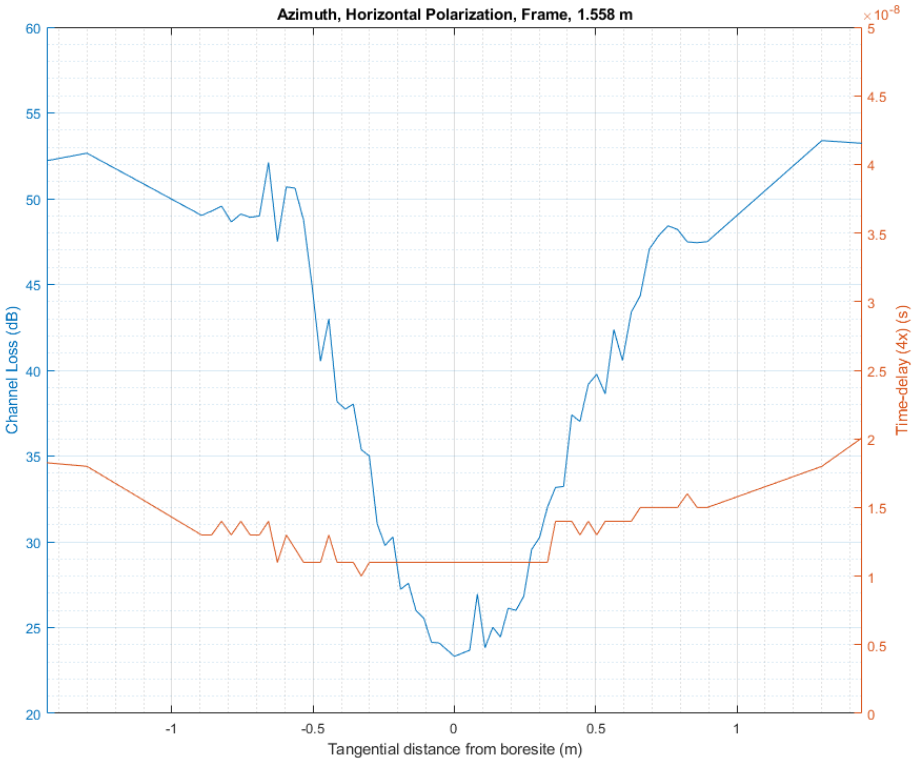

Figure 91: Collected data for wood frame at long distance, horizontal polarization, azimuthal testing

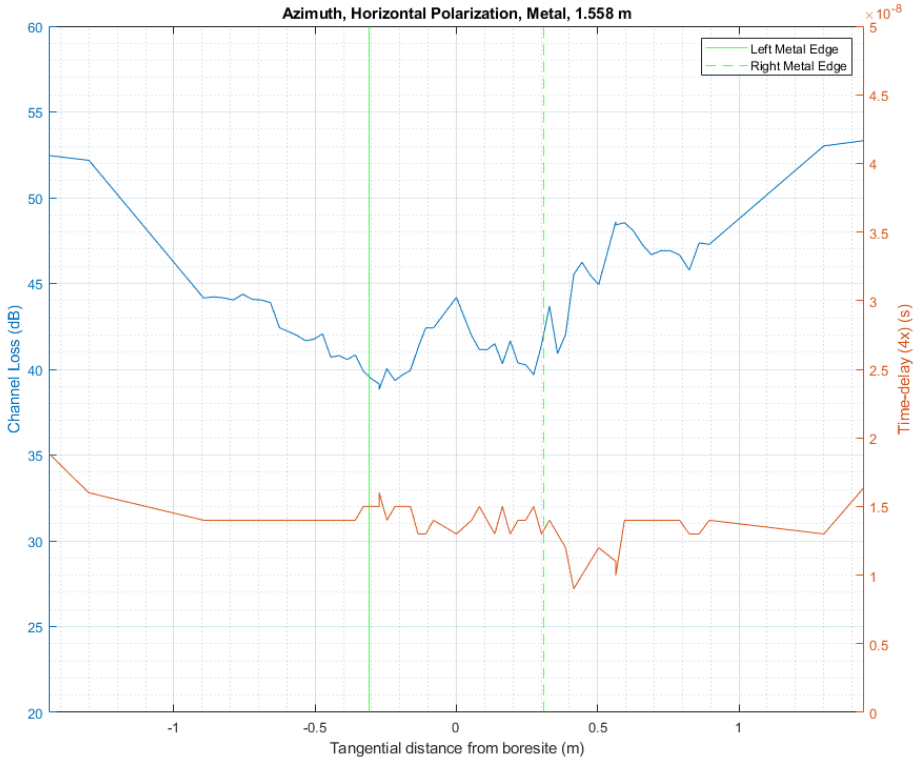

Figure 92: Collected data for metal at long distance, horizontal polarization, azimuthal testing

Appendix E: MATLAB Code

Main File

```
%% PathLengthSCPI_v2_1.m
% Controls instruments via SCPI and generates waveform for multi-path
% measurements, see documentation for further information
%
% Jamison Ehlers
% Masters of Science, Electrical Engineering
% Summer 2022

resp = input("Would you like to clear the workspace before proceeding? [Y/N]
",'s');
%% Housekeeping
if strcmp(resp,"Y") || strcmp(resp,"y")
    clc
    clear all
    close all
else
    clear resp
end
addpath('functions')
%% Test Parameters
test.sweepTime = 1e-3;                  % length of sample time, need to code
into SM200B class
test.recParam.plotFlg = zeros(1,5);     % flags for plotting data (need to
search for which flag is which)
test.shiftCollect = [0,0,0,0];          % initalize shiftCollect vector for
later tracking of sample delay, NOT CAL VECTOR
test.recParam.transmitRate = 50e6;      % transmit rate of samples in VSG in
MHz
test.recParam.receiveRate = 250e6;      % receive rate of samples in SM200B
in Hz
test.corrThresh = .9;                   % Cross-correleation threshold for
sample delay calculations
test.intPow = [2,4,8,16];               % interpolation factors to be used in
sample-delay calculations
test.pol = 'V_M';                       % polarization of antenna in use
test.ant = 'Reflection';                % type of test to be performed
antenna_separation = 2.1145;              % antenna separation distance,
meters, used in reflection testing TEST1: 1.22 m
distance_metal = 1.544;                 % aproximate antenna distance from
object, meters TEST1: 0.833 m
%% Calibration and run parameters
cal.samples = 100;                      % number of samples to use for
calibration
run.samples = 10;                       % number of samples to take for each
data point
contFlg = 1;                            % contFlg for operationality
%% Initialize equipment
vsg = VSG60A('127.0.0.1',5026,5.55e9,-20);
vsg.init();
sm = SM200B('127.0.0.2',5024,5.55e9,-20);
sm.init();
%% Generate waveform
```

```
% type of signal to transmit
% 0 for pN sequence
% 1 for constant 1 across all subcarriers
% 2 for impulse
% 3 for tone
sig.type = 0;                % signal type
sig.bitLength = 9;           % length of m-sequence to use
sig.file = 1;                % write the transmit signal samples to a file
sig.zPad = 100;              % number of zpad samples to use
sig.concat = 3;              % concatenate m-sequence 2^sig.concat times
sig.filt.b = .25;            % shape factor of rasied-cosine filter
sig.filt.span = 100;         % length of raised-cosine filter
sig.filt.sps = 2;            % BPSK modulation
sig.filt.shape = 'normal';  % shape of raised cosine filter, see "rcosdesign"
function in MATLAB for information
% Generate signal samples
[IQtx,timeSig,freqSig,h] = wfGen3(sig); % generate samplesy

%% Convert samples to transmit to ASCII
sampleStr = strings;
for k = 1:length(IQtx)
    if k < length(IQtx)
        sampleStr = sampleStr + num2str(IQtx(k,1)) + "," + num2str(IQtx(k,2))
+ ",";
    elseif k == length(IQtx)
        sampleStr = sampleStr + num2str(IQtx(k,1)) + "," +
num2str(IQtx(k,2));
    end
end

calFlg = 0; % Set calFlg to 0 until otherwise changed
%% BEGIN MAIN LOOP
while contFlg > 0
%% Calibrate system
    if contFlg > 1
        calStr = input('Would you like to calibrate the system? ',"s");
        if strcmp(calStr,'n') || strcmp(calStr,'N')
            calFlg = 0;
        else
            calFlg = 1;
        end
    end
    % If calibration is indicated, or this is the first measurement,
    % calibrate
    if or(calFlg,contFlg == 1)
        vsg.power = -20;            % Need to set vsg.power to actually set
power, additional writeline is probably redundant
        writeline(vsg.tcp,'POW -20')

        % Create loading bar for calibration
        input('Calibration commencing, please connect the VSG to the SA');
        calBar = waitbar(0,'Beginning calibration');
        % Run calibration and update calibration loading bar over time
        for k = 1:1:cal.samples
            waitbar(k/cal.samples,calBar,"Calibrating " + num2str(k) + "/" +
num2str(cal.samples));
```

```
            [refVec(k,:),test,pRef_samples(:,k),rcal(:,k),lagscal(:,k)] =
sysCal(vsg,sm,IQtx,test);
        end
        % Average power measurements after calibration is complete
        pRef = mean(pRef_samples);

        % Catch for number of calibration samples
        if cal.samples > 1
            refVec = round(mean(refVec));
        else
            refVec = round(refVec);
        end

        delete(calBar); % delete calBar to cleanup workspace and display
        disp(refVec); % display baseline delay
    end
%% Run Measurements
    beep % audio plays when calibration is complete
    if contFlg > 1
        fprintf("LAST DISTANCE: %.3f\n",distance(contFlg - 1));
    end
    distance(contFlg,:) = input("Please enter distance measured: "); %
collects change in distances for experiment
%     polarization(contFlg,:) = input("Please enter polarization config [H/V]
",'s'); % uncomment if different polarizations are begin explored in the same
experiment
    polarization(contFlg,:) = test.pol;
%     antenna(contFlg,:) = input("Please enter antennae in use [30/60] "); %
uncomment if different antennas are in use for the same experiment
    antenna(contFlg,:) = test.ant;
%     txPwr = input("Please enter requested transmit power [dB]: "); %
uncomment if different transmit powers are needed
    txPwr = 0; % comment out if variable transmit powers are needed
    if strcmp(test.ant,'Reflection')

        phi =
reflection_angle(distance(contFlg,:),distance_metal,antenna_separation);
        dispform = "Please set receive antenna to %.2f degrees\n";
        fprintf(dispform,phi)
    end
    vsg.power = txPwr;

    input('Initiate test sequence, please connect instruments to SUI, press
enter when finished')
    disp('System Start')
    testBar = waitbar(0,'Performing measurements'); % create loading bar for
measurements
    for n = 1:1:run.samples
        % update loading bar
        waitbar(n/run.samples,testBar,"Performing path-length measurements "
+ num2str(n) + "/" + num2str(run.samples));
        % initalize sample shift vector
        shiftCollect = zeros(1,4);
        IQrx = SCPIMeasure(vsg,sm,IQtx);
% make a sample measurement
        corrIdx = 1;
```

```
        for interpIdx = 1:1:length(test.intPow)
% iterate through inerpolations
            test.recParam.interpFactRx = 2^interpIdx;
% Calculate current interpolation factor
            test.recParam.interpFactTx =
[test.recParam.receiveRate/test.recParam.transmitRate,test.recParam.interpFac
tRx]; % calculate interpolation factor for transmit
            test.recParam.window =
601*test.recParam.interpFactRx*test.recParam.interpFactTx(1):1: ... % create
window to use for correlation over 530 samples

(1131*test.recParam.interpFactRx*test.recParam.interpFactTx(1));        %
grabs samples to cross correlate with received samples
            test.recParam.windowShift = length(test.recParam.window);
% shifts window by length of window for proper application
            timeSigRx = IQrx(:,1).^2 + IQrx(:,2).^2;
% received time signal
            timeSigTx = IQtx(:,1).^2 + IQtx(:,2).^2;
% transmitted time signal

            timeSigTxInterp =
interp(timeSigTx,test.recParam.interpFactTx(1));          % first-stage
transmit interpolation, matches 250e6 sample rate
            timeSigTxInterp2 =
interp(timeSigTxInterp,test.recParam.interpFactTx(2));   % second-stage
transmit interpolation, applies additional interpolation factors
            timeSigRxInterp = interp(timeSigRx,test.recParam.interpFactRx);
% interpolation on received samples to match second stage interpolation
            timeSigTxWindow = timeSigTxInterp2(test.recParam.window,:);
% match cross-correlation window sample rate with received samples

            [r,lags] = xcorr(timeSigRxInterp,timeSigTxWindow);
% apply cross correlation
            [val,shiftIdx] =
findpeaks(r,'MinPeakHeight',test.corrThresh*max(r));       % find correlation
peaks
            shiftCollect(interpIdx) = lags(shiftIdx(1));
% collect sample shift from cross correlation
            deltaN =  -1*(refVec(interpIdx)-shiftCollect(interpIdx));
% sign correction and sample delay calculation
            deltatVec = deltaN ./ ...
                (test.recParam.interpFactRx*test.recParam.receiveRate);
% calculate time delay based on sample rate and current interpolation factor
            deltaCumulative(contFlg,interpIdx) = mean(deltatVec,2);
% average time delay across each mseq, save to deltaCumulative matrix
            if interpIdx == 2
                r_n(contFlg,corrIdx) = max(r(shiftIdx));
                corrIdx = corrIdx + 1;
            end
        end
        [pwr_db(:,n),pwr_db_e(n,contFlg)] =
chpow_v2(timeSigRx,refVec,deltaCumulative(contFlg,:)); % calculate received
power based on IQ samples and time-delay
    end
    pwrDel(contFlg,:) =  (pRef + 20) - mean(pwr_db_e(:,contFlg));  %
calculate increase in loss based on difference from cal, add difference of
power of transmit and cal
```

```
    %% Plot collected results
    figure(1)
    yyaxis left
    plot(distance,pwrDel,'-o')
    ylabel('Power loss in relation to reference (db)')
    yyaxis right
    plot(distance,deltaCumulative(:,2),'-x') % 4x interpolation
    ylabel('Channel delay (s)')
    ylim([0,30e-9])
    grid on
    grid minor
    xlabel('Distance from target (m)')
    title('Current results')

    %% Continue reading measurements check
    beep
    delete(testBar);
    % TIME-DELAY
    if contFlg > 3
        fprintf("\nDISPLAYING LAST 3 MEASUREMENTS")
        printIdx = contFlg - [0,1,2];
        fprintf("\nTIME-DELAY (nS): %.3f %.3f
%.3f",deltaCumulative(printIdx,2).*1e9);
        fprintf("\nCALCULATED CHANNEL LOSS (dB): %.3f %.3f
%.3f\n",pwrDel(printIdx,:));
    else
        fprintf("\nDISPLAYING LAST MEASUREMENT")
        fprintf("\nTIME-DELAY (nS): %.3f",deltaCumulative(contFlg,2).*1e9);
        fprintf("\nCALCULATED CHANNEL LOSS (dB): %.3f\n",pwrDel(contFlg,:));
    end
    contFlg = contFlg + 1;
    resp = input('Would you like to take another measurement? [Y/N] ','s');

    if strcmp(resp,'N') || strcmp(resp,'n')
            contFlg = 0;
    end
end
%% Write power, time delay and correlation coefficient to file
name = input('Save recordings as: ','s');
filename = "Results\" + name + "_PathDelayandLoss.xls";
T = table(deltaCumulative,distance,polarization,antenna,pwrDel,r_n);
writetable(T,filename)
```

VSG60A Initialization Script

```
classdef VSG60A < handle
    %VSG60A Configuration structure of VSG60A for path length measurements
    %   Prepares config struct for path-length measurements

    properties
        center = 5.55e9;%   center frequency in Hz
        power = -20;    %   transmit power of vsg
        respStr = 0;    %   response of last command issued
        tcp = 0;
    end

    methods
        function obj = VSG60A(address,port,centerFrequency,txPower)
            % Initialize connection with VSG60A device
            %   Open tcp port with VSG, create tcpclient obj for
            %   communication, test connection
            obj.tcp = tcpclient(address,port);
            writeline(obj.tcp,'*IDN?');
            readline(obj.tcp);
            obj.center = centerFrequency;
            obj.power = txPower;
        end

%         function obj = chatter(obj,inStr)
%             % General communcation
%             %   Simplifies communication to VSG to one function
%             writeline(obj.tcp,inStr);               % send command to
device
%             pause(.1);
%             if obj.tcp.NumBytesAvailable > 0        % if data to receive
%                 obj.respStr = readline(obj.tcp);
%             else
%                 obj.respStr = -1;
%             end
%
%         end

        function init(obj)
            % init(obj) initialize VSG paramteters
            %   disable outputs until ready to send waveform, set center
            %   frequency and transmit power, select ARB mode
            writeline(obj.tcp,':ROSC:SOUR EXT'); % initialize external clock
reference
            writeline(obj.tcp,':OUTP?');
            obj.respStr = readline(obj.tcp);
            if strcmp(obj.respStr,'1')
                writeline(obj.tcp,':OUTP 0');
            end
            writeline(obj.tcp,':OUTP:MOD?');
            obj.respStr = readline(obj.tcp);
            if strcmp(obj.respStr,'1')
                writeline(obj.tcp,':OUTP:MOD 0');
            end
            writeline(obj.tcp,":FREQ " + num2str(obj.center));     % set VSG
center frequency
```

```
            writeline(obj.tcp,":POW " + num2str(obj.power));        % set VSG
transmit
            writeline(obj.tcp,":RAD:ARB 1");                        % enable
ARB mode
            writeline(obj.tcp,":RAD:ARB:TRIG:TYPE SING");           % only send
one waveform per trigger
            writeline(obj.tcp,":RAD:ARB:IQ:SCAL:AVER 0");           % disable
averaging of samples
        end

        %         function outputArg = method1(obj,inputArg)
        %             %METHOD1 Summary of this method goes here
        %             %   Detailed explanation goes here
        %             outputArg = obj.Property1 + inputArg;
    end
end
```

SM200B Initialization Script

```
classdef SM200B < handle
    %SM200B Configuration class of SM200B for path length measurements
    %   Prepares configuration as well as sets up functions for later
    %   operation.

    properties
        center = 5.55e9;
        power = -20;
        respStr = 0;
        tcp = 0;
        ifBand = 0;
    end

    methods
        function obj = SM200B(address,port,centerFrequency,refLevel)
            % Initialize connection with SM200B device
            %   open tcp port with SM, create tcpclient obj for
            %   communication, test connection
            obj.tcp = tcpclient(address,port);
            writeline(obj.tcp,'*IDN?');
            readline(obj.tcp);
            obj.center = centerFrequency;
            obj.power = refLevel;
            obj.ifBand = 0;
        end

        %         function obj = chatter(obj,inStr)
        %             % General communcation
        %             %   Simplifies communication to VSG to one function
        %             writeline(obj.tcp,inStr);               % send command
to device
        %             pause(.5);
        %             while obj.tcp.NumBytesAvailable > 0        % if data to
receive
        %                 obj.respStr = readline(obj.tcp);
        %                 pause(.1);
        %             end
        %         end
        function checkStat(obj) % check current status of SM200B
            writeline(obj.tcp,'ROSC:SOURCE?');
            pause(.1);
            status.clock = readline(obj.tcp);
            writeline(obj.tcp,':INST?');
            pause(.1);
            status.mode = readline(obj.tcp);
            writeline(obj.tcp,'ZS:CAP:RLEV?');
            pause(.1);
            status.refLev = readline(obj.tcp);
            writeline(obj.tcp,'ZS:CAP:CENT?');
            pause(.1);
            status.Fc = readline(obj.tcp);
            writeline(obj.tcp,'TRIG:ZS:SOUR?');
            pause(.1);
            status.trig = readline(obj.tcp);
```

```
            writeline(obj.tcp,'ZS:CAP:SWEEP:TIME?');
            pause(.1);
            status.sweep = readline(obj.tcp);
            writeline(obj.tcp,'ZS:CAP:SRATE?');
            pause(.1);
            status.caprate = readline(obj.tcp);
            disp(status);
        end

        function init(obj) % init settings for zero-span capture
            writeline(obj.tcp,'ROSC:SOUR OUT'); % enable external 10 MHz
reference out
            writeline(obj.tcp,'INST:SEL ZS'); % select zero-span mode
            writeline(obj.tcp,"ZS:CAP:RLEV " + num2str(obj.power));   % set
reference level
            writeline(obj.tcp,"ZS:CAP:CENT 5.55GHz"); % select center
frequency, hard-set to 5.55 GHz
            writeline(obj.tcp,'ZS:CAP:IFBW?');    % check IFBW
            obj.ifBand = readline(obj.tcp);
            writeline(obj.tcp,'TRIG:ZS:SOUR EXT'); % enable external trigger
in
            writeline(obj.tcp,'TRIG:ZS:SLOP POS'); % set external trigger to
positive
            writeline(obj.tcp,'ZS:CAP:SWEEP:TIME .00025'); % set sweep time
to 1 ms
            writeline(obj.tcp,'ZS:CAP:SRAT 250MHZ'); % set zero-span capture
rate to 250 MHz
%             writeline(obj.tcp,'INIT IMM')
            obj.checkStat();
        end



    end
end
```

Waveform Generation Function

```
function [IQ,timeSig,freqSig,h] = wfGen3(genParam)
%% wfGen3.m
% Generates an output waveform based on input parameter structure genParam
%
% INPUT (structure fields):
%   type:     selects which preprogrammed waveform to generate
%                   0 for pN sequence
%                   1 for constant 1 across all subcarriers
%                   2 for impulse
%                   3 for tone
%
%   bitLength: bit sequence length to use in generating waveform
%   fileW:     file write option
%   plotFlg:   plot option
%   zeroPad:   amount to pad signal
%   subNum:    ammount of subcarrier numbers (currently unused)
%
%
% Jamison Ehlers
% Masters of Science, Electrical Engineering
% Montana Technological University, Fall 2021

%% Create Waveform
if genParam.type ~= 3
    bitSeq = seqGen2(genParam);
    %% Concatinate signal
    if genParam.concat > 0
        for n = 1:genParam.concat
            bitSeq = cat(1,bitSeq,bitSeq);
        end
    end
    sBits = IQgen2(bitSeq);
    if or(genParam.type == 0,genParam.type == 1)
        h =
rcosdesign(genParam.filt.b,genParam.filt.span,genParam.filt.sps,genParam.filt
.shape);
        %% Zero padding
        if genParam.zPad > 0
            zeroVec = zeros(genParam.zPad,1);
            sBits = cat(1,zeroVec,sBits);
        end

        timeSig = filter(h,1,sBits);
        freqSig = fftshift(fft(timeSig));
        filterDel = h;
    else
        timeSig = sBits;
        freqSig = fftshift(fft(sBits));
    end
else
    %%Time specifications:
    Fs = 8000;                   % samples per second
    dt = 1/Fs;                   % seconds per sample
    StopTime = 1;             % seconds
```

```
    t = (0:dt:StopTime-dt)';     % seconds
    %%Sine wave:
    Fc = 133;                     % hertz
    timeSig = cos(2*pi*Fc*t) - j*sin(2*pi*Fc*t);
    freqSig = fft(timeSig);
    I = real(timeSig);
    Q = imag(timeSig);
    IQ = [I,Q];
end
%% File Writing
if genParam.file
    switch genParam.type % detect filename from parameters
        case 0
            filename = "IQ data/IQtx/pN_" +
string(datetime('now','TimeZone','local','Format','MM-dd-y HH-mm-ss')) +
".csv";
        case 1
            filename = "IQ data/IQtx/const_" +
string(datetime('now','TimeZone','local','Format','MM-dd-y HH-mm-ss')) +
".csv";
        case 2
            filename = "IQ data/IQtx/imp_" +
string(datetime('now','TimeZone','local','Format','MM-dd-y HH-mm-ss')) +
".csv";
        case 3
            filename = "IQ data/IQtx/tone_" +
string(datetime('now','TimeZone','local','Format','MM-dd-y HH-mm-ss')) +
".csv";
    end
    I = real(timeSig);
    Q = imag(timeSig);
    fopen(filename);
    writematrix([I,Q],filename);
    IQ = [I,Q];
end
if ~exist('filterDel','var')
    filterDel = 0;
end
if~exist('IQ','var')
    IQ = [real(timeSig),imag(timeSig)];
end
end
```

Sequence Generation Function

```
function [seqOut] = seqGen2(genParam)
%% seqGen2.m
%   Produce bit sequence for waveform transmit based on input parameters
%
%   INPUTS:
%       genParam:       parameter structure, containing parameter fields
%           bitLength:  number of bits to use for sequence
%           type:     type of waveform to generate, see wfGen3 for
%                       options
%   OUTPUT:
%       seqOut:         output bit sequence to use for modulation
%
%   Jamison Ehlers
%   Masters of Science, Electrical Engineering
%   Montana Technological University, Fall 2021
N = 2^genParam.bitLength - 1;
if  genParam.type == 0                % Generate pN sequence
    switch N                            % Select taps based on input length
        case 31
            taps = [5,3];
        case 255
            taps = [8,6,5,4];
        case 511
            taps = [9,8,6,5];
        otherwise
            taps = [8,6,5,4];
    end
    x = ones(N,1);                      % Initialize register states
    seqOut = zeros(N,1);                % Initalize output
    for k = 1:N
        seqOut(k) = x(end);
        xfb = mod(sum(x(taps)),2);      % XOR sum feedback taps
        x = circshift(x,1);             % Shift Registers
        x(1) = xfb;                     % Feedback XOR sum into the first
state
    end
elseif genParam.type == 1             % Generate constant 1 across
subcarriers
    seqOut = ones(N,1);
elseif genParam.type == 2             % Generate impulse function
    seqOut(2^genParam.bitLength) = 1;   % Place impulse in middle of bit
sequence
    seqOut = circshift(seqOut,-16);
elseif genParam.type == 3             % Generate tone (probably won't need)
    % NULL
else
    disp('Unrecognized type, please try again and input recognized type');
    return
end
seqOut = x;
```

IQ Sample Translation Function

```
function [IQ] = IQgen2(bitsIn)
%% IQgen2.m
% Creates signal symbols to be used for VSG60A (Vector Signal Generator
%
% INPUTS:
%   bitsIn: bit sequence to be sent, generated by seqGen
%   sps:    samples per symbol
%
% OUTPUTS:
%   I:  vector of real value samples
%   Q:  vector of imaginary value samples
%   IQ: vector of IQ values for .csv file creation
%
%   Jamison Ehlers
%   Masters of Science, Electrical Engineering
%   Montana Technological University, Fall 2021

%% BPSK modulation to use with workstation
for i = 1:length(bitsIn)
    if bitsIn(i) == 0
        dataBlock(i) = -1;
    else
        dataBlock(i) = 1;
    end
end
% Apply rectangular pulse shaping filter to modulated data, with sps
% samples per symbol, collecting symbol data
Q = imag(dataBlock);
I = real(dataBlock);

% IQ matrix for .csv file creation
IQ = [I + 1i.*Q]';
```

System Calibration Function

```
function [refVec,test,pRef,rcal,lagscal] = sysCal(vsgIn,smIn,IQtx,test)
%% sysCal.m Calibrates system for later measurements
%   Using reference cables, caluclates a "zero path-delay" measurement, to
%   correct for cables and other unwanted delays
%   INPUT:
%       vsgIn:  VSG60A control struct
%       smIn:   SM200B control struct
%           both should be post initialization
%       IQtx:   signal to be transmitted
%       calP:   calibration parameters struct
%       testP:  experiment parameters
%   OUTPUT:
%       refVec: sample delay reference vector
%       test:   updated experiment parameters
%       pRef:   received power reference
%   Jamison Ehlers
%   Montana Technological University
%   Masters of Science, Electrical Engineering
%   Spring 2022

shiftCollect = zeros(1,4);
IQrx = SCPIMeasure(vsgIn,smIn,IQtx);    % make a sample measurement
timeSigRx = IQrx(:,1).^2 + IQrx(:,2).^2;
timeSigTx = IQtx(:,1).^2 + IQtx(:,2).^2;
for interpIdx = 1:1:4
    test.recParam.interpFactRx = 2^interpIdx;
    test.recParam.interpFactTx =
[250e6/test.recParam.transmitRate,test.recParam.interpFactRx];
    test.recParam.window =
601*test.recParam.interpFactRx*test.recParam.interpFactTx(1):1: ...
        (1131*test.recParam.interpFactRx*test.recParam.interpFactTx(1));
    test.recParam.windowShift = length(test.recParam.window);
    timeSigTxInterp = interp(timeSigTx,test.recParam.interpFactTx(1));
    timeSigTxInterp2 = interp(timeSigTxInterp,test.recParam.interpFactTx(2));
    timeSigRxInterp = interp(timeSigRx,test.recParam.interpFactRx);
    timeSigTxWindow = timeSigTxInterp2(test.recParam.window,:);
    [r,lags] = xcorr(timeSigRxInterp,timeSigTxWindow); %% Cross correlate
    [val,shiftIdx] = findpeaks(r,'MinPeakHeight',test.corrThresh*max(r));
    test.recParam.shift = lags(shiftIdx);
    shiftCollect(interpIdx) = test.recParam.shift(1);
    test = test;
    refVec = shiftCollect;
    if interpIdx == 2
        rcal = r;
        lagscal = lags;
    end
end

[~,pRef] = chpow_v2(timeSigRx,shiftCollect,0);
end
```

Channel Power Estimation Function

```
function [pwr_db,pwr_db_e] = chpow_v2(sigIn,timeref,tDel)
%% chpow_v2 Calculates channel power from received IQ samples
```

```
%   Calculates channel power using received I and Q samples from spectrum
%   analyzer used in time delay estimate, and uses window generated by
%   reference delay and measured delay
%   INPUT:
%       sigIn:      power of signal, sigIn = I.^2 + Q.^2
%       timeref:    reference sample delay of system, 1x4,
%       tDel:       calculated sample diference from time ref 1x4
%   OUTPUT:
%       pwr_db_e:   mean receieved power in dBm
%       pwr_db:     received samples in dBm
%   Jamison Ehlers
%   Montana Technological University
%   Masters of Science
%   Electrical Engineering
%   Summer 2022


fsVec = [500e6,1e9,2e9,4e9];                % interpolated sample rates
t_low = mean(timeref./fsVec) + mean(tDel); % beginning of time window
t_high = t_low + 83.76e-6 -(2*10.22e-6);  % end of time window, based on
generated sequence in use at time of writing
t = linspace(0,250e-6,250e6*250e-6);       % time vector for finding samples,
end time based on capture length of SA at time of writing
t_span = find(and(t < t_high, t > t_low)); % find samples wanted

Plin = sigIn;          % power samples, linear
pRx_e = mean(Plin(t_span));                % average power, linear
pwr_db_e = 10*log10(pRx_e);                % average power, dBm

pwr_db = 10.*log10(Plin);                  % power samples, dBm
% figure;plot(t,pwr_db);hold on;plot(t(t_span),pwr_db(t_span));
% fprintf("\nAverage Power (dbm): %.3f", pwr_db_e)
end
```